Novel production pathways for the ^{64,67}Cu theranostic pair: Cross section measurements for the ^{nat}Zn$(n,x)^{64,67}$Cu reactions

by

Nora Irene Jensen Pettersen

THESIS

for the degree of

Master of Science

Faculty of Mathematics and Natural Sciences
University of Oslo

November 23, 2020

Abstract

The main focus of this thesis is to investigate a novel pathway for producing the two medical isotopes ^{64}Cu and ^{67}Cu through the $^{\text{nat}}\text{Zn}(n,x)^{64,67}\text{Cu}$ reactions. Since ^{64,67}Cu are of the same element, they have similar chemical properties which makes them interesting as a theranostic pair. They can be labelled to the same chemical or biological substances and used in both diagnostic and therapeutic applications. ^{64}Cu has a half-life of around 12 hours which makes the production of this isotope preferable to do on-site, without any transport time. The experiment producing the data for this master project was performed at the Lawrence Berkeley National Laboratory's 88-Inch Cyclotron. The aim was to produce neutrons through a deuteron breakup process (using deuteron beams of 16 MeV and 33 MeV) that were then used to activate natural zinc and other monitor foils. The monitor reactions $^{89}\text{Y}(n,2n)^{88}\text{Y}$, $^{27}\text{Al}(n,x)^{24}\text{Na}$ and $^{\text{nat}}\text{Zr}(n,x)^{89}\text{Zr}$ have well-characterized cross sections and are used to compare to our results on the cross sections measurements. The activation of each foil (as a function of time since end of beam) was measured through gamma-ray spectroscopy with a high-purity germanium detector. Fitting the activity to find activity at end of beam and using the monitor cross sections to find the average neutron flux, the spectrum average cross sections for every product made in the targets was found. This experiment showed that the production of ^{64,67}Cu thorough the $^{\text{nat}}\text{Zn}(n,x)^{64,67}\text{Cu}$ reactions is a viable pathway for producing these isotopes. Both 16 MeV and 33 MeV deuteron beam produces more ^{64}Cu than ^{67}Cu, but 33 MeV deuterons will increase the relative ^{67}Cu production. This work resulted in 33 measurements of cross sections using neutrons to irradiate all natural zinc, zirconium, indium, yttrium and aluminum foils, where many of them are first time measurements. The results are compared to previous experiments from the EXFOR-database and simulations using ALICE-2017, CoH-3.5.3, EMPIRE-3.2.3, TALYS-1.9 and TENDL-2019.

Acknowledgements

First of all, I want to thank my supervisors Andrew Voyles and Sunniva Siem. Andrew, thank you for introducing me to this exciting and interesting field of nuclear medicine, answering all of my questions and for being patient with me during this writing process. I really appreciate your all of your feedback on my work. Sunniva, thank you for all of your help with this thesis, for taking me in to the nuclear group and shipping me off to Berkeley by myself. Being able to do this experiment in Berkeley has been something I'm not taking for granted and is a memory that I will bring with me for the rest of my life. I really want to thank the isotope production group in Berkeley, and in particular Lee Bernstein, for being so welcoming and including. A big thank you to Jon, for giving be his unpublished data which made my results even better. I want to thank all the people who have made this time at Blindern amazing, I would not be here if it wasn't for you. I want to thank my family, for your support and encouraging words. Last but not least, Terje. Thank you for being here for me during this time.

Nora Irene Jensen Pettersen

November 23th, 2020

Contents

Chapter 1

Introduction

Count only the good days.

— Irene Jensen, A-Hus 2017

The usage of medical radionuclides can be traced back to as long as late 1890s when Henry Becquerel discovered radioactivity when he was studying a sulfate of uranium, and two years later when Marie Curie together with her husband, Pierre Curie, found activity in the ore where they had extracted uranium from [1]. Since then, many studies on animals and humans have been done which led to development of radionuclides used in therapy and imaging with radiotracers.

According to the National Cancer institute [2] there were 1.735.350 people diagnosed with cancer in 2018 in the United States alone, and approximately one third died. The amount of deaths caused by cancer worldwide in 2018 is approximately 9.6 million people [3]. Without modern medicine like chemotherapy and internal and external radiation, the number of deaths would be much higher. Since radioactivity was discovered in the 1890s, many new applications have been developed in the medical field, such as the use of x-rays by Roentgen in 1895. The tracer approach was developed in 1913 by George de Hevesy [4] when he was investigating the absorption of radioactive lead in plants. In 1927, Blumgart and Weiss [5] used an aqueous solution of radon to study the pulmonary circulation[1] in a man.

Today, nuclear medicine is used for both diagnostics and treatment of a patient.

[1]Pulmonary circulation is the portion of the circulatory system that carries deoxygenated blood from the right side of the heart to the lungs, where the blood oxygenates and returns to the left side of the heart.

PET and SPECT are two imaging techniques that are commonly used in diagnostics. ^{18}F is currently the most used radionuclide in PET scans. Attached to a sugar molecule (FDG), it will find cancerous cells in the body because of the high metabolic activity in cancer cells. In SPECT scans, ^{99m}Tc is often used to diagnose coronary artery disease and stroke. These two illnesses are the number one killer worldwide and ^{99m}Tc is therefore the most widely used radioisotope. Nearly 80% of all imaging procedures use ^{99m}Tc. Therapeutic applications use a radioactive compound and placing it or injecting it into a patient to treat a disease.

In this master thesis, the production of medical isotopes is discussed with the main interest on the production of ^{64,67}Cu. ^{64}Cu and ^{67}Cu are two interesting isotopes that can be used for diagnostic (^{64}Cu) and theranostic (^{67}Cu) applications. They are of the same element, and therefor, because of their same chemistry they can be paired together and used for theranostic applications. ^{64}Cu is fairly easy to make using a ^{64}Ni target and irradiating it with protons, but ^{67}Cu on the other hand, is not. Therefore, a novel pathway of producing both of these isotopes is discussed in this thesis. The production of these two medical isotopes through the $^{\text{nat}}\text{Zn}(n,x)^{64,67}$Cu reactions using deuteron breakup is something that has never been done before. This new way of making ^{64,67}Cu is therefore really exciting. In this experiment, we used 16 MeV and 33 MeV deuterons through a deuteron breakup process, which produces a neutron flux with an energy of approximate 6 MeV and 16 MeV. Five targets (zinc, zirconium, indium, yttrium and aluminum) were irradiated with the neutron flux, producing reaction products such as ^{111}In, ^{87}Y, ^{64}Cu and ^{67}Cu, to mention a few. Measuring the activity at end of beam through gamma-ray spectroscopy allows for the calculation of relative cross sections. The precise neutron flux needed for obtaining "absolute" cross sections which is determined using the monitor reactions with known cross sections. This experiment will give one spectrum-average cross section result at each energy for both ^{64}Cu and ^{67}Cu as well as the relative production yields of ^{64,67}Cu.

The experimental results are compared with monitor reactions (with known cross sections) and modern reaction codes such as ALICE, TENDL, TALYS, CoH and EMPIRE [6–10]. The main motivation of this thesis is then: can we produce two theranostic medical isotopes in a large enough quantity that they can be used in diagnostic and therapeutic applications? And if so, is the production route, using a cyclotron and deuteron breakup a preferable way of doing this?

In this thesis, the characteristics of a medical isotope, why those are important aspects in the production of medical isotopes, and the decision on which isotope that is going to be used is described in chapter 2. A discussion on why ^{64,67}Cu are

interesting theranostic isotopes is presented in chapter 3, followed by a description of details in the experiment, including target stack design and deuteron breakup in chapter 4. How we analysed the data from the experiment is shown in chapter 5, followed by the results and discussion in chapter 6. Finally, the summary and outlook in chapter 7.

Chapter 2

Principles of making medical isotopes

All human things are subject to
decay, and when fate summons,
Monarchs must obey.

Mac Flecknoe
— John Dryden

2.1 Characteristics of medical radionuclides

Radionuclides for both therapeutic and diagnostic use have three principal factors that affect the ability for them to perform as a suitable and effective medical isotope [11], their biological, physical, and chemical properties. The biological and chemical properties affect the stability in a living organism, biological half-life, toxicity, tissue targeting and retention of radioactivity in the tumor [12]. The physical characteristics include physical half-life, energy of the radiation, purity of the radionuclide, type of emission and daughter product(s) [12]. In addition, the method of production is important as it decides how easily available the medical isotope can be.

There are different ways to treat cancerous cells; surgery, chemotherapy, brachytherapy, external beam therapy and targeted radionuclide therapy are some common

techniques. The aim of surgery is to remove as much of the cancerous cells as possible while chemotherapy uses a drug that kills and prevents the cancerous cells to divide and grow [13]. Brachytherapy generally uses beta-, and electron capture or auger sources for therapy but also isotopes that emit gamma rays and x-rays [14]. The source is placed in the targeted location to produce a high dose delivery without damaging healthy tissue [14]. External beam therapy also uses x-rays and protons to kill cancer cells. This method delivers a low-intensity beam or several beams to a patient with a tumor. The beam can deposit the dose to the area of the tumor without much damage to the healthy surrounding tissue [15]. Targeted radionuclide therapy differs from external beam therapy in the way that it uses an antibody or other targeting molecule together with a radioactive isotope to find and irradiate a biologic area of interest. This will allow the irradiation to be at a cellular level rather than a bigger volume [16].

In this chapter, basic theory on general nuclear reactions, high purity germanium detectors, production of medical isotopes and a description of PET-scans is presented. Much of the basic nuclear theory here is adapted from Krane [17].

2.1.1 Half-life

The physical half-life, $t_{1/2}$, of a radioactive substance is the time it takes for a given amount to be reduced by half as a consequence of its decay and is described by the formula:

$$N(t) = N_0 e^{-\lambda t} \tag{2.1}$$

where N_0 is the amount of initial substance, $N(t)$ is how much there is left after time, t, and λ is the decay constant. Using Equation 2.1, the half-life of the decaying quantity is given as:

$$t_{1/2} = \frac{\ln(2)}{\lambda} \tag{2.2}$$

When a radioactive pharmaceutical gets injected into a human body, the biological half-life is important. It is the time it takes for a living body to eliminate half of a substance through its biological processes. Therefore, this has to be considered carefully when a radiopharmaceutical is intended to be used in a patient's body. The half-life should be long enough to do a procedure, but short enough to avoid unnecessary damage to healthy tissue. In diagnostic applications, the half-life should generally be only a few hours. The radioisotope begins to decay immediately after it is produced, so it is important that the physical half-life is long enough such that it can be labelled and given to the patient. If a patient is taking a

PET-scan, the duration will vary depending on the radionuclide. For example, a procedure using ^{18}F usually takes 30-60 minutes to execute. Therefore, the radiopharmaceutical should have a lifetime longer than it takes from production of the radioactive substance to the end of the procedure.

For a therapeutic isotope, the half-life should approximately be a few days. It should be long enough to deliver the right amount of dose to the area of interest. But the most important factor is the effective half-life, the combination of both physical and biological half-life within a patients organ [12]. The physical half-life is well known, but the biological half-life is dependent on several things, including what kind of tracer is used, metabolism, uptake and how the pharmaceutical leaves the body [12]. The choice of tracer and isotope depends on the uptake mechanism, type of tumor and method of administration [12]. If the patient has a low uptake, the physical half-life should be longer such that it will minimize the dose before it has reached the tumor, but not too long such that it contributes excess and unwanted dose on its way out of the body.

Travel time is also a factor when choosing an isotope. If there are cyclotrons in the hospital they can produce isotopes on-site, such as ^{18}F with half-life of 109 minutes [18], that is used in PET scans. In those cases, the half-life can be shorter than if it has to be transported to another part of the county.

2.1.2 Stopping power

When a charged particle penetrates an absorbing medium it will gradually slow down due to energy loss, a process characterized by a quantity called stopping power. There are three known methods of stopping power [19], electronic, S_{col}, nuclear, S_{nuc} and radiative, S_{rad} that contributes to the total stopping power. S_{col} is a result of the charged particle's interaction with orbital electrons in the medium, S_{nuc} is when the charged particle interact with the nuclei in the medium and S_{rad} is due to radiative loss. The total stopping power is given by:

$$S_{tot} = S_{col} + S_{nuc} + S_{rad}$$

.

Electrons can lose energy by Bremsstrahlung(S_{rad}) and by ionization(S_{col}) [20]. Even though the majority of the energy loss for electrons is through collisions, the emission of bremsstrahlung photons is also important. Bremsstrahlung happens when an electron is traveling close to an atomic nucleus and decelerate due to the Coulomb field of the nucleus and atomic electrons. When this happens, energy

releases as photons. The bremsstrahlung yield scales with both the electron's initial kinetic energy, as well as the atomic number of the stopping medium.

When it comes to photons, the beam intensity $I(x)$ will decrease with

$$I(x) = I_0 e^{-\mu x} \tag{2.3}$$

where μ is the attenuation coefficient and depends on the energy, $h\nu$, of the photon and the atomic number Z of the medium [19]. I_0 is the initial intensity of the beam at the surface of the incident medium where the distance $x = 0$.

Photons will also interact with a medium through three mechanisms: the photo-electric effect, Compton scattering and pair production, which are briefly discussed in subsection 2.2.3.

Linear energy transfer (LET)

For therapy, the biological effect depends on how the isotopes decay, and how they distribute the energy of their decay radiation to the surrounding medium. A large LET will concentrate the deposited energy to a small area near the particle's tracks, as a result there will be more damage to the DNA and other cellular structures. LET is closely related to the linear energy loss $\frac{dE}{dx}$ except that LET does not include radiative energy losses.

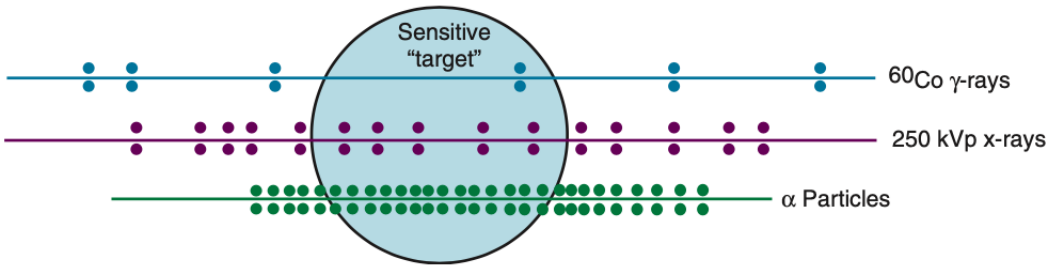

Figure 2.1: An illustration [21] of how γ-rays, x-rays and α particles ionize through a target area. α has a high-LET and γ has a low-LET. The dots along each particle track represent charge carriers created by the particle's ionization of the "target" medium.

As shown in Figure 2.1, high-LET radiation (such as alpha particles, auger electrons, neutrons, and heavy ions) will do more damage in a smaller area and the therapeutic effect is significantly higher than for low-LET radiation (such as photons and beta particles). Low-LET, as shown in Figure 2.1, distributes little

ionization throughout the medium, which results in little to no damage on the cells along the way. In diagnostic procedures, we want to use isotopes that decay with low-LET radiation emissions, and therapeutic procedures seek isotopes with high-LET decay radiation.

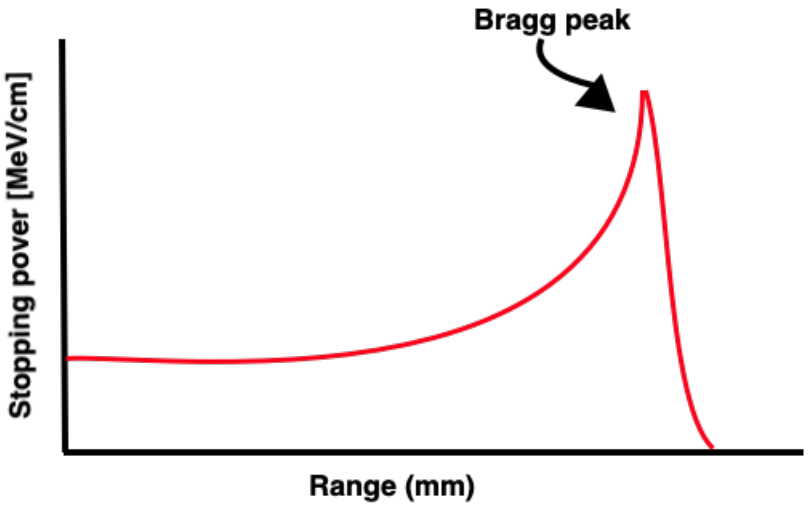

Figure 2.2: Illustration of the bragg curve for charged particles.

Since the ionization of a material increases when the energy decreases for charged particles [19], the energy deposition will be more significant at the end of its tracks. Figure 2.2 shows how the stopping power increases with increasing depth in a medium. The peak at the end is called the "Bragg peak", and is correlated with high-LET, as the charged particle will deposit the majority of its energy in a small volume near the end of its range. By tuning the energy of the beam, the irradiation can be selected so that the brag peak hits the tumor.

2.2 Decay modes

When a patient undergoes diagnostic or therapeutic procedures with radioisotopes, the isotopes that are used must be selected based on decay properties and on the disease being studied. In general, for diagnostic procedures, decay modes that have intense emission branches for low-energy positrons or photons are preferred. In therapy, isotopes which emit alpha particles, auger electrons, or low-energy beta particles are generally preferred. Alpha decay will not be discussed here, as no alpha-emitting radionuclides were produced in this work.

2.2.1 β-decay

β decay occurs for nuclei that have an imbalance between their proton number and neutron number through three different mechanisms: beta-minus (β^-) decay, beta-plus (β^+) decay, and electron capture. In β^- decay, the mechanism is written as:

$$n \rightarrow p + e^- + \bar{\nu_e} \tag{2.4}$$

and the mechanism for β^+ decay is written as:

$$p \rightarrow n + e^+ + \nu_e \tag{2.5}$$

where n is a neutron, p is a proton, e^- is an electron, $\bar{\nu_e}$ is an antineutrino e^+ is a positron and ν_e is a neutrino.

As the electron deposits all of its energy by ionizing matter on its path, β^- decay may be used for therapeutic applications, while β^+ decay is also used in diagnostic applications. If we want to take a picture of the biological activity in a patient, the e^+ is used as a source of two 511 keV photons for imaging in PET scans, which will be discussed in section 2.5.

Compared to α particles, β particles travel much further and create less ionization to the surrounding medium on their path, leading to a more broad-range dose delivery with less total dose per volume. This is important when selecting an isotope based on the size and shape of the tumor, as the biological effect of these two routes differ greatly. There are however, differences in the range of the multiple isotopes that undergo β decay, based on the maximum energy for a given β emission branch. Low-energy β-particle emitters have a relatively short

range of approximately 0.1–10 mm, in tissue where one cell is the size of 0.10 mm (for ∼100-300 keV β particles), making them potentially suitable for treatment of small tumor metastases [20]. Higher-energy ($\geq$ 1 MeV) β-emitters have a much longer range in tissue, penetrating 10's to 100's of mm, and can be used to treat diseases including rheumatoid arthritis, which is an autoimmune disorder that often affects joints.

The energy of β particles are not discrete, but a continuous spectrum. Figure 2.3 is an example of the beta-particle energy spectrum. E_β^{max} is the total energy available for both the electron(positron) and the anti-neutrino(neutrino). The energy of the emitted β particle follows this well-known distribution built upon the Fermi function, based on the energy and emission angle of the (anti)neutrino. The energy will vary from almost zero to the maximum energy, E_β^{max}, and the average energy is approximately one third of the maximum energy.

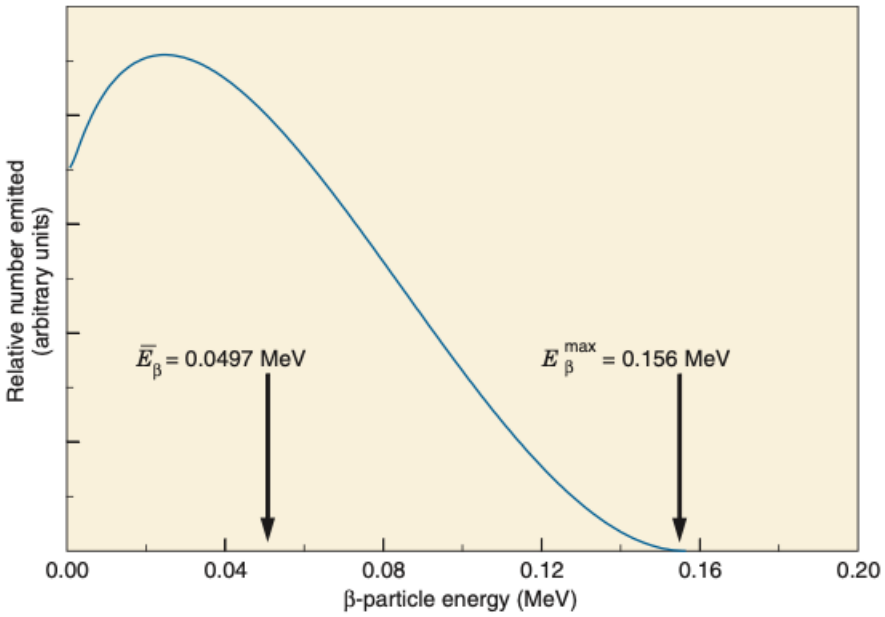

Figure 2.3: An graph of a typical β energy spectrum, in this case, for the decay of ^{14}C [22].

Since the amount of absorbed dose in tissue is proportional to LET and β particles penetrate further into a medium than α particles, β particles have lower LET than α particles. Exposure to β generally results therefore in less dose pr volume.

^{90}Y is a popular long-range isotope used in β therapy, it has a multiple decay

branches and the highest-intensity branch has a mean range of 4.3 mm in water [23] with an average energy of 933 keV [23]. A widely used short-range beta emitter is ^{131}I where the highest-intensity branch for ^{131}I has a mean range of 0.4 mm in water with an average energy of 182 keV [23].

2.2.2 Auger electron created through electron capture and internal convention

An Auger electron is a low-energy electron that can be a product of electron capture or internal convention. When an electron from the inner shell is removed, leaving a vacancy, an electron from a higher orbit fills the vacancy and releases energy. Often, the energy is emitted as a photon, but the energy can be transferred to an electron which gets ejected form the atom. The ejected electrons are called an Auger electrons. The distance the auger electrons travels is less than a cell in biological tissue [24]. These electrons have high-LET and will therefore do a lot of damage to the DNA and other important structures in the cellular nucleus that are important for the cell to live. This makes the auger electrons highly effective for treating cancerous cells (see Figure 2.4b).

In an electron capture (EC) decay, an electron can be captured by the nucleus, converting a proton turn into a neutron. When this happens, there will be a vacancy created in the inner shell (closest to the nucleus) which one of the electrons in the outer shell will try to fill. As β^- decay, EC will lead to a change in element:

$$ {}^{\mathrm{A}}_{\mathrm{Z}}\mathrm{X} \xrightarrow{\mathrm{EC}} {}^{\mathrm{A}}_{\mathrm{Z}-1}\mathrm{Y} \tag{2.6} $$

where X is the parent nucleus with mass number A and Z protons, and Y is the daughter nucleus.

In this process, characteristic x-rays and several auger electrons will be emitted from the daughter nucleus [22].

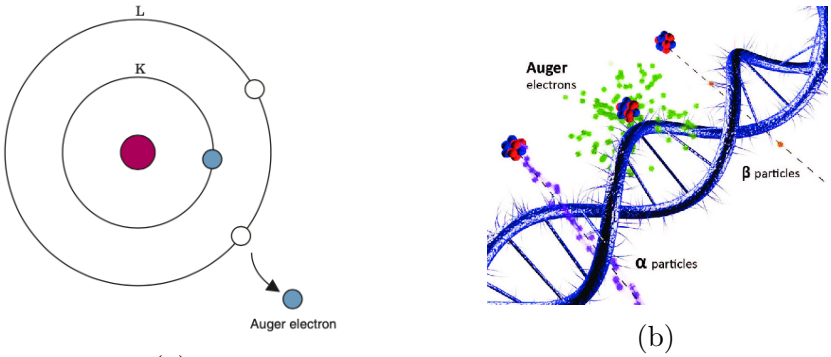

(a) (b)

Figure 2.4: Panel (a) is an illustration of emission of an auger electron [25]. Panel (b) shows the range of auger electron compared to α and β particles [26].

Internal conversion (IC) is a type of de-excitation, where a nucleus returns from an excited state to the ground state. When this happens excess energy is released and transferred to an orbital electron. This internal conversion electron gets ejected, leaving a vacancy in the inner shell. An electron from a higher energy level will move to the vacancy and releases an x-ray or an Auger electron [25].

2.2.3 γ-decay and X-rays

Gamma rays and x-rays are both forms of electromagnetic radiation. The difference between them is that X-rays have their origin from electronic transitions outside of the nucleus and γ's are created from nuclear transitions. Both X-rays and γ's penetrate a medium and depending on their energy, they can create different effects in the body by ionization. γ-rays and x-rays can interact with a medium in three different processes: photoelectric effect, Compton effect or pair production.

The photoelectric effect happens when an orbital electron absorbs the incoming photon. The energy absorbed will eject an orbiting electron, E_e, from the atom. This electron is called a photoelectron [20]. The electron cannot be emitted if the incoming photon energy is lower than the binding energy of the electron (E_b). The energy of the electron emitted is $E_e = E_\gamma - E_b$ where E_γ is the incident photon's energy. The probability of photoelectric effect happening is measured as the cross section τ:

$$\tau \propto \frac{Z^n}{E_\gamma^3} \tag{2.7}$$

where Z is the atomic number and n is equal to 4 or 5 [27, p. 140].

In Compton scattering, an external photon is scattered by an atomic electron. When an incident photon interacts with an atomic or free electron, it will deflect from its original path with an angle from $\theta = 0°$ to $\theta = 180°$, and the electron recoils with an angle ϕ. The energy is shared between the emitted electron and the photon, where the incident photon will transfer some of its energy to the electron. The atomic cross section for Compton scattering is $\sigma_c = NZ\sigma_e$ where $\sigma_e \propto \frac{1}{E_\gamma}$ is the electronic cross section, assuming a free electron [20].

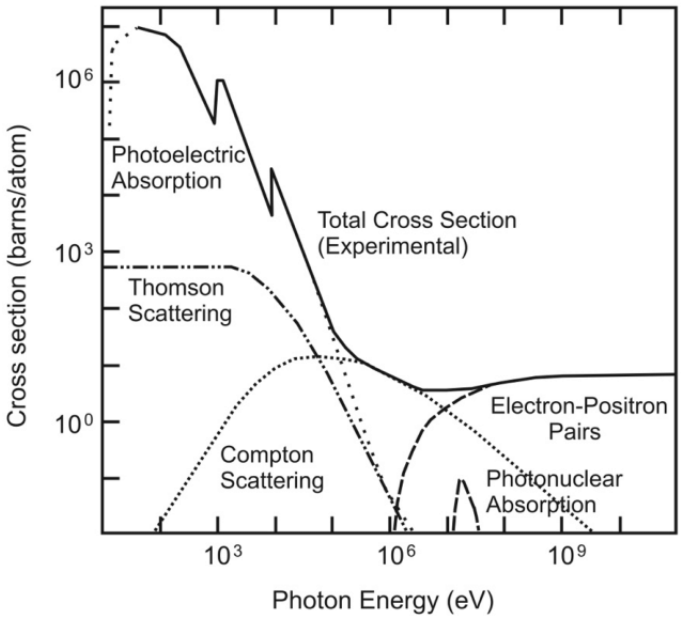

Figure 2.5: Cross section for photoelectric effect, Compton scattering and pair production for copper as a function of photon energy [28].

The last interaction mechanism is pair production. The incoming photon annihilates in the nucleus' Coulomb field, causing an electron-positron pair in the vicinity of a nucleus, which are emitted collinearity (180 degrees apart). This can only happen if the energy of the photon is greater than the total rest mass of an positron-electron pair, 1.022 MeV, where the energy is split between the electron and positron. The cross section for pair production (π) is proportional to Z^2 .

Figure 2.5 shows how the three main interactions of a photon depend on energy. For lower energies the photoelectric effect is dominant, pair production is more probable to happen at higher energies, and Compton scattering dominates in between.

Since X-rays and γ's can penetrate long distances without ionizing the medium, has a low-LET and can emerge from the body, they are ideal to use for diagnostic procedures using different imaging techniques.

γ decay

Following radioactive decay, the nucleus is often left in an excited state which will de-excite by emitting a photon [20]. This process is described in Equation 2.8 where A is the atomic number, Z is the number of protons in the nucleus X and X^* is an excited nucleus:

$$^{\mathrm{A}}_{\mathrm{Z}}\mathrm{X}^* \rightarrow {}^{\mathrm{A}}_{\mathrm{Z}}\mathrm{X} + \gamma \tag{2.8}$$

The excitation energy is transferred to a γ photon plus the recoil energy.

Most nuclear exited states are very short-lived ($t_{1/2} < 1$ ps). However, if the A notation includes an "m", the nucleus is in a long-lived ($t_{1/2} > 1$ µs) isomer state, (e.g., ^{99m}Tc) [20]. The de-excitation of this isomer state will then be described as an isomeric transition (IT).

γ-ray emission and internal conversion (IC) are two competing ways for the nucleus to de-excite. In internal conversion, the nucleus will electromagnetically interact with a shell electron which leads to emitting of the orbiting electron [29].

A nucleus can be excited either by the creation of a compound nucleus, with a direct reaction or if a nucleus decays with one of the decay modes described in section 2.2 into an exited state in another nucleus. The nucleus will decay into its ground state by emitting one or more γ-rays. The latter is illustrated in Figure 2.6, for the decay level scheme of ^{67}Zn.

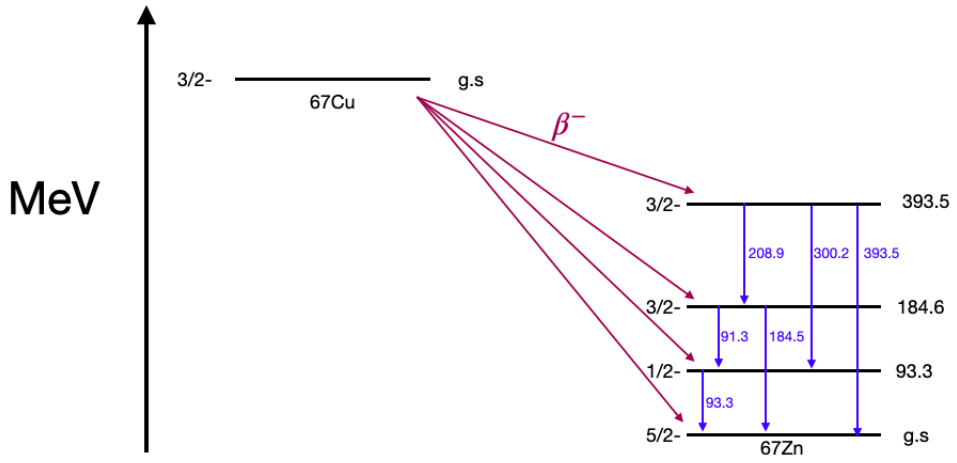

Figure 2.6: An illustration of how ^{67}Cu is β-decaying down to ^{67}Zn. [30]

As Figure 2.6 shows, the γ's that are emitted in ^{67}Zn when the nucleus de-excites will have different energies. The emitted γ's can then be detected with a detector. In this experiment, a high-purity germanium detector was used.

2.3 High-purity germanium (HPGe) detectors

Most semiconductor detectors are based on the n-p junction, which is a boundary between two different types of doped semiconductor, seen in Figure 2.7. A crystal is doped on one side with a material that has excess electrons in the outer shell and therefore is called the negative side, or n-type. The other side is doped with a material that has electron vacancies in its outer shell, leaving a "hole". This side is called p-type, since it is more positive. When these two types are interfaced together, the electrons from the n-type will be attracted to the holes in the p-type, leaving a depletion zone free of charge carriers, around the junction interface, with a net negative charge on the p-side and a positive charge on the n-side. This creates an intrinsic electric field which makes it hard for any electrons produced in the depletion zone to travel to the p-side unless there is a voltage applied to the crystal.

The effect of having an electric field, either intrinsic or externally-applied, is that

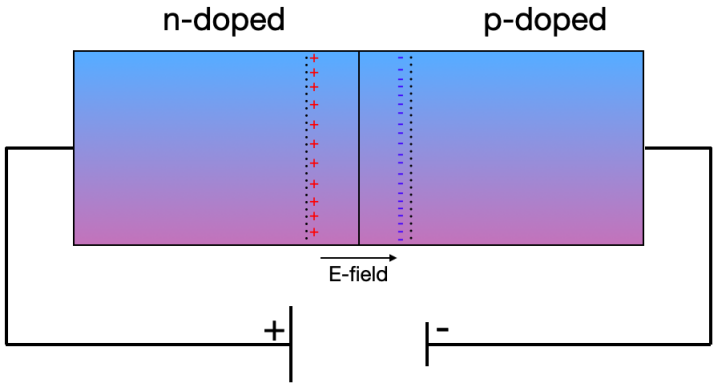

Figure 2.7: Example schematic for the n-p junction of a semiconductor.

a pair of charge carriers generated inside the depletion region between the two crystals, the holes and the electrons will be pushed away and collected at their respective electrodes. This can be used in different ways: if you don't apply any voltage from the outside, the depletion zone will be quite small. The depletion zone can be used for detection, if ionizing radiation creates a free electron inside the depletion zone, it will be swept out by the electric field and may be collected as a voltage pulse. However, hole-pairs that are created outside of the depletion zone can't be collected because they will quickly recombine. If the goal is to efficiently detect radiation, a big depletion zone is preferable [31, p. 226]. This is done by reverse biasing.

Reverse biasing is done by applying an external voltage where a positive terminal is connected to the n-type side and a negative terminal to the p-type side. This will cause the holes and electrons to drift so the depletion zone become larger. The larger the voltage, the bigger the depletion zone, unless too much voltage is applied. In this extreme, the material can break down and damage the detector. The maximum depletion you can obtain is inversely related to the density of the doping. If a lot of doping is added in the material to make it work, it means that one can only produce a narrow depletion zone. This is why high-purity semiconductors are often used in radiation detection; since a pure material doesn't need as much doping, less doping means that the detector can have a thicker depletion zone. This translates to having more material where you can detect particles and read out the deposit charge as pulses, leading to improved detector efficiency.

2.3.1 How to get a spectrum from gamma-rays

Since γ-rays do not have a charge, they can only interact with the detector through different electromagnetic interactions. In these interactions the γ-ray energy is transferred to electrons or an electron and positron pair in the detector medium, as described in subsection 2.2.3. It is these electrons that are being detected in the reverse-biased detector and in the electronics as an electric charge, can vary in energy from almost zero to the full energy of the gamma [32, p. 30]. The electrical charge that is registered in the detector is proportional to the gamma-ray energy absorbed in the detector [32, p. 61]. The charge is then collected and converted into voltage pulses before it is sorted by pulse height. The electronics count the number of pulses within the pulse heights and assigns them to a channel number, which gives rise to a gamma spectrum [32, p. 61]. The peaks in the spectra are due to the decay of the sample in the detector, as seen in Figure 2.8.

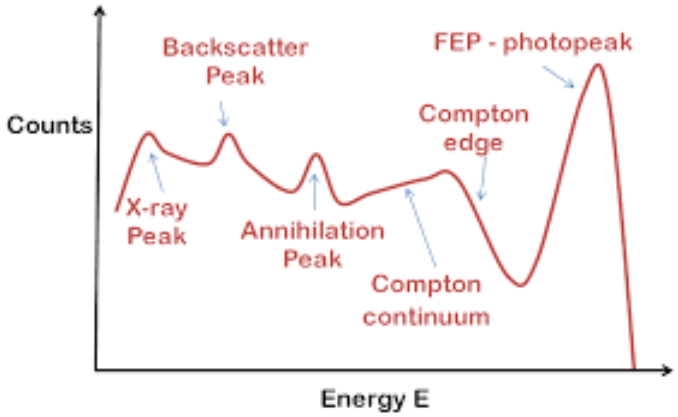

Figure 2.8: A typical detected gamma-ray spectrum for a given incoming E_γ(FEP) where the visualisation of the different gamma interactions are shown [33].

Figure 2.8 shows a typical spectrum from an HPGe detector. At low energies the characteristic X-ray peaks are created when gamma-rays interact with the detector shielding. The Compton continuum happens when a gamma-ray from Compton scattering leaves the detector and transfers only a portion of its energy to an electron in the detector. The energy received by the electron can vary due to the angle of the photon scattered. The Backscatter peak appears when the scattered gamma-ray from a Compton scatter happens outside of the detector

and the backscattered photon enters the detector with an angle $\theta = 180°$. The backscatter peak has the same energy as the backscattered photon [32].

The full-energy peak happens when the a gamma-ray is absorbed with full energy in the detector. This most often happens through the photoelectric effect but in theory it can happen in all cases of interactions.

Annihilation peak occurs due to pair production. If a positron annihilates with an electron outside of the detector, it creates two 511 keV gammas where one of them moves onto the detector, a peak with 511 keV will appear [32]. If, however, the pair production happens inside the detector and creates the two 511 keV gammas, a few different things can happen: If both gammas interact with the detector and does not undergo Compton scattering but photoelectric effect, they contribute to the full-energy peak. If one gamma escapes the detector there will be a single-escape peak with the energy of a full-energy peak - 511 keV. If both of the 511 keV gammas escapes, a double escape peak is created with the energy of full-energy peak - 1022 keV.

2.3.2 Calculation of activity from fitted peaks

The activity follows the radioactive decay law, which describes the behaviour of a large number of nuclei:

$$dN = -\lambda N dt \tag{2.9}$$

where N is the number of atoms in a radioactive sample, dN is the change in N during a change in time, dt, λ is the decay constant. If A is the activity of a source, A decreases exponentially with time and is given as:

$$A = \frac{-dN}{dt} = \lambda N \tag{2.10}$$

Using Equation 2.9, rewriting and taking the integral, gives:

$$\frac{dN}{dt} = -\lambda N \quad \rightarrow \int \frac{dN}{dt} = \int -\lambda N \quad \rightarrow lnN = \lambda t + C \tag{2.11}$$

C is an arbitrary constant of integration. Assume that at $t = 0$ there are no atoms, N_0, present gives $C = lnN_0$. Equation 2.11 can be written as:

$$ln\frac{N}{N_0} = -\lambda t \tag{2.12}$$

or

$$\frac{N}{N_0} = e^{-\lambda t} \tag{2.13}$$

Since the activity in a sample is proportional to the number of atoms present, the activity can be defined as:

$$\frac{A}{A_0} = e^{-\lambda t} \tag{2.14}$$

where A_0 is the activity at time $t = 0$. Thus, the activity can be written as:

$$A(t) = A_0 e^{-\lambda t} \tag{2.15}$$

where $A(t)$ is the activity at a specific time. When a spectrum is counted from a time point after end of beam (Δt_d) with a counting time (Δt_c), the calculation of the number of decays can then be written as:

$$N_D = \int_{\Delta t_d}^{\Delta t_d + \Delta t_c} A_0 e^{-\lambda t} dt = \frac{A_0}{\lambda} e^{-\Delta\lambda t_d}(1 - e^{-\lambda \Delta t_c}) \tag{2.16}$$

inserting $A(t)$ gives:

$$N_D = \frac{A(t)}{\lambda}(1 - e^{-\lambda \Delta t_c}) \tag{2.17}$$

When a spectrum from the detector is created, the only known information is the number of counts, N_c, which is dependent on the efficiency of the detector, ϵ_{eff}, the intensity of the gamma-ray per decay, I_γ, and the number of decays, N_D:

$$N_c = \epsilon_{eff} I_\gamma N_D \tag{2.18}$$

N_c can then be written as:

$$N_c = \epsilon_{eff} I_\gamma \frac{A(t)}{\lambda}(1 - e^{-\Delta\lambda t_c}) \tag{2.19}$$

The activity then becomes:

$$A_0 = \frac{\lambda N_c}{\epsilon_{eff} I_\gamma (e^{-\lambda \Delta t_c})(1 - e^{-\lambda \Delta t_d})} \tag{2.20}$$

or:

$$A(t) = \frac{N_c \lambda}{\epsilon_{eff} I_\gamma (1 - e^{-\lambda \Delta t_c})} \tag{2.21}$$

2.4 Production of medical isotopes

There are many ways in which radionuclides can be produced. Neutron induced reactions, charged particle induced nuclear reactions, fission, selective separation and gamma induced reactions are the most important ones [19]. These ways of producing radionuclides are done either with a cyclotron, a generator or a nuclear reactor. This subsection will only describe a cyclotron since that is what has been used in the experiment in this thesis.

To produce one or more new isotopes, the nucleus and an external particle have to interact with one another. When this occurs, some reactions can happen: neutron induced fission, fusion, nuclear decay and transmutation. Fission is where a heavy nucleus splits into two lighter nuclei. Fusion on the other hand, is the opposite. Two lighter nuclei merge together to create a heavier nucleus. If the product nucleus is left excited, it can de-exite by emitting a γ radiation or it can follow nuclear decay. This is a process where an unstable isotope transforms into a different isotope by decaying through β^-, β^+ or α, emitting ionization radiation as a result. Transmutation is where high energy radiation or neutrons are used to irradiate a specific target with the intention to create a radioactive isotope. For example, in this experiment, natural zinc was bombarded with neutrons to create copper-64 and copper-67 which can be used in diagnostics and therapy.

Nuclear reactions: Compound vs direct reactions

The general equation for a nuclear reaction is:

$$a + A \rightarrow b + B + Q \tag{2.22}$$

where A is the target nucleus, a is the projectile, B is the product nucleus, b is the outgoing particle(s), and Q is the mass difference between the initial and final nuclear configurations, often referred to as the "Q-value". The nuclear reaction is often written as:

$$A(a, b)B \tag{2.23}$$

A nuclear reaction occurs when an interaction between two nuclei or nuclei particles

happens and produces one or more nuclei in the process. If there is no production of a new nuclei, the process is called nuclear scattering. A nuclear reaction can be a direct reaction or a compound reaction. A direct reaction happens where the incoming particle knocks out the incoming particle(s). Equation 2.22 defines this process [19]. But for a compound reaction, the incoming particle is absorbed by the target, transferring energy to the nucleus. This leaves the nucleus with excess energy, this energy gets concentrated in one neutron and escapes the attraction.

2.4.1 Accelerator designs

The medical field was revolutionized by the invention of the cyclotron. Ernest Lawrence build the first cyclotron in Berkeley, CA with the intention of accelerating particles to a high enough energy so they can be used to produce new particles [34]. From a German article written by Winderöe on multiple acceleration on a positive ion, Lawrence and his brother John realized that this can be used in medical applications. John was a medical doctor and was interested in the use of radioisotopes to treat cancer, and in 1935 he came to Berkeley to test ^{32}P for therapy in mice which had a positive outcome. In 1937 John moved to Berkeley and performed his first treatment on a human using radioisotopes. In fact, Ernest and John's mother was diagnosed with cancer in her uterus and given a few months to live. John and Ernest got her to a special clinic that gave her novel radiation therapy and she lived for another 15 years [34].

The cyclotron and the linear accelerator are two designs for accelerators that are commonly used to accelerate particles today. The cyclotron used in this thesis to produce medical isotopes and is described in chapter 4, section 4.3. A cyclotron consists of two D-shaped conducting chambers, called "dees". An alternating electric and a perpendicular fixed magnetic field causes the charged particles to move in an circular orbits. The ions get injected into the center of the cyclotron and start to accelerate by a high frequency electric field that is produced in the gap between the two dees [35], illustrated in Figure 2.9.

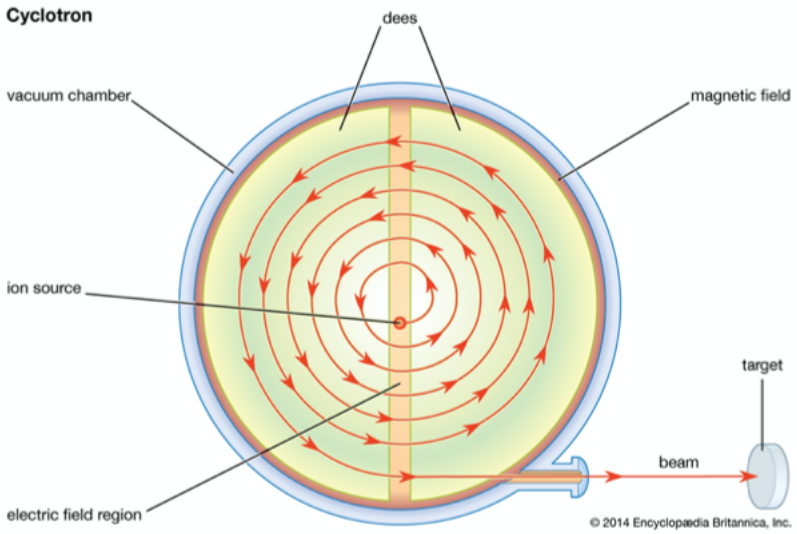

Figure 2.9: Structure of a cyclotron [36].

The rotation frequency is constant as the velocity increases and thus the radius of the movement increases until it exits the cyclotron [35]. The charged particle can then hit a target to produce other isotopes. The centripetal movement is provided by the Lorentz force:

$$\frac{mv^2}{r} = qvB \tag{2.24}$$

where B is the magnetic field, q is the particle charge, m is the particle mass, r is the radius of the circular movement to the particle in the dees and v is the particle velocity. This shows that the particle's energy is dependent on the magnetic field and the diameter of the dees.

Cyclotrons in hospitals

Cyclotrons in hospitals are important for modern medicine. They can be used for proton therapy and radioisotope production for both PET and SPECT isotopes [37]. The different usage of cyclotrons require different energies. For proton therapy a cyclotron that can produce beam with up to 200-250 MeV is needed, while for medical isotope production, an energy of up to 15-30 MeV or higher is required [37].

Linear accelerators (linacs) are used to treat patients with cancer through external beam therapy. Such a linac produces high energy electron beams that are shaped to cover the tumor that is being treating. The principle of operation is to accelerate

particles with an electric field [35].

2.5 PET-scans

In the 1950s, positron emitters and their usage in imaging techniques were described by Frank R. Wrenn, Myron L. Good and Philip Handler [38]. This opened up to the possibility to use radioactive isotopes to identify and diagnose different diseases. Prior to the discovery of ^{99m}Tc in 1964 [39], the most commonly used radionuclide for diagnostic purposes was ^{131}I and was used to study and diagnose thyroid disorder [40]. After Paul Harper and his colleagues used ^{99m}Tc for brain scanning [39], because of its flexibility for labeling, ^{99m}Tc was used to study various organs in the body. The gamma decay properties of ^{99m}Tc were proven to be useful for imaging, and the fact that it could be produced in a long-lived generator made it attractive for usage in hospitals [39]. Another big development was the mathematics to produce a complete image of a body based on angular views around the patient [40]. This technique was important for the evolution of nuclear imaging, and is the basis for imaging procedures used today like SPECT, CT, MRI and PET.

Positron emission tomography (PET) is an imaging technique to monitor the biological processes in the body by using radiotracers [41]. PET uses annihilation photons that are produced when a positron interacts with an electron and thus, the radiotracer that is being used must be a positron emitter. The basic principle of PET imaging is when a positron interacts with an electron near the site of the positron decay in the body, they will annihilate and the energy converts into two photons that will get released in the opposite direction with 180 degrees between them [42]. The energy of the photons are identical (511 keV) and will be detected by detectors that are placed around the patient. The observation of the two photons is done by the principle of annihilation coincidence detection (ACD). It assumes that the annihilation happens at a straight line from where the two γ's is detected, illustrated in figure 2.10b. This makes it possible to find their origin along a line between the detectors [42].

(a)

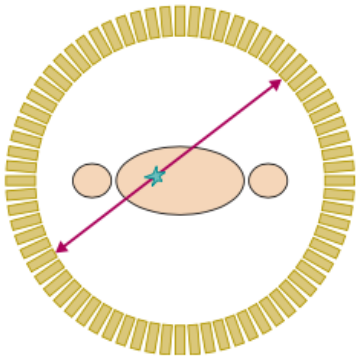

(b)

Figure 2.10: Subfigure (a) shows a clinical PET machine that is used in hospitals and subfigure (b) visualizes the detection of photons [42].

The half-life of the isotopes used in PET-scans can vary. It depends on what kind of biological processes that are of interest but, the half-life is relatively short (from a couple of minutes to a few hours) compared to isotopes used in therapeutic applications. These isotopes have to be produced as-needed and most preferably, on site [43]. Since most diseases do not change the anatomy in the body and are dependent on some kind of activity, the isotopes used in PET scans are attached to a compound that targets different parts in the body, such as protein, sugar and water [43]. A table of some isotopes used in PET scans is listed in Table 2.1

Isotope	Physical half-life	Decay mode (%)	Production
^{11}C	20.36 m	β^+ (100)	Cyclotron
^{13}N	9.965 m	β^+ (100)	Cyclotron
^{15}O	2.03 m	β^+ (100)	Cyclotron
^{18}F	109.77 m	β^+(100)	Cyclotron
^{64}Cu	12.701 h	β^+ (61.50)	Cyclotron
		β^-(38.50)	
^{68}Ga	67.71 m	β^+ (100)	Generator
^{124}I	4.1760 d	β^+ (100)	Cyclotron

Table 2.1: Isotopes used in PET and their half-life [18, 44–50].

Applications of PET

The use of PET scans requires an isotope that will emit a positron, and ^{18}F is currently one of many isotope used in diagnostics. It has a half-life of 109 minutes

[18], and is the most common isotope used in PET. Increased local uptake for ^{18}F-fludeoxyglucose, or FDG, in the tissue indicates that there is a pathological condition that increases the tissue's metabolic rate relative to surrounding tissue [42]. The fact that FDG can be used for a whole-body scan makes ^{18}F a favorite as a medical isotope. As Figure 2.11a shows, FDG-PET is a good imaging technique not only to detect cancer, but also to find metastases and to see how the treatment is working. Combining PET with CT gives a more precise anatomical localization of the radioactive substance that is inside the body.

(a)

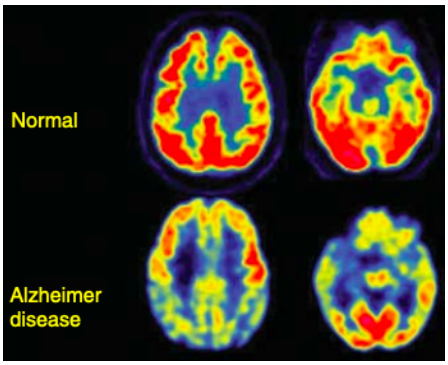

(b)

Figure 2.11: (a) shows an FDG-PET scan of a 47-year-old woman with primary breast cancer, but as the PET scan shows, also metastases in hip bone. Taken from [51]. (b) shows an FDG-PET scan of a brain with and without Alzheimer disease. The normal brain has a much higher uptake of glucose than the brain with Alzheimer disease [52].

^{18}F can also be used in neuroimaging. The brain uses glucose as fuel and for this reason FDG-PET is not well-suited for imaging the brain for cancer. But, Alzheimer's disease usually decreases the brain's metabolic activity, leaving the brain with less oxygen and glucose [53]. As shown in Figure 2.11b, there is less activity in the brain with Alzheimer's disease. FDG can also be used to find other neurodegenerative diseases, dementia, epilepsy, neurodevelopmental disorders and psychiatric disorders [42].

One other radiotracer used for PET-scans is ^{15}O; used along with water as a tracer. It is used for studying blood flow, oxygen flow, blood volume and oxygen volume

[54, 55].

Two interesting radionuclides used for therapy and diagnostics are ^{64,67}Cu. They are a new theranostic pair that are promising to this relativly new field of nuclear medicine [56]. Further details on ^{64,67}Cu are given in chapter 3, as these are the main nuclei of interest in this thesis.

Chapter 3

A deep-dive into Copper

> The pessimist complains about the wind; the optimist expects it to change; the realist adjusts the sails.
>
> — William Arthur Ward

Nuclear medicine is a growing field, where the basis of research is in diagnosis and treatment of patients. It is important to produce patient-friendly isotopes that can be used in theranostic applications that allows to switch between diagnostics and therapeutic applications when a disease is investigated. Copper is one element with six isotopes that is under research for use in a theranostic approach and will be discussed in section 3.2.

3.1 The role of copper in nuclear medicine

There are six copper isotopes that are suited for usage in nuclear medicine: ^{60}Cu, ^{61}Cu, ^{62}Cu, ^{64}Cu, ^{66}Cu and ^{67}Cu. Of these, because of the short half-life, ^{60}Cu and ^{62}Cu are preferable to image fast processes *in vivo*, such as renal and myocardial perfusion [57, 58]. ^{61}Cu, ^{64}Cu and ^{67}Cu have longer half-life and thus, are used to study slower processes *in vivo* that have an accumulation of a specific targeting agent [59]. Because of the short half-life and its high-energy β^- emission, ^{66}Cu can be used for treatment of tumors in a cocktail approach, where ^{66}Cu is combined

with ^{67}Cu or ^{64}Cu for a better therapeutic effect [60].

Isotope	Half-life	Decay (%)	Main Radiation [keV]	Application
^{60}Cu	23.7 m	EC/β^+ (100)	β^+ : 1981.8(49.0%) γ: 1332.5 (88.0%)	Imaging
^{61}Cu	3.33 h	EC/β^+ (100)	β^+ : 1215.5(51.0%) γ: 656.0 (10.8%)	Imaging
^{62}Cu	9.67 m	EC/β^+ (100)	β^+ : 2936.9(97.6%)	Imaging
^{64}Cu	12.07 h	EC/β^+ (61.5)	γ : 1345.77(0.475%) β^+ : 653.03(17.60%)	Imaging
		β^-(38.5)	β^- : 579.7(38.5%) $AugerL$: 0.84(57.7%) $AugerK$: 6.54(22.5%)	Therapy
^{66}Cu	6.12 m	β^- (100)	β^- : 2640.9(90.7%)	Therapy
^{67}Cu	2.57 d	β^- (100)	β^- : 377.1(57%) β^- : 468.4(22.0%) β^- : 561.7(20.0%) $AugerL$: 0.99(19.14%) $AugerK$: 7.53(6.87%)	Therapy
			γ : 91.266(7.00%) γ : 92.3(16.10%) γ : 184.5(48.7%)	Imaging

Table 3.1: Properties of some copper isotopes [30, 47, 61–64]

Targeting molecules

Copper is found naturally in the human body and is important for the function of many enzymes and thus, for our metabolism [65]. It has an important role in several funtions, including cell signaling, oxygen transport, strength of the skin and blood vessels [66]. Copper is absorbed in the gut and binds to a protein called albumin, from there it is transferred to the kidney and liver [67] where the regulation of copper occurs [68]. In the cellular structure, one of many roles of copper is that it works as a cofactor to an enzyme called cytochrome C oxidase, also called coplex IV. It is a part of the electron transport chain, which takes

place in the mitochondria where it plays a vital role in the detoxification of free radicals. It pump H^+ (protons) into the intermembrane and as a result, helps the cell's energy process (ATP) [69]. Copper is also a crucial cofactor for enzymes that regulates the production of neurotransmitters, iron transportation from cells, blood clotting and more [66, 70, 71]. A mice study by Zhou et al. [72] shows that lack of copper in the diet of newborn mice can cause severe heart hypertrophy. Copper has a vital role in many physiological processes and is therefore important to investigate.

Copper is generally bound with a protein or peptide *in vivo* [68]. When copper is injected into a patient, radiocopper with a bifunctional chelator can be labelled with proteins, nanoparticles, antibodies, peptides or small molecules that have high selectivity accumulation to the targeted area [59][73]. In the human body, Cu^+ is usually found in the intercellular medium and Cu^{2+} in the extracellular space, the difference in their oxidation states gives them very different chemical properties [74]. Cu^+ is more unstable in aqueous solutions because its bonds are labile, this means that a ligand exchange can happen and thus, Cu^+ is not often used as a radiopharmaceutical [60]. For a pharmaceutical in PET scans, Cu^{2+} is the preferred chemical form of ^{64}Cu. Designing a chelator that prevents other copper chelator proteins *in vivo* from stealing the Cu^{2+} ion is challenging [73]. The oxidation state of copper plays a role when choosing a chelator, as the binding affinity to the copper and stability are major selection factors for *in vivo* applications [75]. Since copper bonds easily to nitrogen, the copper can bind to other nitrogen molecules in the body and be stripped from the chelator. As shown in Figure 3.1, DOTA and TETA are two chelators that are most commonly used together with ^{64}Cu for PET-scans. Because of better stability, Trientine (TETA) is the preferred chelator for labelling to proteins, antibodies and peptides [76, 77].

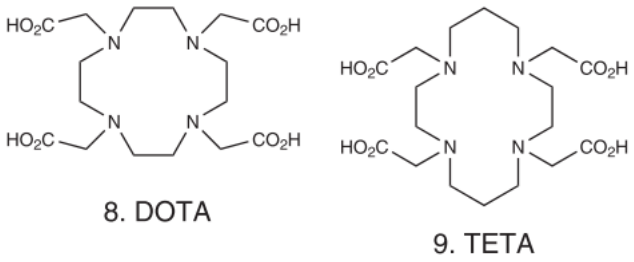

Figure 3.1: Chelators that are commonly used with copper. Picture from [73].

TETA is not only useful for PET-scans. TETA was originally produced as an

alternative to D-penicillamine which is a chelating agent for the treatment of Wilson's disease (caused by an overabundance of copper in the body), and showed effective results [78]. Because if its binding capacity to copper, TETA has also shown promising results for treatment of Alzheimer's disease [79],the prevention of organ damage due to diabetes [80] and tumors [81]. DOTA is not always the most stable *in vivo* but is the most commonly used chelator [73]. Because of the labeling condition needed for DOTA (low temperature for 20 minutes), the stability for up to 48 hours in serum and availability, it is approved from Food and Drug administration for use [73]. DOTA can be fitted with a range of different radionuclides, such as ^{111}In for SPECT [82], ^{90}Y for treatment of neuroendocrine tumors [83] and ^{68}Ga for PET-scans [84].

Copper toxicity

As previously mentioned, copper is naturally found in the body. Copper is consumed through water and food, and plays an important role in many metabolic processes. Too much copper on the other hand, can be toxic to the body and the levels of biological copper are therefore important. If an adult consumes an estimated level of 10–20g of copper, untreated it can be lethal [85]. Copper is mostly stored in the brain, kidney and liver ($\sim$ 5 µg/g) due to the metabolic activity that copper plays a role in [86]. The daily recommended intake for copper is 1.1–1.2 mg/day and an upper limit of 10 mg/day for adults [86]. Copper toxicity in the body can lead to acute symptoms such as: vomiting blood, low blood pressure and abdominal pain [87]. The kidney and liver can be damaged by long term effects where a large amount of copper is stored in the body or consumed.

Since the essence of this Master's thesis are the production and cross sections of ^{64}Cu and ^{67}Cu, the main focus in the rest of this section will be on these two isotopes.

Copper-64

As shown in Table 3.1, ^{64}Cu decays via both β^+ and EC. This means that in principle ^{64}Cu can be used for both diagnostics and therapy. ^{64}Cu is a low-energy positron emitter with only a single β^+ emission branch, seen in Table 3.1. It has a half-life of 12 hours [47] and its range in tissue is on average 0.7 mm [56] for positrons, which makes it a favourable radioisotope for PET scans. ^{64}Cu is in itself a theranostic isotope since it has both diagnostic and therapeutic decay radiation. The fact that ^{64}Cu decays with β^+ in 61.5% of the cases, and that the half-life is a bit short for a therapeutic approach which makes it less favorable for treatment.

^{64}Cu is currently used in clinical trials for imaging applications including blood

flow, hypoxia, prostate cancer, neuroendocrine tumors and colon cancer [88].

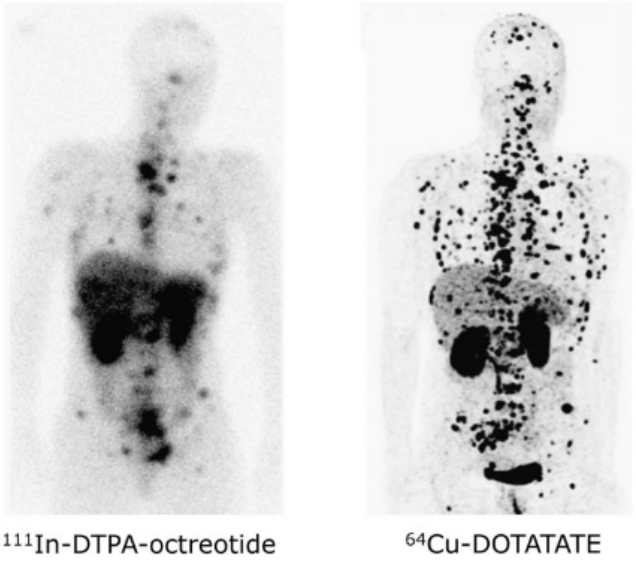

Figure 3.2: A comparison of ^{111}In-DTPA-octreotide in SPECT with ^{64}Cu-DOTATATE in PET in a patient with multiple endocrine neoplasia type I syndrome. The patient has therefore multiple soft-tissue and bone metastases as shown in the multiple dark areas in this figure. The ^{64}Cu PET scan has visibly superior resolution compared to the ^{111}In SPECT scan, and noticeably reduced uptake in the stomach. Image taken from [89].

As Figure 3.2 shows, ^{64}Cu gives a clear image on where the cancer is in the patient using PET. In this first-in-human study done by A. Pfeifer er al. [89], ^{111}In-DTPA-octreotide was compared to ^{64}Cu-DOTATATE. ^{64}Cu-DOTATATE was shown to localize lesions that were not found in previous images and lesions in organs that previously had not been identified as metastatic sites [89]. Compared to the most commonly used radioisotope for PET scans, ^{18}F, ^{64}Cu has a lower branching ratio and therefore, it requires 5.5 times higher activity [56] to give the same quality in the image, which is a drawback.

Copper-67

With its half-life of 2.57 days [30], it is the longest lived radioisotope of copper, thus, it has a preferable decay time for therapeutic applications. It decays via β^- and emits γ-rays (184 keV) in the process, seen in Table 3.1. This makes ^{67}Cu, in principle, suitable for both therapeutic and diagnostic (SPECT) use [56]. But there is no gamma energy emitted by ^{67}Cu close to 140 keV, which is important for

imaging with SPECT and because of its half-life where the dose rate to the tumor is high, ^{67}Cu is mainly studied with regard to therapeutic use. Several studies [90–92] comparing the effect of ^{131}I-labeled Lym-1 antibodies with ^{67}Cu-labeled Lym-1 antibody used to treat non-Hodgkin's lymphoma in patients and mice have shown promising results. Another study done on bladder cancer consisted of 16 patients with ^{67}Cu-labeled Anti-MUC1 Mucin Monoclonal Antibody C595 [93] had the conclusion that ^{67}Cu is promising for usage in bladder cancer.

3.2 Theranostic applications

Nuclear medicine is being advertised as a form of personalized medicine. This indicates that the patient's characteristics such as anatomy, physiology and genetics are evaluated when radioisotopes for diagnostic and therapy are chosen [56]. To make the planning and execution of a treatment easier and more efficient, researchers look at different ways to combine therapy and diagnostics, an approach referred to as "theranostics.". ^{64}Cu and ^{67}Cu are two isotopes that are being evaluated for theranostic use [56]. When radioisotopes used for diagnostic and therapy have the same chemical properties they can be attached to the same type of carrier agent and injected into a patient's body at the same time.

Generally, theranostic pairs use isotopes of the same element, but recent work has explored the use of two different isotopes labelled with the same targeting molecule. ^{64}Cu / ^{67}Cu [94], ^{123}I / ^{131}I [95] and ^{68}Ga-DOTATATE (diagnostic) / ^{177}Lu-DOTATATE (therapy) [95] are three examples of isotope pairs that can be used in theranostic techniques. Since the theranostic applications in nuclear medicine are becoming more valuable, there are a range of isotopes that are being researched. A study from 2019 done on tumors in mice by Cristina Müller et al, [96] shows that the radionuclide ^{44}Sc together with ^{47}Sc are good isotopes to be used as a theranostic pair in the future. Another study [97] done on ^{86}Y and ^{90}Y in 2017 concluded: "we believe that this radionuclide represents a valuable choice for radiotheranostics".

The combination of diagnostics and therapy can be delivered in one package. It can be used for imaging and monitoring the diseased tissue, controlling the ability to tune the therapy and dose, drug efficacy and delivery kinematics [98].

^{64}Cu and ^{67}Cu are two interesting isotopes that can be used for theranostic applications because of their favourable nuclear properties. Copper is naturally found in organs and cells, it is a part of several enzymes [99] where the highest levels

of copper is found in the brain and liver in both newborn and adults [99]. Diseases such as Wilson's disease, where there is a mutation in a specific gene that is responsible for the extraction of copper through the bile, can be investigated through imaging with copper [100].

A study done by Biggin et al, [94] compares the usage of ^{64}Cu/^{67}Cu with ^{68}Ga/^{177}Lu as a theranostic pair. The study concluded that imaging with PET using ^{64}Cu paired with ^{67}Cu provides advantages for a range of different tumor types.

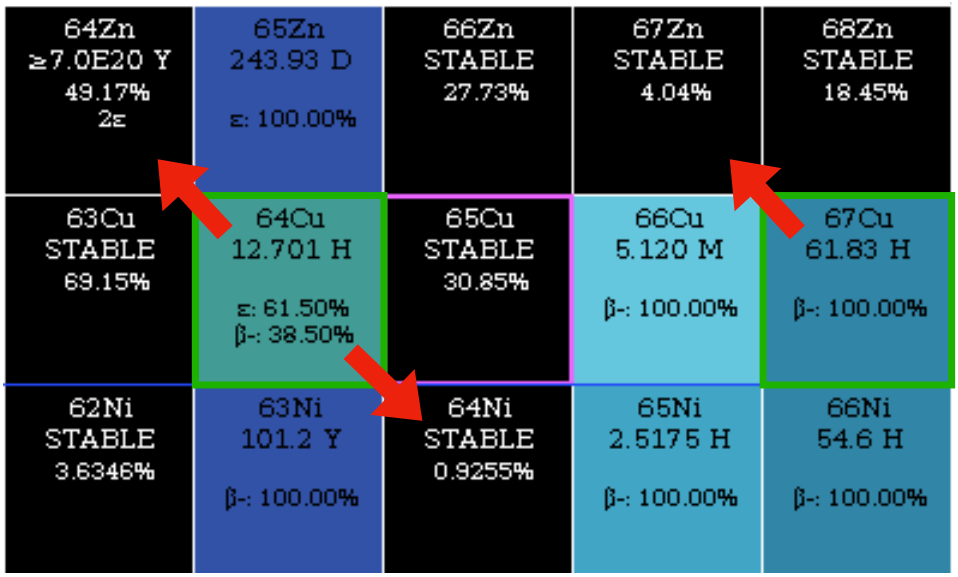

Figure 3.3: The decay of ^{64}Cu and ^{67}Cu. Both decay down to a stable isotope. Figure from [101].

Together, ^{64}Cu and ^{67}Cu are a interesting new pair for theranostic application, shown in Figure 3.3. Both ^{64}Cu and ^{67}Cu decay down to stable isotopes, they have the favourable decay for both diagnostics and therapy and as section 3.3 will discuss, there are different ways to produce them.

3.3 Production of Copper-64 and Copper-67

Even though ^{64}Cu and ^{67}Cu are two interesting radioisotopes, there are some challenges in making them. The most common way to produce ^{64}Cu is through the $^{64}\text{Ni}(p,n)^{64}\text{Cu}$ reaction using a cyclotron [102, 103]. Another way to make ^{64}Cu is in reactors, where fast neutrons are used in the $^{64}\text{Zn}(n,p)^{64}\text{Cu}$ reaction [104]. A reactor is not a preferable way of doing production on ^{64,67}Cu. The fraction of fast neutrons compared to thermal neutrons are low and since the cross sections rise at approximate 2 MeV (discussed in chapter 6), the thermal neutrons are not of any use. However, ^{67}Cu is more difficult to produce and therefore there are not many biological studies done with this isotope. One way to produce ^{67}Cu is with a higher-energy proton accelerator with an energy of over 70 MeV [105] where the $^{68}\text{Zn}(p,2p)^{67}\text{Cu}$ reaction is aimed at. Another production route is the $^{70}\text{Zn}(p,\alpha)^{67}\text{Cu}$ reaction that was produced with a low energy proton beam [106]. The most common way to get ^{67}Cu, is through $^{67}\text{Zn}(n,p)^{67}\text{Cu}$ in a nuclear reactor [56]. The different production routes of ^{64}Cu and ^{67}Cu gives not only cross section measurements, but also production yields (discussed in chapter 5, section 5.4). Some reported yields for ^{64}Cu and ^{67}Cu through different reaction routes are listed in Table 6.1. While many other exotic routes exist (such as the use of heavy ion fusion-evaporation reactions), the focus here is limited to those production routes capable of being used by the existing medical cyclotrons.

Isotope	E_i-E_f (MeV)	Reported yield	Units	Production route	Target thickness
^{64}Cu [102]	15.5	5.0	mCi/µAh	$^{64}\text{Ni}(p,n)^{64}\text{Cu}$	311 µm
^{64}Cu [107]	*	1.983	mCi/µAh	$^{64}\text{Ni}(p,n)^{64}\text{Cu}$	144 µm
^{64}Cu [108]	16	4.89	MBq/µAh	$^{64}\text{Zn}(d,2p)^{64}\text{Cu}$	325 µm
^{64}Cu [108]	16	8.24	MBq/µAh	$^{66}\text{Zn}(d,\alpha)^{64}\text{Cu}$	325 µm
^{64}Cu [109]	70-35	21.0	mCi/µAh	$^{66}\text{Zn}(p,2pn)^{64}\text{Cu}$	20 µm
^{64}Cu [109]	25-10	1.8	mCi/µAh	$^{68}\text{Zn}(p,x)^{64}\text{Cu}$	50 µm
^{64}Cu [109]	37-21	5.0	mCi/µAh	$^{68}\text{Zn}(p,x)^{64}\text{Cu}$	50 µm
^{67}Cu [110]	70-50	0.46	mCi/µAh	$^{68}\text{Zn}(p,2p)^{67}\text{Cu}$	10 µm
^{67}Cu [108]	19.5	0.01	MBq/µAh	$^{67}\text{Zn}(d,2p)^{67}\text{Cu}$	325 µm
^{67}Cu [111]	8-18	2.9	MBq/µAh	$^{70}\text{Zn}(p,\alpha)^{67}\text{Cu}$	◇

Table 3.2: Reported production yields for ^{64}Cu and ^{67}Cu. E_i is the initial energy and E_f is the final energy of the irradiation. (*) "The ^{64}Ni target was bombarded with a 50±3 µA proton current" [107]. (◇) Thin ^{70}Zn layers of 1.6–20 mg/cm^2 was prepared by an electrolytic deposition method [111].

None of the production reactions listed in Table 3.2 produce both ^{64}Cu and ^{67}Cu at the same time. In this experiment, a novel way of creating these isotopes simultaneously is presented. Using ^{nat}Zn as a target, deuteron breakup, creating a neutron flux in the two irradiation's for this thesis, was used to produce both ^{64}Cu and ^{67}Cu. The neutron flux had an average energy of approximately 6 MeV and 12 MeV, corresponding to a deuteron energy of 16 MeV and 33 MeV, respectively. The experiment was done using the 88-Inch Cyclotron at Berkeley, CA. Using two different energies will create ^{64}Cu and ^{67}Cu in different ratios, this means that the tuning the energy of the beam will adjust the production of the isotopes.

Chapter 4

The Experiment

He who is brave is free.

— Seneca

In this thesis we have to studied the $^{\text{nat}}\text{Zn}(n, x)^{64,67}\text{Cu}$ reactions. In section 4.1, the experiment itself is discussed together with the beam tuning and the irradiation of the targets. Section 4.2 describes the HPGe detector that was used for counting, and includes the energy, peak and efficiency calibration. The Lawrence Berkeley National Labratory's 88-Inch Cyclotron was used in this experiment and the deuteron breakup process is introduced in section 4.3. How the targets were stacked together during irradiation is discussed in section 4.4.

4.1 The experimental setup

The experiment was performed in August 2018 at the Lawrence Berkeley National Laboratory where deuterium beams with an energy of 16 and 33 MeV were used. The deuterium beam was focused to irradiate a beryllium target, creating a neutron "beam" through the deuteron breakup process. Five targets (zinc, zirconium, indium, yttrium and aluminum) were then irradiated with the neutrons, as illustrated in Figure 4.1. For the 16 MeV run, the targets were irradiated with an average of 247.7 nA of deuterons for 7 hours and 57 minutes, and 2 hours and 20 seconds with an average of 354.5 nA (measured with an external Faraday cup) of deuterons for the 33 MeV run. The run duration and beam current for the two irra-

diations were separately chosen, based on knowledge of the relative neutron yields at each beam energy. A higher energy beam and a longer irradiation time will open up additional reaction channels and increase the dose from the activated targets in addition to driving activities closer to saturation. The irradiation conditions must be balanced such that enough activity is made to quantify the weakly-fed reaction products, without causing excessive dead time in the HPGe detectors used to count these targets. For the breakup of 33 MeV deuterons, we know from previous work at the 88-Inch Cyclotron (as discussed in subsection 4.3.1) that the total neutron yield (per nA of deuterons) is approximately two to three times higher than for 16 MeV. This increased yield allows for the shorter irradiation time for the 33 MeV deuteron case.

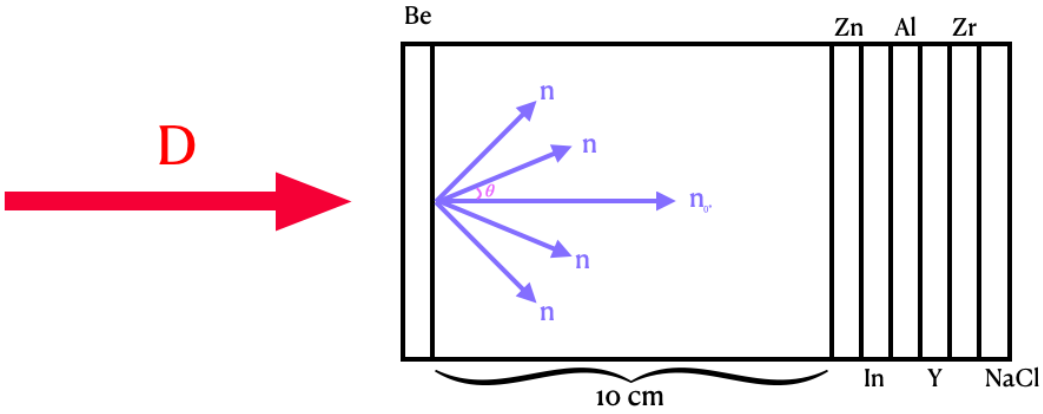

Figure 4.1: Illustration of the kinematics of the deuteron breakup neutron emission and how the activation foils were positioned relative to the breakup target.

The irradiation took place in Cave 0, as seen in Figure 4.2. In this figure, the green line entering this cave is the beam line, which is connected to the cyclotron. The beam arrives at Cave 0 via two bending magnets where any deuterons which are accidentally extracted from the cyclotron at the wrong energy will be lost when the beam is bent to the correct beamline. Cave 0 has the thickest shielding of all experimental caves at the 88-Inch Cyclotron, when a high energy beam enters the cave there will be an intense flux of neutrons and x-rays in the room. Shielding is therefore one of the main reasons why high energy experiments are done in Cave 0.

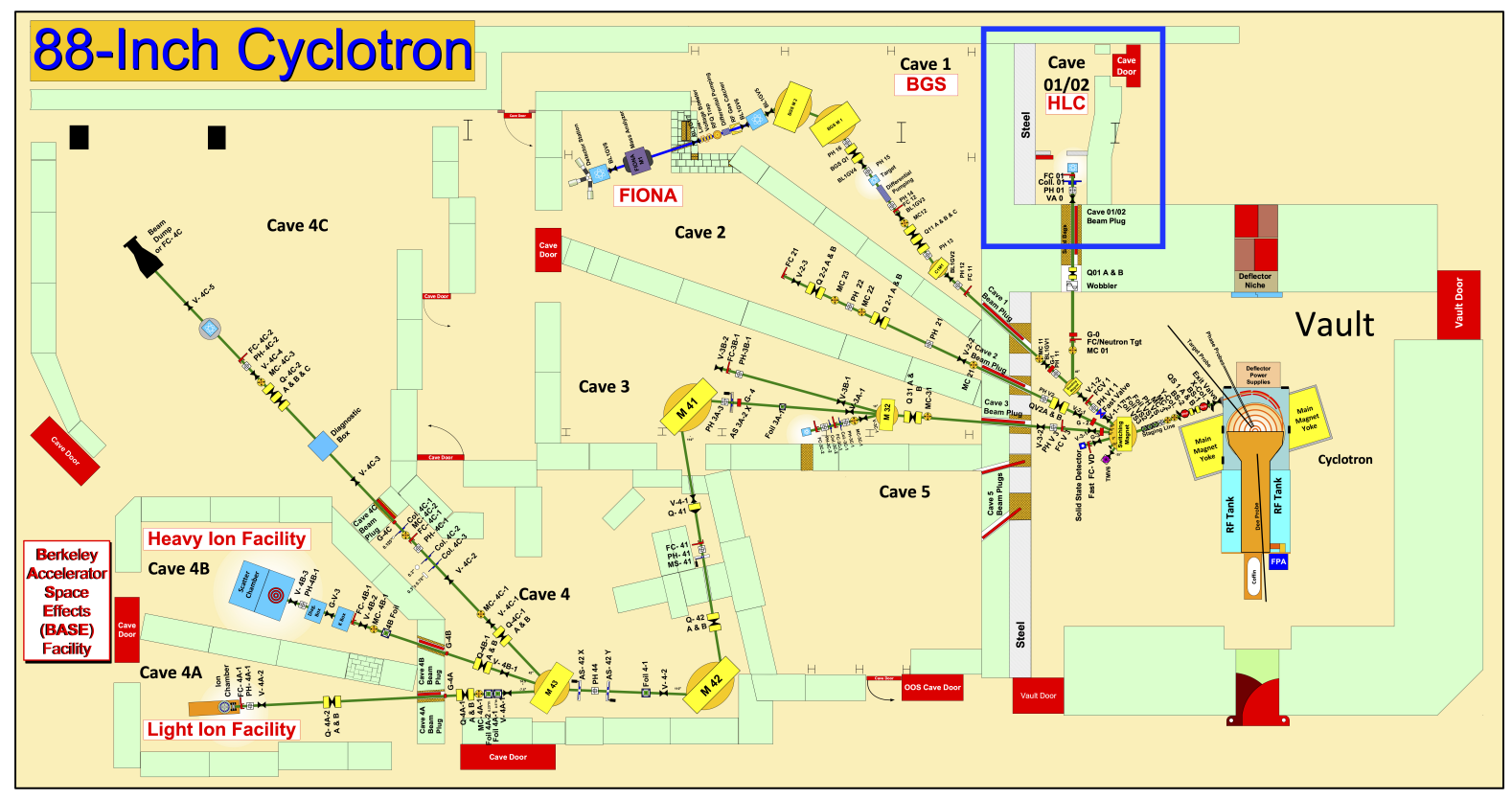

Figure 4.2: Map of the 88-Inch Cyclotron at Lawrence Berkeley National Laboratory. The irradiations which took place in this work were performed in Cave 01/02 (blue square). Figure is from private communication by A. Voyles.

Before the irradiation, the beam had to be tuned such that it was a well-collimated pencil beam (without significant convergence or divergence) before it hits the beryllium target. Since the neutrons from deuteron breakup are emitted from the beryllium target with an angular distribution, the goal is to get a intensely forward-focused neutron beam. The targets were placed 10 cm away from the beryllium target in order to minimize the emission angle of neutrons which hit the targets, as this maximizes the neutron energy. The amount of neutrons that reaches the targets is represented as the solid angle. Solid angle (or geometry factor) is a 2D angle in a 3D space, it is a measure of the amount of particles from a point source that enters a disk surface, as shown in Figure 4.3.

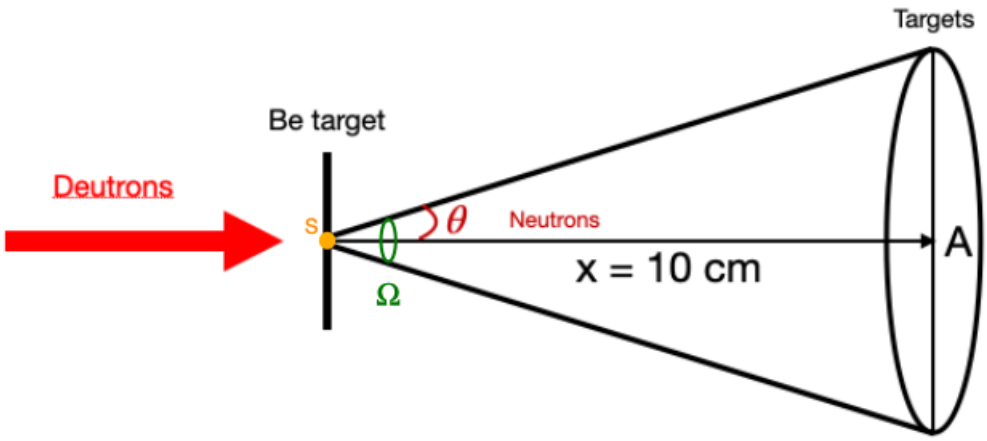

Figure 4.3: An illustration of a circular plane that represents the beam profile with an angle θ, having an area A where the centre lies at a distance, x, and perpendicular to the point source, S. Ω is the solid angle defined by A.

As seen in Figure 4.3, the further back the target stack is placed, more of the forward-focused neutrons will hit the targets, since the targets will only have a small planar angle θ. However, since the neutron flux will decrease with solid angle, Ω, there is a trade-off between getting only the highest-energy neutrons and maximizing flux.

In the calculation of the cross sections in chapter 6, section 5.5, includes the correction for solid angle. That correction accounts for the fact that there is a slightly different neutron flux on each monitor foil because of the spacing between them in the experiment, also the solid angle dependence of the breakup neutron

flux. The foils are therefore getting a slightly different number of neutrons, but the neutron flux per solid angle should be constant within uncertainty. Since our deuteron beamspot illustrated in Figure 4.4 is not a point source, the solid angle is calculated for each of the targets with a Monte Carlo simulation [112].

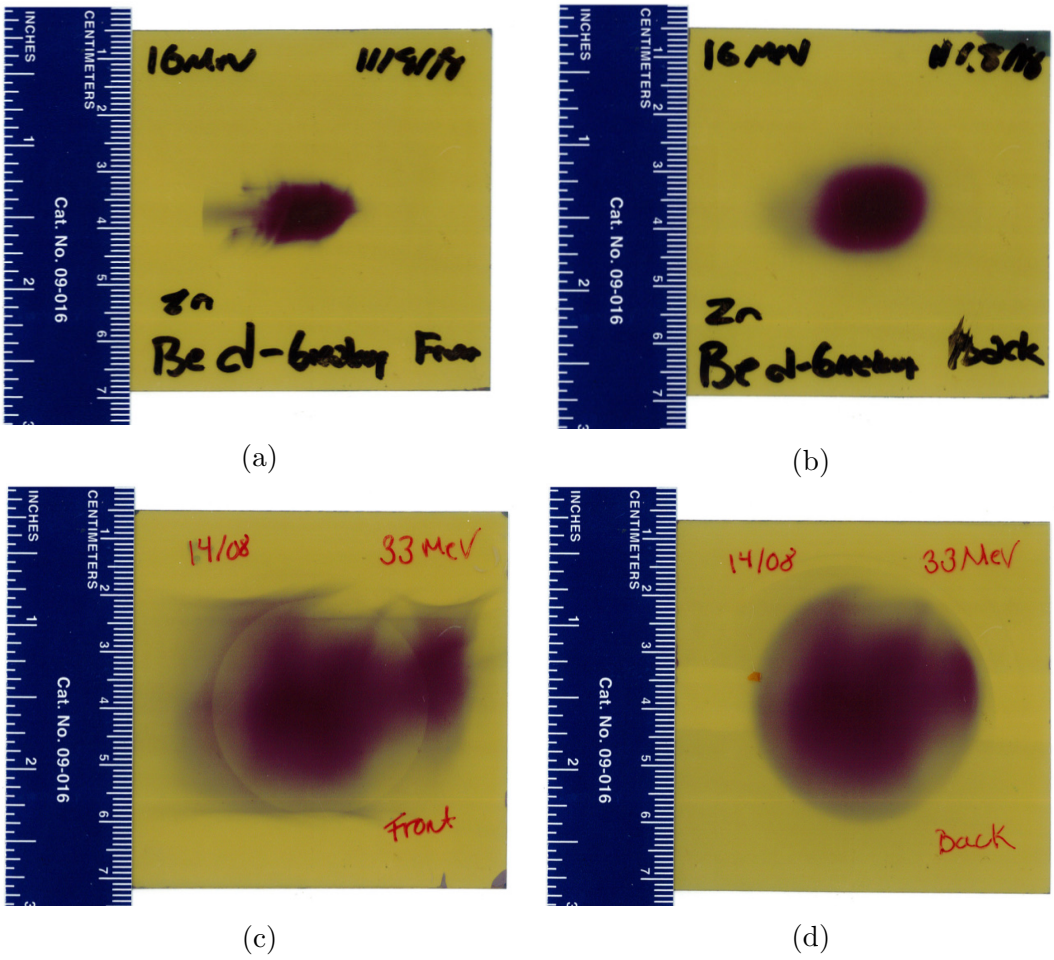

(a) (b)

(c) (d)

Figure 4.4: Pictures of the deuteron beam spots in this work, developed using Gafchromic EBT3 film. (a) shows the beam spot of the front film where the Beryllium target is placed and (b) shows the beam in the back where all of the other targets are placed during the 16 MeV run, and (c) and (d) shows the beam spot for the 33 MeV run.

The Gafchromic EBT3 films in Figure 4.4 are used for visual measurements of ionizing radiation [113] and in this experiment, they were used to image the deuteron beam spot incident on the beryllium target during the beam tuning. The films are usually used for dose mapping and dose verification for external

photon therapy, Gafchromic films do not need any post-irradiation processing compared to other radiographic films like EDR2 [114], which is a standard film for dosimetry. The Gafchrimic EBT3 films have an active layer which consists of an active component, stabilizers, a marker dye and other components; these give the film a near energy-independent response [113]. When the films are irradiated, the active layer will react and the blue coloured polymer will show where the radiation was hitting the film [113]. In previous work, Gafchromic film has been used to directly image the spatial intensity profile of the beam spot [114, 115].

After tuning a centered and uniform beam spot, the targets were mounted in an aluminum target box and then placed into the beamline and sealed down to vacuum, as seen in Figure 4.5. The vacuum is needed to decrease the amount of interactions between the air particles and the incident deuterons inside the target holder.

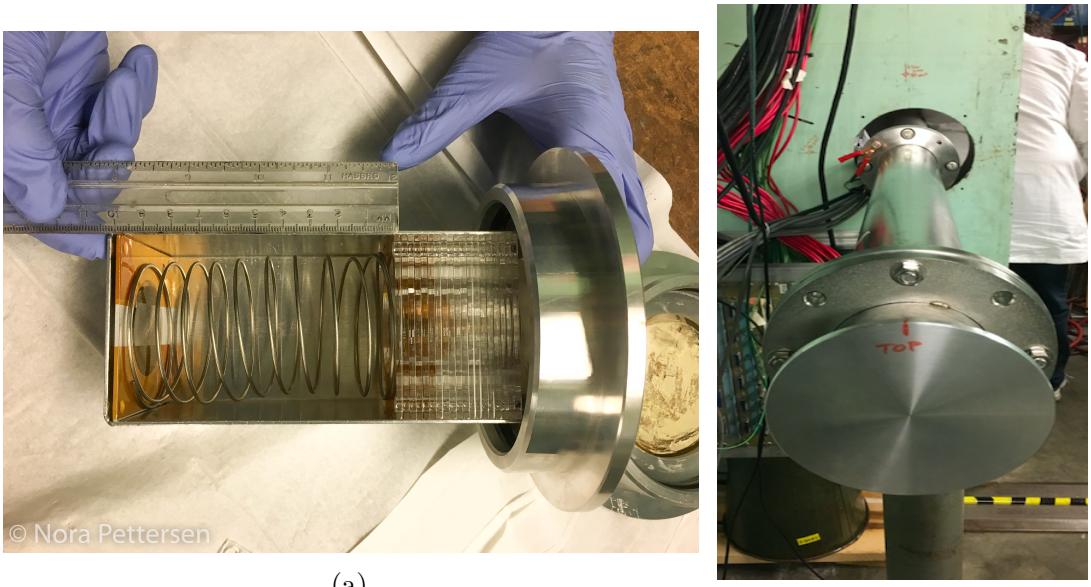

(a) (b)

Figure 4.5: Figure (a) shows how the targets were stacked inside the target holder prior to irradiation. (b) is the position where the target box was placed at end of the beam line inside Cave 0.

During the irradiation, the target stack was connected to a beam current integrator in the control room, which measured the current on the beryllium target and reported an integral current for each run, $I\Delta t$. This is done to check how much total current the targets receive and to make sure that the irradiation is stable over time. If the irradiation is unstable it will affect the calculations on the activity by

modifying the term $\Phi(1 - e^{-\lambda t_{irr}})$ in Equation 5.12 in chapter 5, section 5.3 . A plot of the current integrator readout over the time for the 33 MeV irradiation is shown in Figure 4.6.

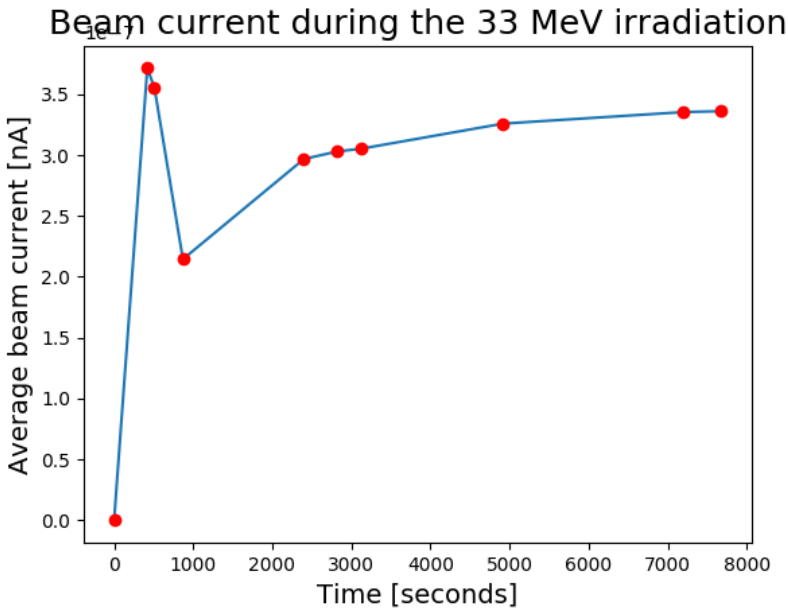

Figure 4.6: A plot of how the beam integrator changes during the irradiation run with 33 MeV deutrons. After 8 minutes, the beam was turned off for approximately 6 minutes because of missing cooling water.

At the end of the irradiation, the current integrator for the 16 MeV run was at 1182 coulombs and the Full-scale Amps setting (a scale on the current integrator) was $6 \cdot 10^{-6}$. For the 33 MeV run, the current integrator was at 4302 coulombs and the Full-scale Amps setting was $6 \cdot 10^{-7}$. These give an average deuteron beam current for each irradiation of:

$$\text{Beam current}_{16MeV} = \frac{1182 \cdot 6 \cdot 10^{-6}}{28620} = 247.7 \text{ nA} \tag{4.1}$$

$$\text{Beam current}_{33MeV} = \frac{4302 \cdot 6 \cdot 10^{-7}}{7340} = 353.1 \text{ nA} \tag{4.2}$$

After completed irradiation, the targets were removed from the end of the beam line. Before entering cave 0, where the irradiation took place, the dose levels in the cave were verified to be safe (< 1 mSv/hr) using a handheld Victoreen 451P ion chamber survey meter. When the dose fields in the cave dropped to safe levels,

the target holder was removed from the beam line. The targets were sealed in plastic bags to prevent the spread of contamination and brought to the counting room where they were counted using a high-purity germanium detector.

4.2 Gamma-ray spectroscopy

A lead-shielded ORTEC GMX-50220-S HPGe detector was used for counting the gammas for all samples in this experiment. This is a n-type germanium detector where the outer contact layer is doped with boron and lithium is used to dope the hole contact layer.

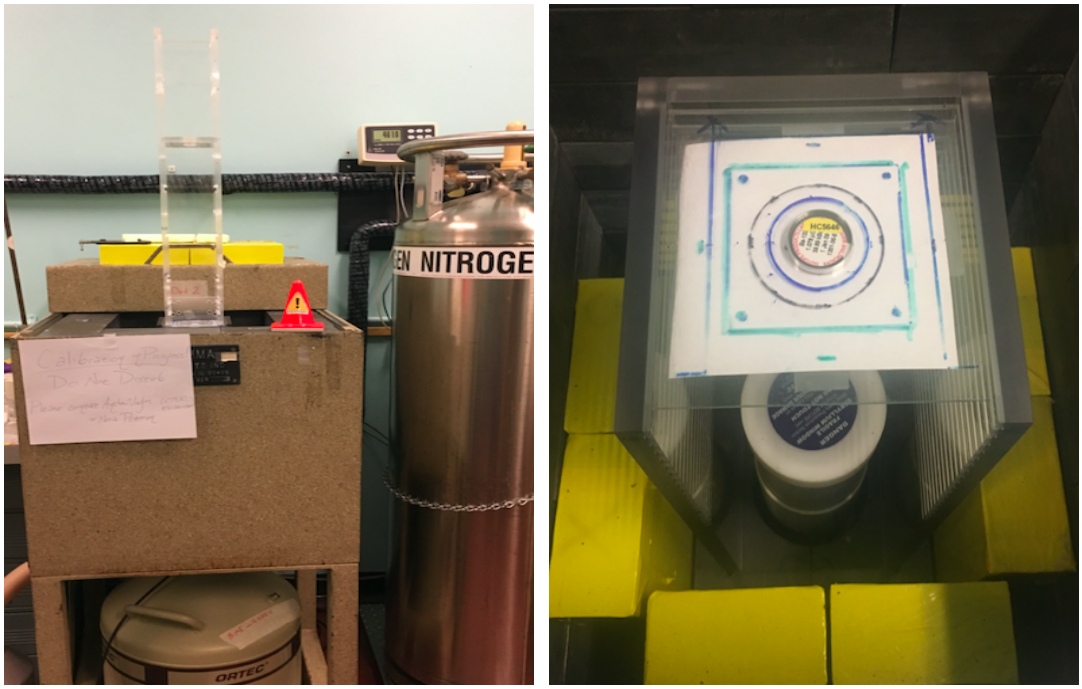

(a) (b)

Figure 4.7: Pictures of the germanium detector used for counting of the gamma-rays. (a) shows the ORTEC GMX-50220-S from the outside of its lead shielding and (b) shows the ORTEC GMX-50220-S and counting shelves from the inside of the shielding.

The counting started approximately 15 minutes after end of beam for both the 16 MeV and 33 MeV irradiations. To make sure that all of the short-lived products

were not lost, targets were initially counted for short live time and gradually moving to progressively longer count times. This made sure that all of the gammas that were of interest were detected. The targets and the calibration sources were counted with different heights from the detector. As figure 4.7a and 4.7b show, a plastic tower with different fixed shelf distances were placed over the detector in order to collect data from different heights repeatedly. In the counting process of the targets, shelves with 5 cm, 10 cm, 18 cm and 22 cm distance from the detector were used, all of which require calibration.

4.2.1 Energy and peak calibration

Before any measurements of the targets, an energy calibration had to be done. For this calibration, 1 µCi of: ^{137}Cs ($t_{1/2} = 30.08$) years [116], ^{133}Ba ($t_{1/2} = 10.551$) years [117] and ^{152}Eu ($t_{1/2} = 13.517$) years [118] standard sources were used. They have several well-known gamma lines with known energy listed in table Table A.1 and the sources used are shown in Figure 4.8. The relationship between the channel number and energy is linear and is obtained from a fit to:

$$E = a + b \cdot C \tag{4.3}$$

where E is the energy of the gamma, a is the intercept, b is the gradient of the line and C is the channel number of the center of the photo peak [32].

The detector was calibrated at every height that was used during counting of the targets from the experiments.

Both the energy and peak shape calibration were done in the gamma spectroscopy program FitzPeaks. Using the gamma-lines for the counting sources in Table A.1, the built-in function in the program calibrates the energy and peak shape for each shelves used in the counting process.

4.2.2 Efficiency calibration

The total efficiency of a HPGe detector is the number of detected events divided by the number of emitted events. To make an efficiency calibration of the detector shelves, the calibration sources with known gamma-energies and gamma branching ratio listed in Table A.1 were used. Since the total efficiency depends on both the shape and the density [32] it takes the intrinsic efficiency and the geometric

Figure 4.8: The calibration sources that were used in this efficiency calibration of the detector (Na-22 was not used in the calibration). Picture from private communication with Hannah Ekeberg.

efficiency into the calculation. The intrinsic efficiency is defined as the number of events registered per gammas strikes on the detector and the geometric efficiency is the fraction of the source radiation that is geometrically intercepted by the detector volume.

Solving Equation 2.20 and Equation 4.4, they are is used to calculate the efficiency ϵ_{eff} from every height of the detector that was used for counting our foils in this experiment:

$$\epsilon_{eff} = \frac{\lambda N_c}{A_0 I_\gamma (1 - e^{-\lambda \Delta t_c})(e^{-\lambda \Delta t_d})} \tag{4.4}$$

where λ is the decay constant, N_c is the number of counts in the fitted peaks, A_0 is the activity at a reference time, I_γ is the intensity of the γ, Δt_c is the counting time and Δt_d is the delay time since end of beam.

Equation 4.4 is an analytical efficiency that gives the efficiency for a given E_γ. When the activity of a given sample is unknown, the efficiency has to be interpolated to a model so that it gives a general efficiency that can be used for the unknown E_γ lines from this experiment. Together with the efficiency, this inter-

polated efficiency can be used to calculate activity in a sample by calculating the number of emitted events. The model used here is based on the work of Gallagher [119] where he and Cipolla measured the efficiency at several energies of Si(Li) and Ge(Li) detectors. This model takes the dead layer and the probability of interacting with the detector into account and the equation that is used in this model is given as:

$$\epsilon(E_\gamma) = B_0 \underbrace{e^{-B_1 E_\gamma^{B_2}}}_{\text{dead layer}} \underbrace{\left(1 - e^{B_3 E_\gamma^{B_4}}\right)}_{\text{detector volume}} \tag{4.5}$$

where the B-values are model parameters which represent the physical interactions of the γ-rays with the detector. Since Equation 4.5 is non-linear, the fitting of this model was done by minimizing χ^2 [119] which is an algorithm that measures how observed data compares to expectations within measurement uncertainties. More detail on χ^2 fitting is provided in Appendix B.

4.3 The 88-Inch Cyclotron

Berkeley Lab is located in the Berkeley hills, directly over the University of California, Berkeley, overlooking San Francisco Bay. Responsible for the invention of the cyclotron, as well as building the first cyclotron used to produce medical isotopes [34], Lawrence Berkeley National Laboratory still produces radionuclides that are a part of the research on the medical applications.

The 88-Inch Cyclotron at Berkeley Lab is used in research spanning multiple fields including astrophysics and nuclear structure. The accelerator is a 300-ton, K = 140 sector-focused cyclotron with the ability to run with both heavy (Z≤92) and light ions. The K-value characterizes the strength and radius of the cyclotron's magnetic field, and represents the maximum kinetic energy a proton can reach in the cyclotron and can be used to rescale the maximum energy for protons to other ions with a given charge-to-mass ratio:

$$E_k = AK(\frac{Q}{A})^2 \tag{4.6}$$

where A is the ion's mass number, Q is the charge state of the ion and E_k is the maximum energy that the ion can be accelerated to in the cyclotron. From Equation 4.6, using deuterium where A = 2 and Q = 1, the 88-Inch Cyclotron can accelerate deuterium particles up to 70 MeV.

4.3.1 Deuteron breakup process

Since an intense source of fast neutrons is needed to study their use in isotope production, the thick-target deuteron breakup neutron source was used in this work. This process has been studied by Meulders [120] and Saltmarsh [121] and it involves splitting deuterons into a proton and a neutron using a thick target of beryllium.

Deuteron breakup can be done on any material but natural beryllium has been used as a breakup target in this work, for several reasons. Beryllium is a dense metal and a good conductor of heat, it is impossible to produce a radioactive activation product using deuterium, it will only produce stable isotopes. Be has a low Z which is preferable for producing a harder breakup neutron spectrum, as neutrons from breakup on high-Z targets have a more downshifted spectrum. This is because the breakup protons are emitted at increased energy in high-Z targets due to enhanced "acceleration" during the breakup process within the Coulomb field of the target. There are no bound excited states in deuterium [122] and because of the low binding energy of 2.22 MeV [122], it will easily split into one proton and one neutron when it hits the beryllium target and excites it above its binding energy.

Deuteron breakup occurs through a combination of two main mechanisms: a direct "stripping" process, and excitation of the deuteron. The first one happens at higher energies when the deuteron interacts with a beryllium nucleus in the target and strips off the proton in a direct (d,n) reaction, allowing the residual neutron to pass through the beryllium target. At lower energies, the breakup process is dominated by excitation of the deuteron. If the deuteron is excited above its binding energy, this unbound state will decay by separating into its components, a proton and neutron. The energy distribution of the breakup neutron spectrum is illustrated in Figure 4.9 for breakup of 16 MeV and 33 MeV deuterons on a range of different breakup targets. At both energies, the neutron yield increases in magnitude and the spectrum shifts towards higher neutron energy for targets with a lower atomic number.

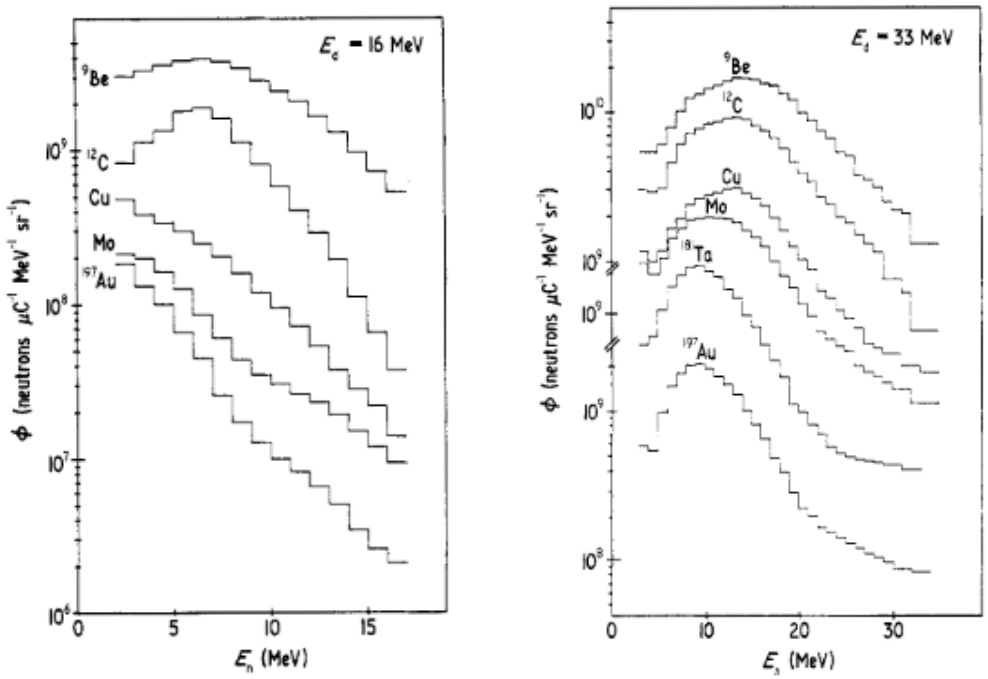

(a) (b)

Figure 4.9: Neutron energy spectra produced in deuteron breakup for (a) 16 MeV deuterons and (b) 33 MeV deuterons [120].

Figure 4.10 shows how the neutron energy varies with its emission angle (with respect to the deuteron beam) in the breakup process. At larger emission angles, the neutron spectrum decreases in magnitude, and becomes much "softer" (shifting towards lower energy) due to the disapperance of the "peak" observed at approximately half of the incident deuteron energy [120]. Even going from zero to ten degrees decreases the neutron flux by a factor of two. It is this sharp decline that is what gives the breakup spectrum its highly "forward-focused" nature. While this figure illustrates the 50 MeV breakup spectrum on a beryllium target, a similar energy-angle trend is observed for breakup at all deuteron energies. In this experiment the activation foils were positioned to give the smallest angle as reasonably possible (without sacrificing flux by moving to much farther distances), since both the neutron flux and energy will decrease with the angle [120].

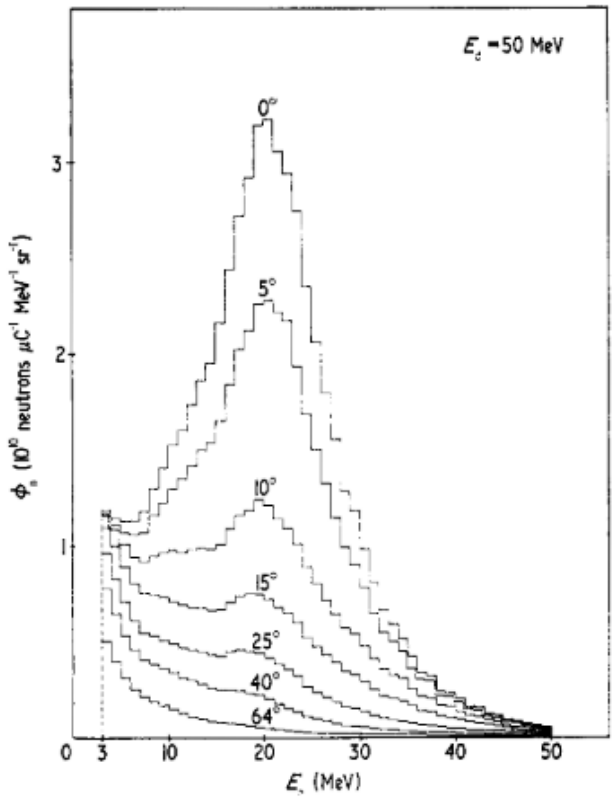

Figure 4.10: Illustration of the angular dependence of the neutron spectrum in deuteron breakup, for 50 MeV breakup on a beryllium target [120]. A similar energy-angle relation is observed for breakup at all deuteron energies, illustrating the forward-focused nature of the breakup neutrons.

The neutron spectra for 33 MeV and 16 MeV will have a similar shape at each angle as in Figure 4.10 but with spectrum endpoint shifted down in energy based on the incident deuteron energy. The spectra are expected to have an average neutron energy for the 16 MeV deuteron beam of approximately 6.5 MeV and approximately 16 MeV for the 33 MeV beam, whose spectra are shown in Figure 4.9.

4.4 Stack design

To measure the production of ^{64,67}Cu and other reaction products, as well as monitor the neutron flux at each position, a target stack was built, consisting

of five different natural targets, all purchased from Goodfellow, Zn (with an abundance 49.17% of ^{64}Zn, 27.73% of ^{66}Zn, 4.04% of ^{67}Zn, 18.45% of ^{68}Zn, and 0.61% of ^{70}Zn), Zr (with an abundance 51.45% of ^{90}Zr, 11.22% of ^{91}Zr, 17.15% of ^{92}Zn, 17.38% of ^{94}Zr, and 2.80% of ^{96}Zr), In (with an abundance 4.29% of ^{113}In, 95.71% of ^{115}In), Y (with an abundance 100% of ^{89}Y) and Al (with an abundance of 100% ^{27}Al). All foils were measured by mass, thickness and diameter, see Table 4.1, after they were cut into 1 cm diameter discs and sealed into small "packets" using Kapton tape, as shown in Figure 4.11. This was done to prevent the loss of any foil material during handling or irradiation, as since the targets were fragile, they could easily break. While sealed in Kapton tape, any scattered material from the activated foils is sealed inside, preventing the spread of contamination, and ensuring that no material is lost prior to counting, which would systematically shift the magnitude of all activities counted in that foil.

Figure 4.11: Picture of how the targets were sealed before irradiation. From the top left to right: Zn, NaCl, Zr and bottom left to right: In, Y, Al. The NaCl target was there for a different experiment.

The Kapton tape used in this work is 3M 5413-Series Kapton polyimide film tape. For each target we measured their mass, weight, thickness and length, and width to calculate the areal density of each target. The targets were each attached to a 1.6 mm-thick plastic frame (over a 3 cm circular aperture in the frame) and were placed in the end of an aluminum target holder box. The targets were placed with 10 cm between the beryllium breakup target (3.5 mm thick) and first foil in the stack, and approximately 3 cm thickness of empty frames were placed as thermal spacers behind the foils. This position was chosen as a good compromise between the planar angle and neutron flux for the foil stack. A metal spring was

Target	Diameter [mm]	Thickness [mm]	Mass [mg]	Areal density [g/cm^2]
Al 01	12.90 12.86 12.89	0.830 0.852 0.830 0.831	258 257 257	0.19700 ± 0.00055
Al 02	12.93 12.97 12.83 13.02	0.882 0.901 0.842 0.890	258 256 255	0.19600 ± 0.00160
Zn 01	12.45 12.51 13.26	1.044 1.031 1.061 1.043	648 848 854	0.66300 ± 0.02400
Zn 02	12.89 12.66 13.10	1.041 1.077 1.023 1.058	842 843 839	0.64600 ± 0.01100
Zr 01	12.37 12.21 12.34	1.098 1.086 1.080 1.093	756 757 755	0.63600 ± 0.00450
Zr 02	12.34 12.35 12.23	1.119 1.163 1.116 1.134	755 757 755	0.63500 ± 0.00360
Y 01	12.65 12.65 12.65	1.195 1.195 1.195	507 506 503	0.40200 ± 0.00170
Y 02	11.80 11.80 11.80	1.151 1.151 1.151	466 466 465	0.42600 ± 0.00053
In 01	13.90 14.15 14.19	0.255 0.255 0.255	275 280 278	0.18000 ± 0.00440
In 02	13.83 14.17 13.89	0.255 0.255 0.255	270 273 274	0.17800 ± 0.00270
In 03	13.95 14.16 14.19	0.255 0.255 0.255	277 275 275	0.17700 ± 0.00180
In 04	13.99 13.73 13.91	0.255 0.255 0.255	271 268 267	0.17800 ± 0.00220

Table 4.1: Characterization of the targets used in this thesis.

placed between the Be target at the foil stack, to ensure that the foils did not shift position during the irradiation. A photograph of the assembled 16 MeV stack is shown in Figure 4.5a.

Chapter 5

Analysis

> If you ever start thinking too seriously, just remember that we are talking monkeys on an organic spaceship flying through the universe.
>
> — Joe Rogan

5.1 Analysis of gamma spectra

FitzPeaks

FitzPeaks Gamma Analysis and Calibration Software was the program used in this thesis work for gamma spectroscopy analysis [123]. The performance of the peak fitting process is using the SAMPO method [124]. It is a mathematical algorithm that uses the first and second derivative of the spectrum to fit the peaks. The first derivative changes the sign at the centroid of the peak and the second derivative finds the minimum at the centroid [32, p. 186]. The peaks are fitted to a Gaussian distribution with an exponential tail on both sides of the peaks [32, p. 186]. In this kind of a fit, the area under the curve, position and width are determined at the same time by using nonlinear least square fit on all the peaks [32, p. 192].

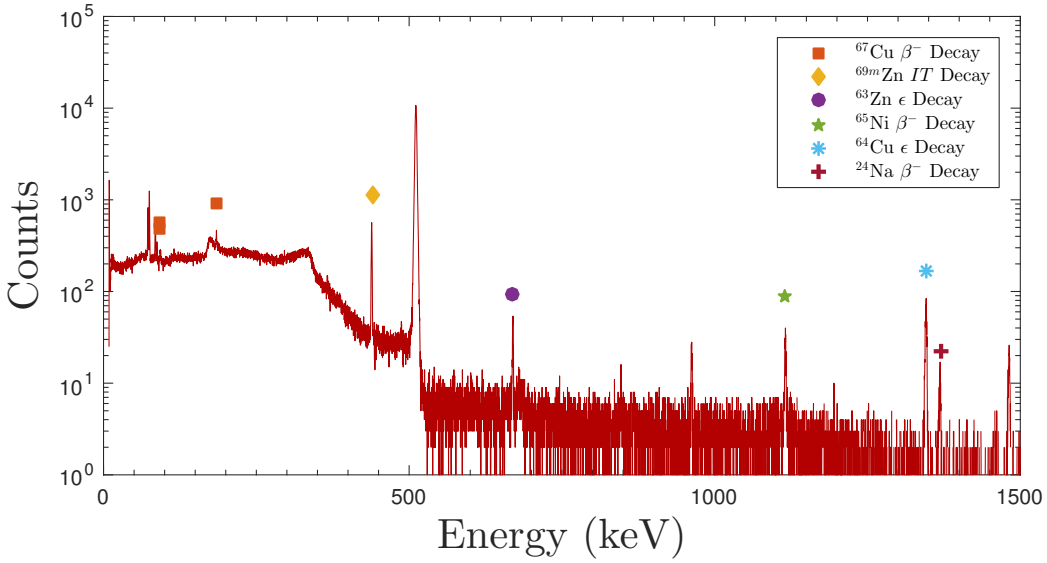

Figure 5.1: Figure of an example spectrum collected in this experiment looks like, in this case it is a spectrum of the activated zinc targets from this experiment.

Adding a gamma spectrum into fitzpeaks, allows the fitting of each peak in the spectrum. This is done automatically, except if a peak doesn't have a Gaussian shape. This can occur if there are multiple overlapping peaks with approximately the same energy. Manually, the peak(s) are evaluated to be one single peak or two peaks. After the program has gone through all the peaks in the gamma spectrum, a fitzpeaks report is created, an example shown in Figure 5.2. The report contains information on the date of the irradiation, live time, peak energy, centre channel, FWHM of the peak, significance, goodness of fit, peak area (number of counts), relative uncertainty of peak area and detection rate.

be used for evaluation purposes

14-Mar-2019 11:15

P E A K F I T R E P O R T

Spectrum file Analysed: AB0811118_10cm_Zn01.Chn
Sample Title : Cs137

Spectrum saved on 25-Oct-2018 at 16:15 Collected on 12-Aug-2018 at 12:19
Sample Taken on 12-Aug-2018 at 12:19 Decayed 0 Days, 0 mins.

Detector file number used: 1
Energy Calibration Performed on 13-Mar-2019 at 17:27
Peak Shape Calibration Performed on 13-Mar-2019 at 17:31

Datetime: 12-Aug-2018 12:19
Live: 5510.00
Mass: 130
Shelf: 10

Reported Activity values were rounded
FitzPeaks Version: 3.71 23rd January 2014

Peak Energy	Centre Channel	FW@HM (KeV)	Signif	Goodness of Fit	Peak Area	% Uncert.	Gammas per sec.	% Uncert.	2 Sigma Background
72.7	388.4	0.94	15.5	1.05	3073	6.3	5.5769e-01	6.3	2213
74.8	400.1	0.94	22.7	1.05	5349	4.1	9.7082e-01	4.1	2459
84.7	452.8	0.96	10.0	0.92	2118	7.8	3.8444e-01	7.8	2266
87.3	466.8	0.96	5.4	0.92	643	22.2	1.1667e-01	22.2	2266
184.6	985.8	1.07	5.4	1.08	778	24.4	1.4128e-01	24.4	3423
366.4	1955.9	1.28	3.6	1.16	237	48.9	4.2953e-02	48.9	1264
438.7	2341.8	1.37	22.0	0.84	3915	3.6	7.1054e-01	3.6	455
511.0	2727.9	3.08	39.4	37.05	173480	0.9	3.1485e+01	0.9	3374
669.7	3574.9	1.62	7.4	0.96	416	11.5	7.5463e-02	11.5	69
846.5	4518.8	1.82	3.8	0.89	67	43.9	1.2185e-02	43.9	56
962.1	5135.6	1.95	5.8	1.16	267	14.1	4.8430e-02	14.1	35
1115.5	5954.2	2.12	6.4	1.13	358	12.6	6.4926e-02	12.6	50
1345.6	7182.5	2.45	10.7	0.92	1031	6.1	1.8710e-01	6.1	18
1368.5	7304.5	2.40	4.8	0.70	161	18.3	2.9189e-02	18.3	20
1481.6	7908.4	2.53	6.4	0.81	307	11.8	5.5698e-02	11.8	16
2753.7	14697.7	3.97	3.8	0.58	81	33.5	1.4653e-02	33.5	3

Figure 5.2: An example of a fitzpeaks report

From a FitzPeaks report such as the one in Figure 5.2, the peak energy was used to identify what kind of isotopes were made during the irradiation. When the isotope was identified, its decay radiation dataset was looked up (from its most recent evaluation) to find the intensity of the gamma, the uncertainty of the intensity and half-life. Information from the FitzPeaks report and the knowledge of the different isotopes that were created were then used to calculate how much activity that was made of the different isotopes during the irradiation.

Peak fit uncertainty

Since the peaks are fitted as a Gaussian peak, it gives rise to systemic and statistical errors. Since radioactive decay follows Poisson distribution, the probability of observing N events is [31, p. 85]:

$$P(N) = \frac{\mu^N e^{-\mu}}{N!} \tag{5.1}$$

where μ is the expected mean value of the decay rate and is equal to the variance $\sigma^2 = \mu$ [31, p. 86]. The Poisson distribution is dependent on μ and is not a symmetric distribution. It will, however, be more symmetric and approach a Gaussian distribution when μ gets large.

The uncertainty gets smaller when the number of counts in the peak gets higher. The statistical uncertainty in a channel of the detector can be approximated to the whole peak.

$$\text{Statistical uncertainty} = \frac{\sqrt{\delta_{N_i}}}{N_i} = \frac{1}{\sqrt{N}} \tag{5.2}$$

To reduce the statistical uncertainty, an energy-peak were aimed to have 10 000 count ($i = 10\ 000$) so that the relative uncertainty would be less than 1%.

5.2 Peak counts to activity since end of beam

Using Equation 2.21 along with a self-attenuation correction, the activity since end of beam can be calculated as:

$$A(\Delta t_d) = \frac{\lambda N_c}{\epsilon_{eff} I_\gamma (e^{-\lambda \Delta t_d})(e^{-\mu \rho \Delta r/2})} \tag{5.3}$$

where ϵ_{eff} is the efficiency of the detector, I is the intensity of the gamma per decay, μ is the photon attenuation coefficient from XCOM database on photon cross section [125] and $\rho \Delta r$ is the areal density of the foil.

Knowing the half-life and number of counts of each of the different produced isotopes from the FitzPeaks reports, the activity at some time Δt_d after end of beam can be calculated using Equation 5.3.

FitzPeaks in the reports are shown in Figure 5.2 and gives information needed to identify each peak for the zinc, zirconium, yttrium, Indium and aluminum foils for both 16 MeV and 33 MeV and are listed in Table C.1 - Table C.5. Using the number of counts, N_c, along with the uncertainty for each foil in the peak fit reports, the I_γ and the uncertianty from Table C.1 - Table C.5, the efficiency from Equation 4.5, the areal density from Table 4.1 and μ from XCOM photon cross section database [126] in Equation 5.3, the activities for a specific product as a function of time since end of beam was calculated.

Parent-daughter relationship

When a radioactive nucleus decays, it can decay into a stable or unstable daughter. The parent, A_p is decaying with a decay constant λ_p and the parent activity follows [127, p. 40]:

$$A_p(t_d) = A_0 e^{-\lambda_p t_d} \tag{5.4}$$

where A_0 is the activity at end of beam and t_d is the time since end of beam. Figure 5.3 shows how the activity decreases where there is no feeding from another decaying isotope.

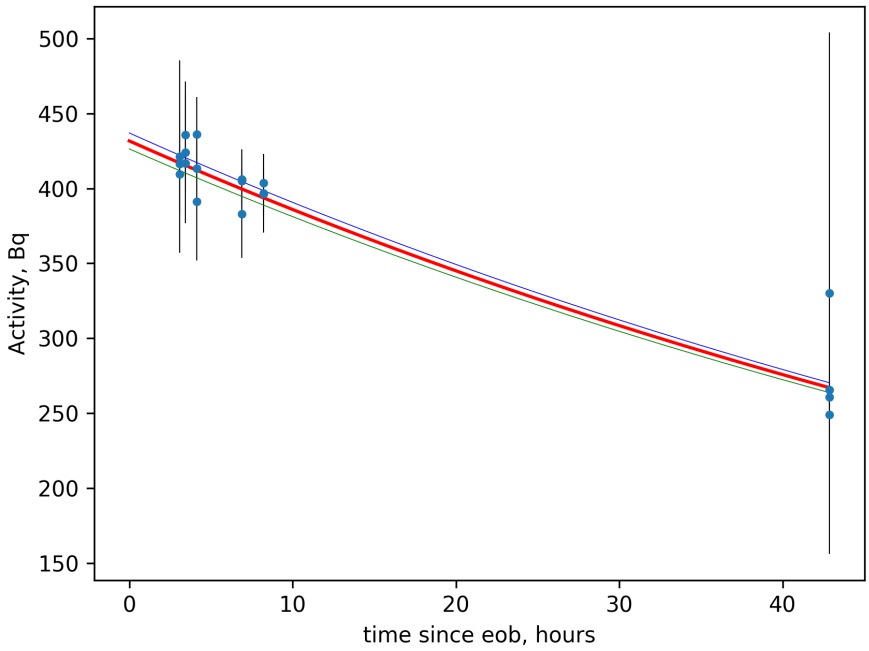

Figure 5.3: The activity of ^{67}Cu in an activated zinc target as a function of time since end of beam, for the 33 MeV irradiation.

However, for a multiple decay chain, the Bateman equation Equation 5.5 [128] gives the activity of the daughter in a parent-daughter mixture. The fact that the parent is decaying and produces more daughters at the same time as the daughter is decaying makes it more tricky, and is given as:

$$A_n = \lambda_n \sum_{i=1}^{n} \left[\left(A_{i,0} \Pi_{j=1}^{n-1} \lambda_j \right) \cdot \left(\sum_{j=1}^{n} \frac{e^{\lambda_j t}}{\Pi_{i \neq j}^{n} (\lambda_i - \lambda_j)} \right) \right] \tag{5.5}$$

the equation sums over all nuclei in a decay chain, where A_n is the activity of a nuceli n in a decay chain and λ_n is the corresponding decay constant. In this work, single and double decay (n=1,2) were detected and Equation 5.5 can be simplified to:

$$A_d(t) = \lambda_n [A_{d,0} \lambda_1 \frac{e^{-\lambda_1} + e^{-\lambda_d}}{\lambda_p - \lambda_d} A_{d,0} e^{-\lambda_d t}] \tag{5.6}$$

where d is daughter and p is parent nucleus.

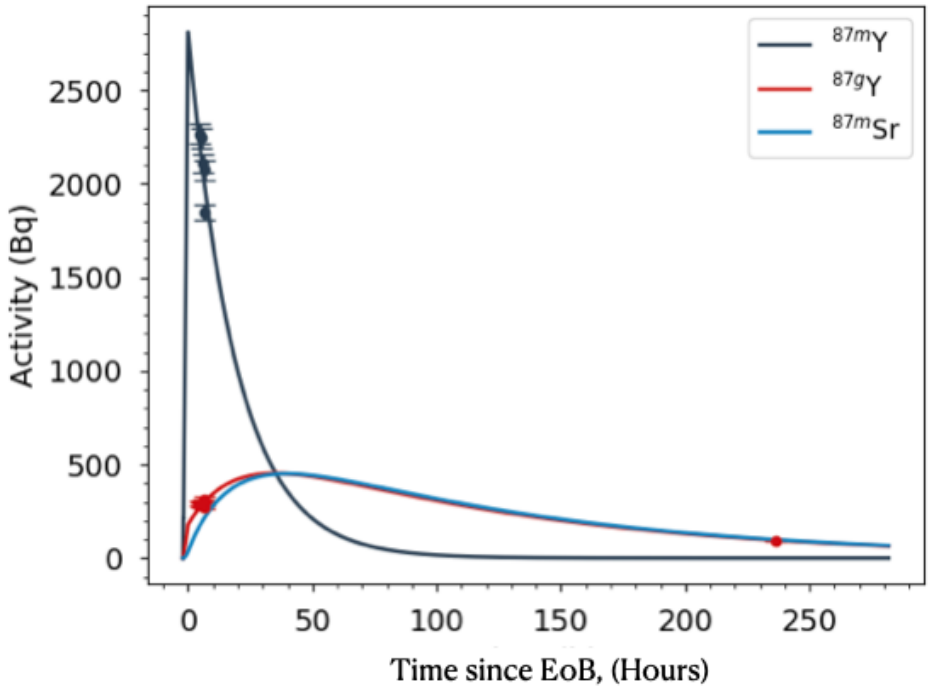

Figure 5.4: Decay of the parent, ^{87m}Y, daughter ^{87g}Y, and granddaughter ^{87m}Sr (not directly observed) produced in the irradiation of an activated yttrium target, for the 33 MeV irradiation.

Figure 5.4 shows an example of what the activity curve looks like when the parent decays down to an unstable daughter with a longer half-life. The parent, in this

case ^{87m}Y, has a half-life of 13.37 hours [129] and its daughter, ^{87g}Y has a half life of 79.8 hours [129]. ^{87m}Sr has an isomer with a half-life of 2.815 hours [129] and is the granddaughter to ^{87m}Y which implies that $n = 3$ in Equation 5.5. Even though the gamma lines for ^{87m}Sr were not observed, the prediction of the activity that was expected to be seen, is also a part of the activity plot in Figure 5.4.

5.3 Production of isotopes

The number of nuclei produced follows the differential equation:

$$dN = Rdt - \lambda N dt \tag{5.7}$$

where N is the number of nuclei and λ is the decay constant of the nucleus. R is the rate of production and is dependent on the average flux of the beam, Φ, the reaction cross section, σ and the number of target nuclei, N_T. R can then be written as:

$$R = \Phi \sigma N_T \tag{5.8}$$

Solving Equation 5.7 gives:

$$N(t) = \frac{R}{\lambda}(1 - e^{-\lambda t}) \tag{5.9}$$

The instantaneous decay rate of a radioactive sample is defined as the total activity of the nucleus:

$$A(t) = \frac{-dN}{dt} = \lambda N \tag{5.10}$$

Using Equation 5.10 and putting it in for $N(t)\lambda$ in Equation 5.9 gives:

$$A(t) = R(1 - e^{-\lambda t}) \tag{5.11}$$

Replacing R with Equation 5.8 in Equation 5.11, and at the end of beam $A(t_{irr}) = A_0$:

$$A_0 = N_T \sigma \Phi (1 - e^{-\lambda t_{irr}}) \tag{5.12}$$

This assumes either that the neutron spectrum is monoenergetic or that Φ represents an average flux.

Equation 5.12 can be used to find the average cross section for production assuming a monoenergetic beam during the irradiation and can be written as:

$$\sigma = \frac{A_0}{N_T \Phi (1 - e^{-\lambda t_{irr}})} \tag{5.13}$$

Monitor foils

Knowing the neutron flux on each target is important for the calculation of cross sections. The deuteron current is known from the beamline current integrator, and the neutron flux on each target were measured in this experiment through the use of monitor foils.

There is well characterized data across the neutron energy range in this experiment for different monitor reactions. These are trusted for neutrons and were used to determine the average neutron flux based on each reaction. These reactions have peaks at different areas of the spectrum, and as a consequence, the average neutron flux can be calculated. After finding the average neutron flux on the monitor foils, the cross section can be calculated. Since the monitor reactions have well known cross sections, by comparing the International Reactor Dosimetry and Fusion File (IRDFF) [130] database cross sections with the calculated cross sections for the monitor reactions, the results from this experiment can be calculated with confidence that they are correct. The monitor reactions used in this thesis:

Target	Reaction route
Yttrium	^{89}Y(n,2n)^{88}Y
Aluminum	^{27}Al(n,x)^{24}Na
Zirconium	$^{\text{nat}}$Zr(n,x)^{89}Zr

Table 5.1: The monitor reactions used in the calculation of average neutron flux.

Initially, indium was included in the stack as one of the monitor foils with the monitor reactions ^{113}In(n,2n)^{112m}In, ^{115}In(n,n')^{115m}In, ^{113}In(n,n')^{113m}In and ^{115}In(n,2n)^{114m}In. But these reactions are very sensitive to population through thermal neutron capture and since thermal neutrons are present during irradiation (produced by room-return), these cross sections will shift the average neutron flux down and thus make the spectrum average cross section apparently larger than it actually is. For this reason, all indium monitor reactions were excluded from the calculation of the average neutron flux.

5.4 Finding the average neutron flux

For the case of deuteron breakup the spectrum is not monoenergetic, it is a broad spectrum and therefore, from Equation 5.12 the A_0 can more accurately be written as:

$$A_0 = N_T \Omega (1 - e^{-\lambda t_{irr}}) \int \sigma(E) \frac{d\phi}{dE} dE \tag{5.14}$$

where $\frac{d\phi}{dE}$ is the flux distribution, $\sigma(E)$ is the energy dependent average cross-section, and Ω is the solid angle subtended by a foil. The integral in this equation accounts for the different production rates as a function of neutron energy.

Given the energy-dependent monitor cross sections (from IRDFF) and a spectral shape for the neutron flux obtained by Morrell(New data listed in Appendix D) and Harrig [131], the expected activity after a certain length of time was calculated. The observed activity for the monitor data was used to calculate the intensity of the neutron flux that produced that activity. Using Equation 5.14, the average neutron fluxes for each of the monitor channels can be found:

$$\phi_{avg} = \frac{A_0}{N_T \Omega (1 - e^{-\lambda t_{irr}}) \int \sigma(E) \frac{d\phi}{dE} dE} \tag{5.15}$$

Similarly, the flux-weighted average energy for neutrons in Equation 5.16 is used to calculate the average flux energy for each of the foils:

$$E_{avg} = \frac{\int E \cdot \frac{d\phi}{dE} dE}{\int \frac{d\phi}{dE} dE} \tag{5.16}$$

This E_{avg} is used as the average energy when plotting the calculated cross sections for each foil.

Equation 5.15 and Equation 5.16 were used for the monitor channels to find the average value of the flux and neutron energy for each foil. The average energy and the FWHM of the energy distribution was used to characterize the spectrum when reporting the results of this very broad-energy irradiation spectrum.

The uncertainty on the weighted average flux is the total uncertainty and combines both the systematic uncertainty and the statistical uncertainty. The systematic uncertainty is the observed spread in the reaction fluxes, calculated as the standard deviation of all monitor fluxes. The statistical uncertainty is that the spectrum is broad and every reaction samples a different energy location, calculated as the

propagated uncertainty in the weighted average neutron flux. This is done to make sure that the uncertainties in the cross sections we report reflect that this is a broad spectrum.

Comparison of neutron flux spectra

The data on neutron flux for both 16 and 33 MeV deuteron breakup from Meulders [120] collected in 1974 does not include deuteron breakup energies lower than 3 MeV. With that knowledge, data from an experiment done on 16 MeV deuteron breakup in 2018 by K. Harrig, at al. [131] and physically-informed re-normalization of Meulders data, using foil activation with 33 MeV neutron flux by Jonathan T. Morrell [132], are being compared with Meulders data. This will give a better insight on why the newer data gives a more accurate cross sections results in this analysis.

As Figure 5.5 shows, the average energy for the Harrig data measures down to a lower threshold than the Meulders paper was able to measure. This means that the neutrons with energy bellow 3 MeV are ignored by using the Meulders data. Looking at the Harrig data, there are a lot of neutrons in the 1-3 MeV region that contribute to a rise in neutron flux, and as a consequence, the cross section will go down for reactions which dominate in this low-energy region. Additionally, the overall magnitude of the Harrig spectrum is significantly smaller, relative to the Meulders data.

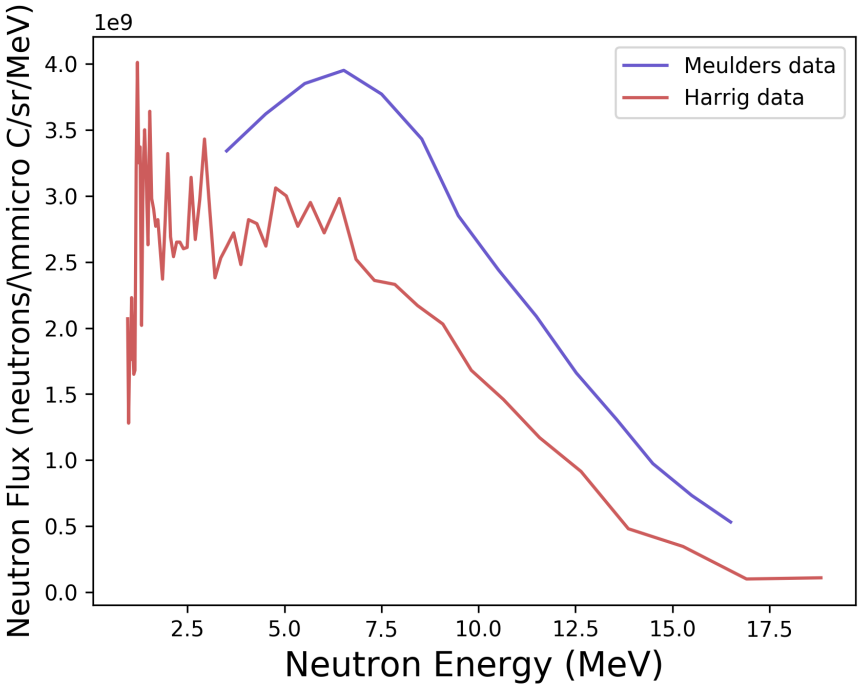

Figure 5.5: Comparison of Meulders [120] and Harrig [131] 16 MeV deuteron breakup neutron spectra. In addition to a smaller magnitude, the Harrig data shows additional low-energy structure to the spectrum, and an overall softer spectrum than Meulders.

The neutron spectra that is used for 33 MeV deuteron breakup, is based on an on-going work by Morrell [132] and while it has not yet been published, the data has proven in this work to be better for cross section measurements. The data used is listed in a table in Appendix D. A comparison of the Meulders data with Morrells data is shown in Figure 5.6. The new data from Morrell includes the lower energies not observed in the work of Meulders. The magnitude of the spectra is also renormalized relative to the Meulders data, and therefore, the cross section value will not change as much for 33 MeV as it did for 16 MeV with Harrigs data.

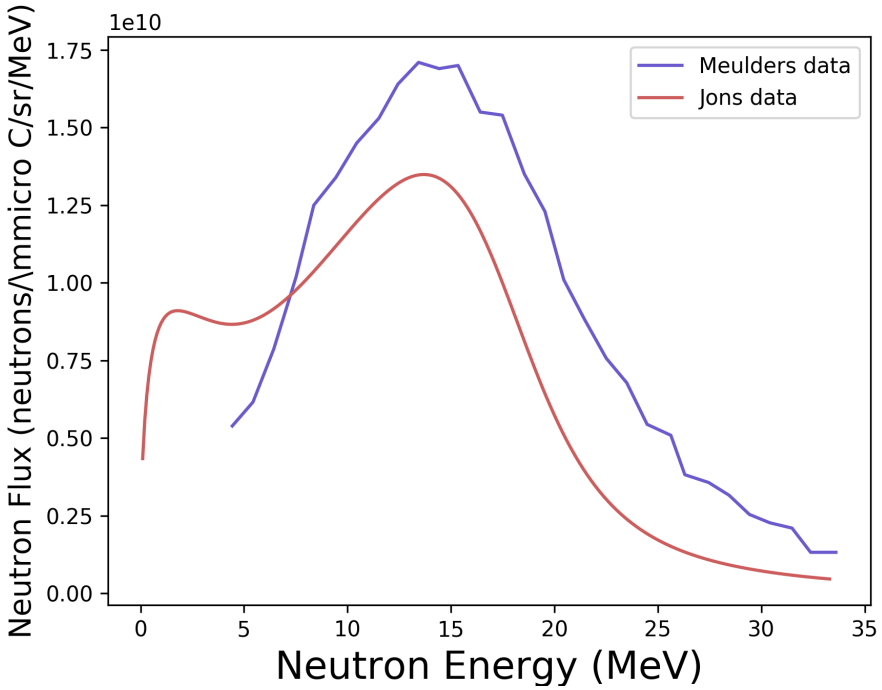

Figure 5.6: Comparison of Meulders [120] and Morrell's [132] 33 MeV deuteron breakup neutron spectra. In addition to a smaller magniude, the Morrell data shows additional low-energy structure to the spectrum, and an overall softer spectrum than Meulders.

Selection of neutron spectra for analysis

A comparison is done to make a better justification for why the new data from Harrig [131] and by Jonathan T. Morrell [132] are used instead of the Moulders data when the calculations of the results are done in this thesis. Figure 5.7 shows how the average neutron flux and the individual neutron fluxes for the monitor foils were impacted by the selection of neutron spectrum. For Figure 5.7a the agreement of the individual fluxes improved when switching away from Meulders data to data from Harrig and Morrell.

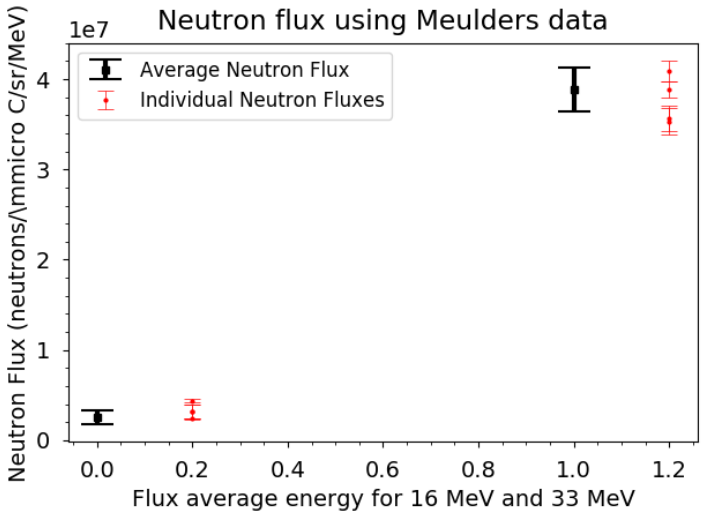

(a)

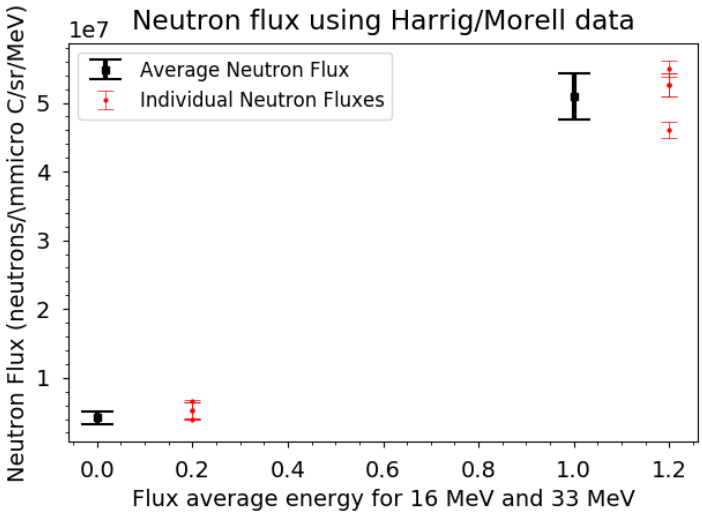

(b)

Figure 5.7: A plot of the neutron flux for the monitor foils, where the two points on the left side in the plots is with neutron flux with an energy of 16 MeV and the points on the right side is for 33 MeV neutron flux. (a) is the average and individual neutron fluxes using Meulders data. (b) the fluxes using Harrig and Morrell's data from newer experiments.

Using this knowledge, the Harrig data [131] at 16 MeV neutron flux and Jonathan T. Morrell's [132] unpublished data for 33 MeV neutron flux will be the spectra

used in the results of this thesis.

5.5 Spectrum-average cross-section

To calculate the cross sections, the average flux is used as shown in Equation 5.15. Since the spectrum is broad the cross section is, by consequence, flux weighted average cross section and is given as:

$$\sigma_{avg} = \frac{\int \sigma(E) \cdot \frac{d\phi}{dE} dE}{\int \frac{d\phi}{dE} dE} \tag{5.17}$$

Equation 5.17 is the equation used for the final results that are discussed in chapter 6.

Thick-target yield and purity

The spectrum-average cross section is determined by thick-target yields and purity of the sample, therefore they are two important factors to discuss.

Production yield

The production yields gives an easy comparison when discussing different production pathways. Comparing the cross sections was not enough because other things have to be taken into account such as purity of the targets.

The production yields are a even comparison between the pathways. Since there is no (direct) use of charged particles in this experiment, the units of the production rates for this experiment will be different from a production yield of charged particles. The charged particle yields are reported in units of (mCi/µ Ah) and (MBq/µAh) and we reported (mCi/µ A/g/sr), which can be calculated as:

$$\text{Production yield} = \frac{\frac{A_0}{(1-e^{-\lambda t_{irr}})}}{\text{D-current} \cdot \text{target mass} \cdot \text{target solid angle}} \tag{5.18}$$

where $\frac{A_0}{(1-e^{-\lambda t_{irr}})}$ is the production rate. A_0 is in the units of MBq, by multiplying A_0 with $3.7x10^7$ the units becomes mCi.

The units for charged particles are a better comparison as our production was based on neutrons as a secondary beam. To get units that are easier to compare to other experiments done with traditional charged-particle production of producing ^{64}Cu and ^{67}Cu. The units mCi / µ Ah and MBq/µAh is based on the assumption of $t_{irr} = 1$ hour. The equation for production yield in mCi/µAh and MBq/µAh is used:

$$\text{Production yield} = \frac{\text{Production rate} \cdot (1 - e^{-\lambda \cdot t_{irr}=1\text{hour}})}{\text{D-current}} \tag{5.19}$$

Even reporting in these units, it is not a perfect comparison because in this experiment, not all deuterons breakup and produce neutrons which hit the target.

Using a neutron source as a beam with a certain flux, this is how much activity that is expected:

$$\text{Neutron yields} = \frac{\text{Production rate}}{\text{Neutron flux}} \tag{5.20}$$

Purity

The isotopic purity and radionuclidic purity are used to evaluate the purity of a medical isotope after the chemical purification. Since no radiochemical purification was part of this thesis, looking at these purities before the purification process gives an estimate on how pure our production path is, assuming everything but copper are removed.

The isotopic purity (IP) is the number of nuclei produced for isotope of an element over the sum of nuclei of all isotopes of the same element. Isotropic purity gives information on how many actual nuclei there is in a sample and how many chelators that can bind to the product. Radionuclidic purity (RNP) is the activity of an isotopes over the sum of all activities of all isotope of the same element and is used for patient dose calculation. These are defined as[133]:

$$IP = \frac{N_{(^{A}X)}}{\sum_i N_{(^{i}X)}} \quad \text{and} \quad RNP = \frac{A_{ct_{A_X}}}{\sum_j A_{ct_{j_X}}} \tag{5.21}$$

where N is the number of nuclei in a sample, X is the element, A is the mass number and A_{ct} is the activity of the nuclide.

The isotopic and radionuclidic purity are evaluated in this experiment for copper

observed by gamma spectroscopy. Since Both IP and RNP changes with function of time due to the decay rates in the different products, the common report time is one hour after EoB.

Chapter 6

Results and discussion

> I am ready to face any challenge that might be foolish enough to face me.
>
> — Dwight Schrute

In this thesis, the cross sections for production of ^{64,67}Cu through the $^{\text{nat}}$Zn$(n,x)^{64,67}$Cu reactions have been measured. To contribute to the production of ^{64,67}Cu in hospitals and other small cyclotrons using the deuteron break-up technique, the deuteron beam energies that optimize production of the two isotopes must be established. The measurements of cross sections and a discussion of ^{64,67}Cu are presented in section 6.2. In addition to the two Cu channels, we also present cross section measurements on natural Zn, Zr, In, Y and Al targets. Of these, 13 out of 33 reaction channels are first reported measurements. The cross section measurements for the monitor foils are described in section 6.1 and results for the remaining reaction channels are discussed in Appendix E.

The cross section measurements are compared with other experimental data where they exist and the reaction modelling codes ALICE-2017, TALYS-1.9, TENDL-2019, EMPIRE-3.23 and CoH-3.5.3 [7, 8, 8–10]. These models are used in many applications to calculate reaction cross sections over a large range of energies.

6.1 Cross section results for monitor reactions

As discussed in chapter 5, the neutron spectrum were used in the calculation for spectrum-average cross sections. The spectrum-average cross sections calculating using the neutron spectra from both Harrig/Morrell data and Meulders data are shown in Figure 6.1. To be able to compare these two monitor reaction results with the modeling codes and IRDFF, the cross sections for the modeling codes had to be calculated as spectrum-average cross sections using Equation 5.15. Together with IRDFF these spectrum-average cross sections provides a better comparison of our results.

Comparing the data from other experiments with these monitor reactions, the measurements in this experiment shows overall good agreement. Using the newer neutron spectra shows that the data from Harrig [131] and Morrell [132] in Figure 6.1b Figure 6.1d and Figure 6.1f, which account for the low-energy component of the neutron spectrum, gives a better agreement with the cross sections. They agree better with both the modelling results and the previous experimental data points. This indicates that the newer spectra represent a better picture of foil activation using deuteron breakup than the older data from Meulders.

Figure 6.1e and Figure 6.1f illustrate one monitor reaction where the data from Greenwood [134] do not agree with both the modelling codes, IRDFF and the measured cross section in this experiment. Since the single measurement from Greenwood was performed in 1987 and there is no other experimental data for this reaction, it is unclear if this discrepancy is due to an error in the original Greenwood measurement, or an needed update on the IRDFF evaluation. With that in mind, the data from out measurements agrees with both IRDFF and all of the modelling codes, that indicates that our measurements are more reliable, until further measurements on this channel.

Since the data from this experiment agrees with the spectrum-averaged monitor cross sections using Harrig and Morrell data for 16 and 33 MeV deuteron breakup, and because the new spectra show better consistency, the final cross sections calculated using Harrig and Morrell data will be reported here for the rest of the results. Similar behavior of this impact is seen in many product channels, but one specific example on the difference in cross section measurement by using Meulders or the Harrig/Morrell data is given in section 6.2.

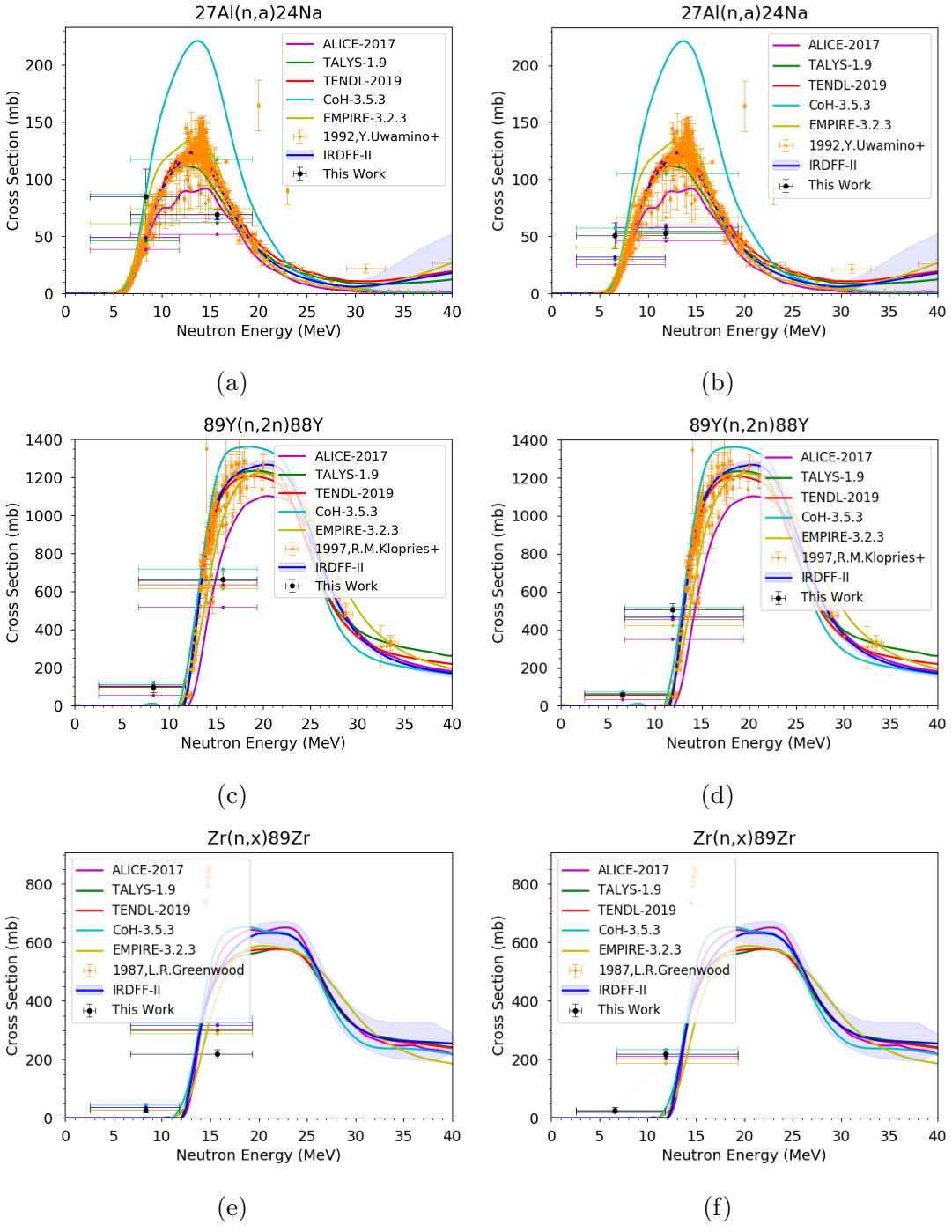

Figure 6.1: Plots of the observed cross section for the monitor reactions from this work together with modeling codes and other experimental data from EXFOR [135]. Figures (a), (c) and (e) are calculated using breakup neutron spectra from Meulders [120], and (b), (d) and (f) using the newer data from Harrig [131] and Morrell [132].

6.2 Cross section results for ^{64,67}Cu

The cross section for ^{nat}Zn$(n,x)^{64}$Cu reaction is both the Meulders data [120] shown in Figure 6.2a, and with the newer data on 16 MeV neutrons from Harrig [131] and improved data on 33 MeV neutron flux produced by Morrell [132] in Figure 6.2b. A comparison of these figures shows a shift of the average neutron energy to lower energies. This low-energy component normalizes the spectrum and an overestimation of the cross section was avoided, compared to Figure 6.2a. The measured data points from this work in Figure 6.2b show good agreement with other data points from Uwamino et al. [136] and the modelling results, compared to Figure 6.2a. EMPIRE is the only modelling code that does not show good agreement with experimental data and the other simulations codes.

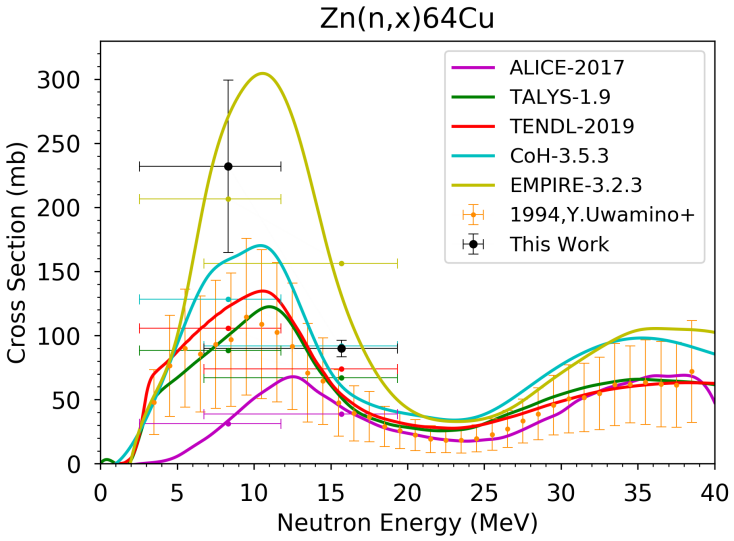

(a)

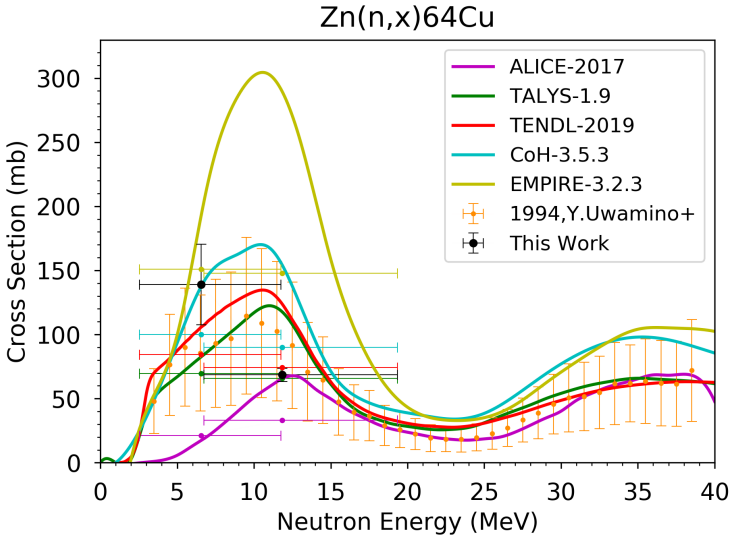

(b)

Figure 6.2: Comparison of spectrum-averaged cross sections for ^{64}Cu in this work where (a) shows the cross section calculated using Meulders neutron spectra [120], (b) is the cross section calculated with the new data from Harrig [131] and Morrell [132], with literature data from [136] for comparison. The new spectra show improvement in agreement with modeling results and literature data.

The cross section for $^{\mathbf{nat}}\mathbf{Zn}(n,x)^{\mathbf{67}}\mathbf{Cu}$ reaction is shown in Figure 6.3, there

is no other experimental data using neutrons to produce ^{67}Cu from natural zinc. The result in this work show good agreement with the modeling codes, and in particular ALICE. The spectrum-average cross sections for the modeling codes are within the same magnitude, except for EMPIRE, which overestimates this channel relative to the rest. This data show that producing ^{67}Cu on natural zinc, using deuteron breakup is a potential pathway for production with higher ^{67}Cu production with higher deuteron energies.

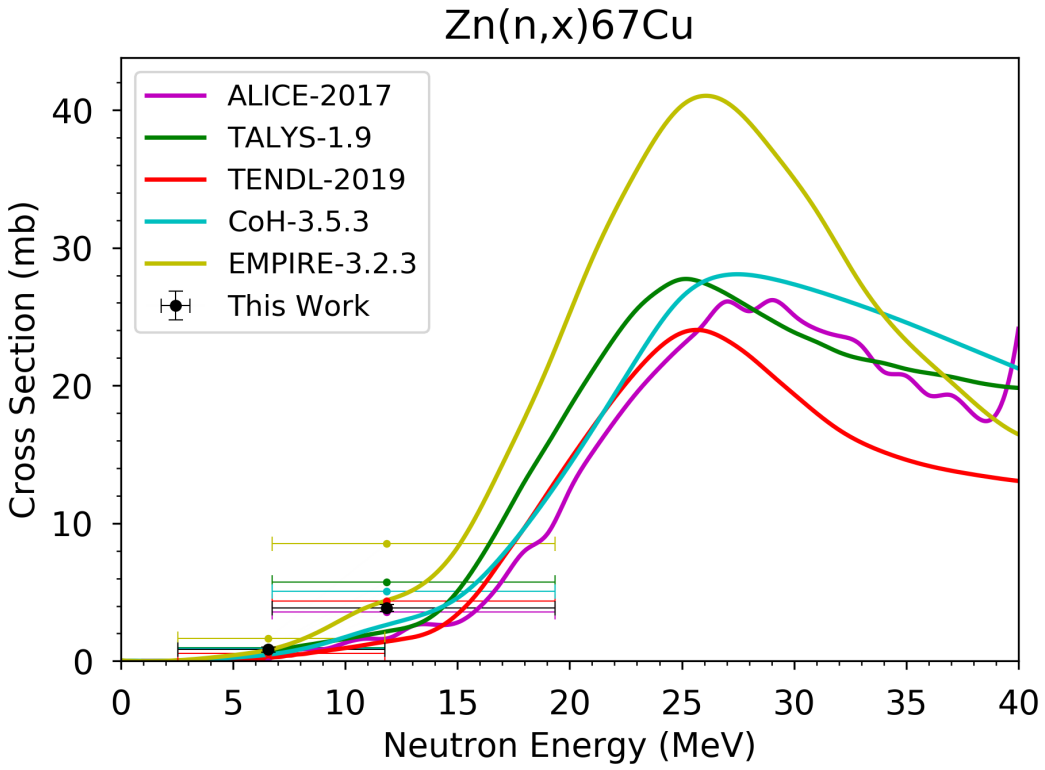

Figure 6.3: Cross section results for ^{67}Cu.

6.2.1 Discussion on ^{64,67}Cu production

The results on cross section for ^{64,67}Cu in this experiment show that the simultaneous production of these medical isotopes can be done via deuteron breakup. Since a higher enriched ^{67}Cu production require higher energies, this pathway can be used for simultaneous production and making it available with K = 35 cyclotrons.

This is a big step towards producing and using this new theranostic pair in both diagnostic and therapeutic applications. As seen in Figure 6.2b and Figure 6.3 the production of ^{64}Cu and ^{67}Cu depends on the beam energy being used, so by tuning the beam, the decision on what ratio the isotopes can be produced in can be controlled.

Thick-target integral yields

To calculate the production yields of ^{64}Cu and ^{64}Cu, in units of (mCi/µA/g/sr), (mCi/µAh), (MBq/µAh) and the neutron yields, Equation 5.18, Equation 5.19 and Equation 5.20 were used. Neutron yields and the production yields are listed in Table 6.1.

The production yield in mCi/µAh and MBq/µAh is much smaller compared to other reported production yields seen in chapter 3, section 3.3. Unlike in charge particle experiments where the entire beam is incident upon the target, in this experiment, using deuteron breakup, a small fraction of the deuterons will undergo breakup produce neutrons. The aim of the setup in this experiment was to make use of the forward-focused neutrons from the breakup reaction, and thus, a small fraction of the neutrons are going to hit the target. The fact that our numbers are relatively small compared to the charged particle yield is therefore to be expected. Assuming the same amount of neutron hitting the target as charged-particles, the production yield will increase and are far more competitive compared to the established (p, x) and (d, x) production pathways. By making the target wider, more neutrons can be catched. Since neutrons don't loose much energy going through the target, making the target thicker gives a higher probability of interaction with the target.

At both energies, ^{64}Cu and ^{67}Cu are co-produced in the target. And since the separation of these two isotopes is difficult, both will always be present. But, the ratio of the production yields (in mCi/µA/g/sr) shows that for 16 Mev, approximately 164 times more ^{64}Cu was produced than ^{67}Cu, and 17 times more ^{64}Cu than ^{67}Cu for 33 MeV. For mCi/µAh, the ratio of ^{64}Cu:^{67}Cu is 784:1 for 16 MeV and 85:1 for 33 MeV which reflects the different in half-life for the two isotopes. This means that if the aim is to produce more of ^{64}Cu for diagnostic applications, a lower energy such as 16 MeV is preferable. The higher deuteron energy gives a lesser ratio between ^{64}Cu and ^{67}Cu, so by tuning the beam energy gives the option to choose the ratio between the two isotopes. This is a useful quality for making isotopes for theranostic applications.

The ratio at end of beam (EoB) activities shows that the activity is 684 times higher for ^{64}Cu than it is for ^{67}Cu at 16 MeV. This indicates how much of the

Isotope	Deuteron Energy	Production yield	Units
^{64}Cu	16 MeV	0.61592	mCi/µA/g/sr
^{67}Cu	16 MeV	0.00374	mCi/µA/g/sr
^{64}Cu	33 MeV	2.27333	mCi/µA/g/sr
^{67}Cu	33 MeV	0.12744	mCi/µA/g/sr
^{64}Cu	16 MeV	0.00035	mCi/µAh
^{67}Cu	16 MeV	4.40392e-07	mCi/µAh
^{64}Cu	33 MeV	0.00128	mCi/µAh
^{67}Cu	33 MeV	1.51199e-05	mCi/µAh
^{64}Cu	16 MeV	22.78919	MBq/µAh
^{67}Cu	16 MeV	0.13854	MBq/µAh
^{64}Cu	33 MeV	84.11321	MBq/µAh
^{67}Cu	33 MeV	4.71557	MBq/µAh
		Neutron yields	
^{64}Cu	16 MeV	3.79657e-10	mCi/(neutrons/ (MeV·µ$C \cdot sr$)
^{67}Cu	16 MeV	2.30798e-12	mCi/(neutrons/ (MeV·µ$C \cdot sr$)
^{64}Cu	33 MeV	1.67790e-10	mCi/(neutrons/ (MeV·µ$C \cdot sr$)
^{67}Cu	33 MeV	9.40671e-12	mCi/(neutrons/ (MeV·µ$C \cdot sr$)

Table 6.1: Production yields for ^{64}Cu and ^{67}Cu.

^{64}Cu isotope that was made compared to ^{67}Cu. The ratio at end of beam accounts for the half life of each isotope to show how much that is produced per length of beam. At 33 MeV, the ratio of ^{64}Cu:^{67}Cu is approximately 82.

Purity

To be able to use these isotopes not only the cross section is needed, but radiopurity and specific activity (the activity per amount of atoms of a radionuclide) are two important factors during production.

Isotope	Energy	IP	%	RNP	%
^{64}Cu	16 MeV	0.99262	99.262	0.99847	99.847
^{67}Cu	16 MeV	0.00737	0.737	0.00152	0.152
^{64}Cu	33 MeV	0.94217	94.217	0.98755	98.755
^{67}Cu	33 MeV	0.05782	5.782	0.01244	1.244

Table 6.2: Isotopic purity (IP) and Radionuclidic purity (RNP) for ^{64}Cu and ^{67}Cu, calculated at 1 hour after EoB, and prior to any radiochemical separations.

^{64}Cu and ^{67}Cu were the only copper radionuclides produced from the zinc target. No other copper isotopes were observed, stable isotopes such as ^{63}Cu and ^{65}Cu will be present but cannot be detected with HPGe detector, therefore, RNP is the most accurate. With known ratio between the end of beam activities and production yields, the ratio between the purities of the two copper isotopes are good approximations. There was trace production of ^{66}Cu made from the zinc target as well, but since its half-life is approximately 5 minutes [64], it will decay and be gone by one hour after end of beam.

Looking at purity from the dose perspective, the Radionuclidic purity is the most important because of the activity of each isotope. The isotopic purity is useful for labelling chemistry because it serves as a proxy for concentration of the isotopes competing in the sample during labelling.

6.3 Discussion on the results of other produced isotopes

As mentioned in the introduction to this chapter, many other isotopes were produced in this experiment and many are first time measurements. This means that the results of the monitor reactions are heavily weighted, and as discussed, these results are in good agreement with the evaluated data. The current results are consistent with published and evaluated data (where they exist) which implies that, the first time measurements for these new products are trustworthy. The results and further discussion are given in Appendix E.

Chapter 7

Summary and outlook

> Perhaps the best test of a man's intelligence is his capacity for making a summary.
>
> — Lytton Strachey

This thesis is motivated by the desire to characterize a novel pathway for production of the ^{64,67}Cu using deuteron breakup. The experiment was performed at the Lawrence Berkeley National Laboratory's 88-Inch Cyclotron in August 2018 where the aim was to produce neutrons through a deuteron breakup process. A beryllium target was irradiate using deuteron beams of 16 MeV and 33 MeV with the aim to produce neutron flux. The neutron flux were used to irradiate a natural zinc target with the goal to produce the two medical isotopes through the $^{\text{nat}}\text{Zn}(n, x)^{64,67}\text{Cu}$ reactions. In addition to the zinc target, zirconium, indium, yttrium and aluminum targets were irradiated. Together with the zinc, 33 cross section measurements are reported and discussed in this thesis. The targets were irradiated for 7 hours and 57 minutes with approximately 247.7 nA average beam current of 16 MeV deuteron. For 33 MeV deuterons, the targets were irradiated for 2 hours, 1 minute and 20 seconds with an average beam current of approximately 354 nA. The difference in length of the irradiation time is based on the knowledge that the higher beam energy will open up more reaction channels. To activate the channels that we want without producing too much activity, the limited time for irradiation was necessary for the 33 MeV run. The neutron yield from deuteron breakup is approximately two to three times higher at 33 MeV than for 16 MeV which makes the shorter irradiation time preferable for 33 MeV deuterons.

From the measurements on ^{64,67}Cu, both 16 MeV and 33 MeV deuteron breakup produces more of ^{64}Cu than ^{67}Cu, but the ratio of ^{64}Cu:^{67}Cu decreases with higher deuteron energy. The data points from this experiment are in agreement with both modeling codes and previous measurements of ^{64}Cu, but there is no experimental data available for comparison with ^{67}Cu. For both the 16 MeV and 33 MeV deuteron beam, both ^{64}Cu and ^{67}Cu were produced, but the ratio of the production yield in mCi/µhA shows that it is possible to create approximately 164 times more ^{64}Cu than ^{67}Cu simply by tuning the beam to 16 MeV. For 33 MeV deuterons, the ^{64}Cu:^{67}Cu were 17:1. Dependent on how much ^{64}Cu and/or ^{67}Cu that is favourable to produce, the beam energy can be adjusted thereafter.

The cross section measurements were compared to the reaction modelling codes ALICE-2017, CoH-3.5.3, EMPIRE-3.2.3, TALYS-1.9 and TENDL-2019. While no code was overall the best in predictive power, ALICE, TALYS, CoH and TENDL are the codes that generally had the best agreement with the data measured in this experiment. EMPIRE was, perhaps, the modeling code that did not agreed very well.

^{64,67}Cu have been shown through previous research to be well suited for diagnostic and therapeutic applications in nuclear medicine. The challenge of producing ^{64,67}Cu isotopes is one of the motivations for finding a novel way of making them. The use of deuteron breakup as a way of producing neutrons is a new way of making neutron flux to irradiate natural zinc for production of ^{64,67}Cu. Since ^{64,67}Cu forms a theranostic pair, it is clear that deuteron breakup is a feasible production pathway for high specific activity radionuclides with great potential to benefit this relatively new and upcoming field in medicine.

To answer my questions in the introduction: Can we produce ^{64,67}Cu in a large enough quantity that they can be used in diagnostic and therapeutic applications? And if so, is the production route in this experiment a preferable way of doing this? By comparing production yield from previous experiment with the results in this thesis shows that it is possible to make ^{64,67}Cu in a large enough quantity for clinical use. By making the target bigger or thicker the production yield will increase; a thought for future experiments. This novel pathway of producing ^{64,67}Cu has shown in this experiment to be a promising production pathway and should be repeated. Further investigations on this way of making ^{64,67}Cu is important. As more experiments are performed, this gives more data which will be vital for production for clinical use. A second experiment that includes additional and higher deuteron energies, investigating how that would affect the production yield ratio of ^{64}Cu and ^{67}Cu would be interesting and important to document.

Appendix A

Calibration sources

^{137}Cs		^{133}Ba		^{152}Eu	
E_γ[keV]	I_γ[%]	E_γ[keV]	E_γ[%]	E_γ[keV]	E_γ[%]
661.66 (3)	85.10 (2)	53.16 (6)	2.14 (3)	121.7817 (3)	28.53 (16)
		79.61 (12)	2.56 (5)	244.6974 (8)	7.55 (4)
		80.99 (11)	32.9 (3)	295.9387 (17)	0.440 (4)
		160.61 (16)	0.64 (5)	329.41 (5)	0.1213 (24)
		223.24 (13)	0.45 (3)	344.2785 (12)	26.59 (20)
		276.40 (12)	7.16 (5)	367.7891 (20)	0.859 (6)
		302.85 (5)	18.34 (13)	411.1165 (12)	2.237 (13)
		356.01 (7)	62.05	416.02 (3)	0.1088 (19)
		383.85 (12)	8.94 (6)	443.9606 (16)	2.827 (14(
				444.01 (17)	0.298 (11)
				488.6792 (20)	0.414 (3)
				503.467 (9)	0.1524 (20)
				563.986 (5)	0.494 (5)
				566.438 (6)	0.131 (3)
				586.2648 (26)	0.455 (4)
				656.489 (5)	0.1441 (22)
				674.64 (14)	0.169(3)
				678.623 (5)	0.473 (4)
				688.670 (5)	0.856 (6)
				719.346 (7)	0.250 (8)
				764.88 (4)	0.189 (4)
				778.9045 (24)	12.93 (8)
				810.451 (5)	0.317 (3)
				841.574 (5)	0.168 (3)
				867.380 (3)	4.23 (3)
				919.337 (4)	0.419 (5)
				926.31 (5)	0.272 (3)
				963.367 (7)	0.140 (6)
				964.057 (5)	14.51 (7)
				1005.27 (5)	0.659 (11)
				1085.837 (10)	10.11 (5)
				1089.737 (5)	1.734 (11)
				1109.18 (5)	0.189 (6)
				1112.076 (3)	13.67 (8)
				1212.948 (11)	1.415 (8)
				1249.94 (5)	0.187 (3)
				1292.78 (5)	0.101 (3)
				1299.142 (8)	1.633 (11)
				1408.013 (3)	20.87 (9)
				1457.643 (11)	0.497 (4)
				1528.10 (4)	0.279 (3)

Table A.1: A list of all the energy lines of the calibration sources that were used in the calibration. [116–118]

Appendix B

Statistics and uncertainty

Standard deviation

When a sample is taken from a normal distribution, the uncertainty in statistics refers to the deviation of the data, σ. It is a measure of how the data points are scattered around the mean value:

$$\sigma = \sqrt{\frac{1}{N}\sum_{i}^{N}(x_i - \overline{x})^2} \tag{B.1}$$

$x_i = x_1, x_2, .., x_N$ are all the observed values in a sample, $\overline{x}$ is the mean value of the observed values and N is the number of observations in a sample.

The χ^2-propagation

In regression, the chi-square distribution is used for testing the goodness of fit. It is a test that tells how well theoretical distributions explain observed ones or how good a fit to observed results are for theoretical distributions [31] and is given as [137]:

$$\chi^2 = \sum_{i=1}^{n}\left(\frac{y_i - Y_i}{\sigma}\right)^2 \tag{B.2}$$

where y_i is the value of the sample taken, Y_i is the mean of the samples, and σ is the standard deviation of the samples.

Propagation of uncertainty

For a function f with inputs, x, a set of linear parameters, $a = a_1, a_2, a_3, ..., a_i$, and outputs, y, can be written as:

$$y = f(x, a) \tag{B.3}$$

The variance-covariance matrix of the input parameters of a_i is given as:

$$\mathbf{V} = \begin{pmatrix} \sigma_1^2 & \sigma_{1,2} & \cdots & \sigma_{1,n} \\ \sigma_{2,1} & \sigma_2^2 & \cdots & \sigma_{2,n} \\ \vdots & \vdots & \ddots & \vdots \\ \sigma_{n,1} & \sigma_{n,2} & \cdots & \sigma_n^2 \end{pmatrix} \tag{B.4}$$

and the Jacobian matrix of the measurements in function f is given as:

$$\left(\mathbf{J} = \frac{\partial f}{\partial a_1}, \frac{\partial f}{\partial a_2}, \cdots, \frac{\partial f}{\partial a_n}\right) \tag{B.5}$$

The most general expression for the error propagation is:

$$\sigma_y^2 = \mathbf{JVJ}^T \tag{B.6}$$

where σ_y^2 is the variance of y.

Weighted average

When measurements are correlated, the standard case of an uncertainty-weighted average no longer applies. Instead, a general case for the weighted average of correlated measurements is described here, in the context of calculating the average neutron flux.

The beam flux is given as:

$$\phi = \frac{R}{N_a \sigma} \tag{B.7}$$

where R is the production rate, N_a is the number of atoms in the target and σ is the flux-weighted average cross section.

The uncertainty in flux is given by:

$$\delta\phi = \sqrt{\left(\frac{\partial\phi}{\partial R}\right)^2 \delta_R^2 + \left(\frac{\partial\phi}{\partial N_a}\right)^2 \delta_{N_a}^2 + \left(\frac{\partial\phi}{\partial\sigma}\right)^2 \delta_\sigma^2} \tag{B.8}$$

This will give one flux and one corresponding uncertainty per monitor reaction channel.

The weighted average of a set of flux measurements is given as:

$$\langle\phi\rangle = \frac{\sum_{i,j} \phi_j (\hat{V}^{-1})_{i,j}}{\sum_{i,j} (\hat{V}^{-1})_{i,j}} \tag{B.9}$$

Taking the expectation value and calculating the uncertainty in the average flux:

$$\sigma^2_{\langle\phi\rangle} = \sum_{i,j} (\hat{V}^{-1})_{i,j} \tag{B.10}$$

To get both the weighted average flux and its propagated uncertainty, the covariance matrix has to be calculated. This is done in this thesis using the robust sandwich estimator [138]:

$$V_{i,j} = cov(\phi_i, \phi_j) = \sum_x \left.\frac{\partial\phi}{\partial x}\right|_i \delta_{x_i} corr_x(x_i, x_j) \delta_{x_j} \left.\frac{\partial\phi}{\partial x}\right|_j \tag{B.11}$$

where $V_{i,j}$ is the element of the covariance matrix between flux i and flux j, and is the sum over x, where $x_i \in \{R, N_a, \sigma\}$.

Setting up a correlation matrices of each of the monitor foils to get the elements, converting it to get the averages. In this work the production rate $R = 0.3$. Since the same Ge-detector is used, the activity is going to be linked and it is estimated to be 30% correlated. The mass of the targets has no impact on the mass of the flux. They are independent of each other, and thus, $N_a = 1$. The cross section is going to be partially correlated. Because we are using the same neutron energy spectrum for the two different reactions, $\sigma = 0.3$.

Appendix C

Tables of nuclear and reaction data

In these tables the produced nuclei together with their half-life, decay mode, gamma energy and the intensity of the gamma-ray are listed.

Product nucleus	Half-life	Decay mode	E_γ(keV)	I_γ(%)
^{62}Zn	9.193 (15) h	$\epsilon = 100\%$	40.85 (6)	25.5 (24)
			243.36 (6)	2.52 (23)
			246.95 (6)	1.90 (18)
			507.60 (10)	14.8 (14)
			548.35 (11)	15.3 (14)
			596.56 (13)	26.0 (20)
^{63}Zn	38.47 (5) m	$\epsilon = 100\%$	669.62 (5)	8.2 (3)
			962.06 (4)	6.5 (4)
^{64}Cu	12.701 (2) h	$\epsilon = 61.50\%$	1345.77 (6)	0.475 (11)
^{65}Ni	2.51719 (26) h	$\beta^- = 100\%$	366.27 (3)	4.81 (6)
			1115.53 (4)	15.43 (13)
			1481.84 (5)	23.59 (14)
^{66}Cu	5.120 (14) m	$\beta^- = 100\%$	1039.2 (2)	9.23 (9)
^{67}Cu	61.83 (12) h	$\beta^- = 100\%$	91.266 (5)	7.0 (10)
			93.311 (5)	16.10 (20)
			184.577 (10)	48.7 (3)
			300.219 (10)	0.797 (11)
			393.529 (10)	0.220 (8)
^{69m}Zn	13.756 (18) h	IT = 99.967 %	438.634 (18)	94.85 (7)

Table C.1: Decay data for zn(n, x) reaction products observed in this thesis. Uncertainties are listed in the least significant digit, that is, 78.4(12) hr means 78.4 ± 1.2 hr [30, 47, 63, 64, 139–141].

Product nucleus	Half-life	Decay mode	E_γ(KeV)	I_γ(%)
^{89}Zr	78.4 (12) h	$\epsilon = 100\%$	909.15 (15)	99.04 (3)
			1620.8 (2)	0.073 (5)
			1713.0 (6)	0.745 (13)
			1744.5 (2)	0.123 (4)
^{90m}Y	3.19 (6) h	IT = 100%	202.53 (3)	97.3 (4)
			479.51 (5)	90.74 (5)
			681.8 (6)	0.32 (3)
^{91m}Y	49.71 (4) m	IT = 100%	555.57 (5)	95.0 (3)
^{92}Y	3.54 (1) h	$\beta^- = 100\%$	488.5 (1)	2.3 (3)
			561.1 (1)	2.4 (3)
			844.3 (1)	1.25 (14)
			934.47 (7)	13.9 (15)
			1405.4 (1)	4.8 (5)
^{93}Y	10.18 (8) h	$\beta^- = 100\%$	266.9 (1)	7.4 (11)
			947.1 (1)	2.1 (3)
^{95}Zr	64.032 (6) d	$\beta^- = 100\%$	724.192 (4)	44.27 (22)
			756.725 (12)	54.38(22)
^{95}Nb	34.991 (6) d	$\beta^- = 100\%$	765.803 (6)	99.808 (7)
^{97}Nb	72.1 (7) m	$\beta^- = 100\%$	657.94 (9)	98.23 (8)
^{97}Zr	16.749 (8) h	$\beta^- = 100\%$	743.36 (3)	93.09 (16)

Table C.2: Decay data for zr(n, x) reaction products observed in this thesis. Uncertainties are listed in the least significant digit, that is, 78.4(12) hr means 78.4 $\pm$ 1.2 hr [142–148].

Product nucleus	Half-life	Decay mode	E_γ(KeV)	I_γ(%)
^{87m}Y	13.37 (3) h	IT = 98.43%	380.79 (7)	78.05 (7.9)
^{87}Y	79.8 (3)h	$\epsilon = 100\%$	484.805 (5)	89.8 (9)
^{88}Y	106.627 (21) d	$\epsilon = 100\%$	898.042 (3)	93.7 (3)
			1836.063 (12)	99.2 (3)
			2734.0 (5)	0.71 (7)
^{90m}Y	3.19 (6) h	IT = 100%	202.53 (3)	97.3 (4)
			479.51 (5)	90.74 (5)

Table C.3: Decay data for y(n, x) reaction products observed in this thesis. Uncertainties are listed in the least significant digit, that is, 78.4(12) hr means 78.4 $\pm$ 1.2 hr [129, 143, 149].

Product nucleus	Half-life	Decay mode	E_γ(KeV)	I_γ(%)
^{111}In	2.8047 (4) d	$\epsilon = 100\%$	171.28 (3)	90.7 (9)
			245.35 (4)	94.1 (10)
^{112m}In	20.67 (8) m	IT = 100 %	156.61(3)	13.33 (16)
^{112}In	14.88 (17) m	$\epsilon = 62(4)\%$	617.517 (3)	6.7 (25)
^{113m}In	99.476 m	IT = 100 %	391.698 (3)	64.97 (14)
^{114m}In	49.51 (1) d	$\epsilon = 3.25(24)\%$	558.43 (3)	4.4 (6)
			725.24 (3)	4.4 (6)
^{115m}In	4.486 (4) h	IT = 95.0 (7) %	336.241 (25)	45.9 (1)
^{116m}In	54.29(17) m	$\beta^- = 100\%$	138.29 (2)	3.70 (9)
			263.03 (3)	0.126 (4)
			278.62 (2)	0.130 (4)
			303.73 (4)	0.120 (6)
			355.40 (2)	0.730 (11)
			416.90 (2)	27.2 (4)
			463.21 (2)	0.725 (11)
			655.17 (2)	0.123 (3)
			688.93 (2)	0.166 (4)
			705.97 (2)	0.160 (3)
			779.12 (22)	0.247 (5)
			818.68 (2)	12.13 (14)
			972.60 (2)	0.496 (7)
			1097.28 (2)	58.5 (8)
			1293.56 (2)	84.8 (12)
			1507.59 (2)	9.92 (13)
			1752.50 (2)	2.36(3)
			2112.29 (2)	15.09 (22)

Table C.4: Decay data for in(n, x) reaction products observed in this thesis. Uncertainties are listed in the least significant digit, that is, 78.4(12) hr means 78.4 $\pm$ 1.2 hr [150–155].

Product nucleus	Half-life	Decay mode	E_γ(KeV)	I_γ(%)
^{24}Na	14.997 (12) h	$\beta^- = 100\%$	1368.626 (5)	99.9936 (15)
			2754.007 (11)	99.855 (5)

Table C.5: Decay data for al

$$(n, x)$$

$reactionproductsobservedinthisthesis.Uncertaintiesarelistedintheleastsignificantdigit, thatis, 78.4$
1.2 hr [156]

Appendix D

Tabulated neutron spectra data

The improved data on the 33 MeV neutron spectrum by Morrell [132]. The data in this table was used to find the spectrum-average cross sections in this thesis.

Energy (MeV)	Flux (arb. unit)	Energy (MeV)	Flux (arb. unit)
0.1	4338181616.67	16.8	11123753944.9
0.2	5559195990.52	16.9	10970131827.4
0.3	6388576222.98	17.0	10812953323.2
0.4	7004204269.99	17.1	10652456057.8
0.5	7478815255.26	17.2	10488888734.3
0.6	7851674167.8	17.3	10322509917.5
0.7	8147264709.78	17.4	10153586709.8
0.8	8382277733.45	17.5	9982393337.25
0.9	8568798710.17	17.6	9809209658.74
1.0	8715962614.04	17.7	9634319618.34
1.1	8830895876.38	17.8	9458009659.23
1.2	8919290698.74	17.9	9280567119.39
1.3	8985774362.88	18.0	9102278629.52
1.4	9034157039.5	18.1	8923428533.44
1.5	9067604070.19	18.2	8744297350.77
1.6	9088759584.14	18.3	8565160300.66
1.7	9099837983.3	18.4	8386285903.82
1.8	9102693943.52	18.5	8207934678.55
1.9	9098878029.61	18.6	8030357944.09
2.0	9089682730.59	18.7	7853796742.65
2.1	9076182115.9	18.8	7678480888.72

Energy (MeV)	Flux (arb. unit)	Energy (MeV)	Flux (arb. unit)
2.2	9059267100.67	18.9	7504628151.92
2.3	9039677357.1	19.0	7332443577.09
2.4	9018030188.03	19.1	7162118942.7
2.5	8994846202.69	19.2	6993832356.59
2.6	8970571420.24	19.3	6827747985.64
2.7	8945595458.67	19.4	6664015914.15
2.8	8920265683.09	19.5	6502772124.12
2.9	8894897491.63	19.6	6344138589.09
3.0	8869781206.14	19.7	6188223472.14
3.1	8845186231.73	19.8	6035121417.93
3.2	8821363221.4	19.9	5884913928.1
3.3	8798544940.81	20.0	5737669808.88
3.4	8776946411.25	20.1	5593445680.11
3.5	8756764760.04	20.2	5452286534.69
3.6	8738179061.9	20.3	5314226338.17
3.7	8721350332.85	20.4	5179288658.28
3.8	8706421747.5	20.5	5047487315.48
3.9	8693519089.83	20.6	4918827045.57
4.0	8682751411.93	20.7	4793304166.85
4.1	8674211857.89	20.8	4670907244.83
4.2	8667978604.84	20.9	4551617748.23
4.3	8664115876.09	21.0	4435410691.24
4.4	8662674986.91	21.1	4322255257.25
4.5	8663695391.44	21.2	4212115400.71
4.6	8667205706.66	21.3	4104950423.81
4.7	8673224696.13	21.4	4000715525.89
4.8	8681762201.84	21.5	3899362323.79
4.9	8692820017.21	21.6	3800839342.06
5.0	8706392697.73	21.7	3705092472.28
5.1	8722468308.25	21.8	3612065401.42
5.2	8741029107.95	21.9	3521700009.25
5.3	8762052175.02	22.0	3433936735.27
5.4	8785509974.25	22.1	3348714916.01
5.5	8811370870.89	22.2	3265973093.5
5.6	8839599594.41	22.3	3185649296.01
5.7	8870157656.15	22.4	3107681292.4
5.8	8903003724.23	22.5	3032006821.32
5.9	8938093959.61	22.6	2958563796.62
6.0	8975382316.32	22.7	2887290490.48

Energy (MeV)	Flux (arb. unit)	Energy (MeV)	Flux (arb. unit)
6.1	9014820809.3	22.8	2818125695.63
6.2	9056359752.51	22.9	2751008868.09
6.3	9099947970.13	23.0	2685880251.91
6.4	9145532983.26	23.1	2622680987.15
6.5	9193061174.4	23.2	2561353202.59
6.6	9242477931.6	23.3	2501840094.3
6.7	9293727774.39	23.4	2444085991.4
6.8	9346754462.85	23.5	2388036410.14
6.9	9401501091.62	23.6	2333638097.31
7.0	9457910170.07	23.7	2280839064.09
7.1	9515923689.91	23.8	2229588611.38
7.2	9575483181.32	23.9	2179837347.27
7.3	9636529758.75	24.0	2131537197.68
7.4	9699004157.14	24.1	2084641410.91
7.5	9762846759.52	24.2	2039104556.72
7.6	9827997616.65	24.3	1994882520.66
7.7	9894396459.49	24.4	1951932494.24
7.8	9961982704.97	24.5	1910212961.47
7.9	10030695455.8	24.6	1869683682.27
8.0	10100473494.6	24.7	1830305673.17
8.1	10171255273.1	24.8	1792041185.81
8.2	10242978896.6	24.9	1754853683.42
8.3	10315582104.1	25.0	1718707815.85
8.4	10389002244.7	25.1	1683569393.2
8.5	10463176249.7	25.2	1649405358.53
8.6	10538040602.8	25.3	1616183759.74
8.7	10613531305.5	25.4	1583873720.88
8.8	10689583841.1	25.5	1552445413.12
8.9	10766133135.6	25.6	1521870025.44
9.0	10843113515.8	25.7	1492119735.34
9.1	10920458666.6	25.8	1463167679.48
9.2	10998101584.6	25.9	1434987924.58
9.3	11075974531.6	26.0	1407555438.53
9.4	11154008985.4	26.1	1380846061.91
9.5	11232135589.9	26.2	1354836479.78
9.6	11310284103.7	26.3	1329504194.1
9.7	11388383348.0	26.4	1304827496.55
9.8	11466361153.2	26.5	1280785441.95
9.9	11544144305.2	26.6	1257357822.29

Energy (MeV)	Flux (arb. unit)	Energy (MeV)	Flux (arb. unit)
10.0	11621658491.5	26.7	1234525141.38
10.1	11698828246.6	26.8	1212268590.06
10.2	11775576898.0	26.9	1190570022.15
10.3	11851826511.9	27.0	1169411931.07
10.4	11927497839.8	27.1	1148777427.01
10.5	12002510265.7	27.2	1128650214.95
10.6	12076781754.8	27.3	1109014573.18
10.7	12150228803.0	27.4	1089855332.58
10.8	12222766388.9	27.5	1071157856.57
10.9	12294307927.3	27.6	1052908021.64
11.0	12364765225.8	27.7	1035092198.64
11.1	12434048444.6	27.8	1017697234.54
11.2	12502066059.1	27.9	1000710434.98
11.3	12568724827.4	28.0	984119547.342
11.4	12633929762.1	28.1	967912744.382
11.5	12697584107.9	28.2	952078608.532
11.6	12759589324.4	28.3	936606116.705
11.7	12819845076.8	28.4	921484625.667
11.8	12878249233.2	28.5	906703857.939
11.9	12934697871.2	28.6	892253888.224
12.0	12989085293.6	28.7	878125130.328
12.1	13041304054.3	28.8	864308324.575
12.2	13091244996.2	28.9	850794525.69
12.3	13138797301.7	29.0	837575091.138
12.4	13183848556.4	29.1	824641669.902
12.5	13226284828.7	29.2	811986191.689
12.6	13265990765.8	29.3	799600856.548
12.7	13302849707.0	29.4	787478124.878
12.8	13336743816.8	29.5	775610707.828
12.9	13367554238.4	29.6	763991558.054
13.0	13395161269.8	29.7	752613860.84
13.1	13419444563.7	29.8	741471025.559
13.2	13440283352.2	29.9	730556677.457
13.3	13457556698.9	30.0	719864649.762
13.4	13471143779.3	30.1	709388976.095
13.5	13480924190.3	30.2	699123883.171
13.6	13486778291.6	30.3	689063783.785
13.7	13488587578.6	30.4	679203270.068
13.8	13486235088.6	30.5	669537107.008

Energy (MeV)	Flux (arb. unit)	Energy (MeV)	Flux (arb. unit)
13.9	13479605841.0	30.6	660060226.21
14.0	13468587312.3	30.7	650767719.913
14.1	13453069945.1	30.8	641654835.221
14.2	13432947692.3	30.9	632716968.571
14.3	13408118594.5	31.0	623949660.406
14.4	13378485390.7	31.1	615348590.051
14.5	13343956160.2	31.2	606909570.797
14.6	13304444992.8	31.3	598628545.161
14.7	13259872685.9	31.4	590501580.334
14.8	13210167463.0	31.5	582524863.807
14.9	13155265711.2	31.6	574694699.153
15.0	13095112730.3	31.7	567007501.982
15.1	13029663489.6	31.8	559459796.042
15.2	12958883383.8	31.9	552048209.472
15.3	12882748981.2	32.0	544769471.196
15.4	12801248755.8	32.1	537620407.453
15.5	12714383792.7	32.2	530597938.458
15.6	12622168458.6	32.3	523699075.193
15.7	12524631025.8	32.4	516920916.309
15.8	12421814238.4	32.5	510260645.157
15.9	12313775810.9	32.6	503715526.919
16.0	12200588845.8	32.7	497282905.853
16.1	12082342161.3	32.8	490960202.634
16.2	11959140516.6	32.9	484744911.805
16.3	11831104725.6	33.0	478634599.31
16.4	11698371649.3	33.1	472626900.123
16.5	11561094060.5	33.2	466719515.97
16.6	11419440372.2	33.3	460910213.123
16.7	11273594227.1	33.4	455196820.288

Appendix E

Cross sections

In this thesis, many other cross sections were also measured and the results are discussed below. In the tables Table E.1, Table E.2,Table E.3,Table E.4 we report cumulative (c) and independent (i) cross sections. Cumulative nuclei are affected by decay feeding, for example feeding from an excited state to the ground state. It can also be a first observed element in a decay chain, if a precursor isotope with too short of a half-life to be measured decays. If there was no feeding, the cross section is reported as independent.

E.1 Other interesting cross section results

Neutron-induced reactions on zinc

Figure E.1 shows all the products created using the natural zinc target with the abundance 49.17% of ^{64}Zn, 27.73% of ^{66}Zn, 4.04% of ^{67}Zn, 18.45% of ^{68}Zn, and 0.61% of ^{70}Zn.

The products produced along with its half-life, decay mode, gamma energy and the intensity of each gamma is listed in Table C.1.

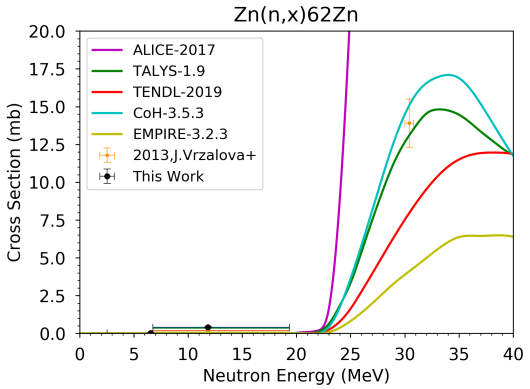

(a) Cross section for $^{\text{nat}}\text{Zn}(n,x)^{62}\text{Zn}$

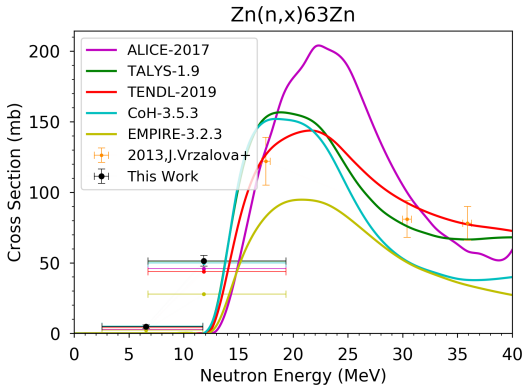

(b) Cross section for $^{\text{nat}}\text{Zn}(n,x)^{63}\text{Zn}$

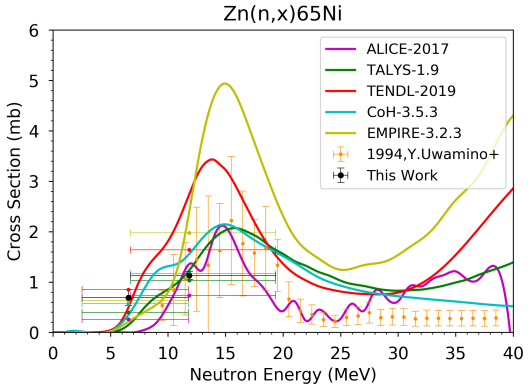

(c) Cross section for $^{\text{nat}}\text{Zn}(n,x)^{65}\text{Ni}$

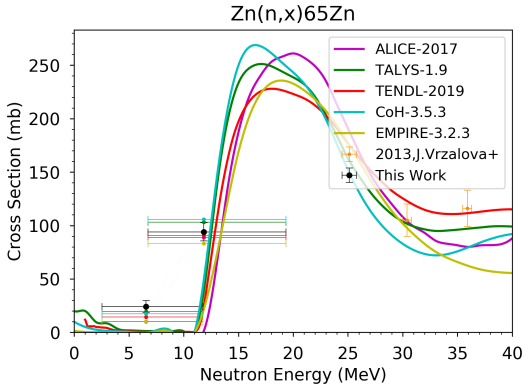

(d) Cross section for $^{\text{nat}}\text{Zn}(n,x)^{65}\text{Zn}$

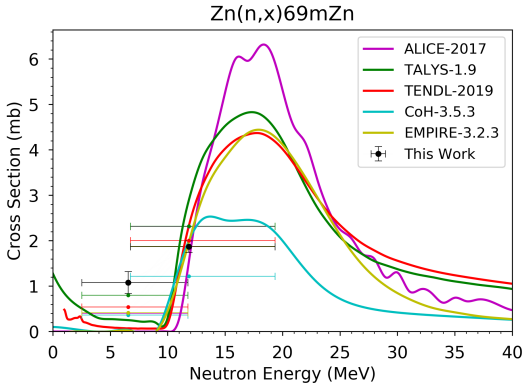

(e) Cross section for $^{\text{nat}}\text{Zn}(n,x)^{69m}\text{Zn}$

Figure E.1: Cross section measurements for products following n-induced reactions on natural zinc target together with modeling codes and other experimental data [135].

Production cross sections (mb)		
E_n (MeV)	$6.55^{+4.02}_{-5.09}$	$11.84^{+5.21}_{-7.51}$
$^{62}Zn_i$	0.03 ± 0.02	0.40 ± 0.04
$^{63}Zn_i$	4.76 ± 1.15	51.41 ± 3.73
$^{64}Cu_i$	138.98 ± 31.55	68.61 ± 5.17
$^{65}Ni_i$	0.69 ± 0.16	1.13 ± 0.08
$^{65}Zn_i$	24.24 ± 5.55	94.02 ± 8.54
$^{67}Cu_i$	0.84 ± 0.19	3.86 ± 0.26
$^{69m}Zn_i$	1.08 ± 0.24	1.87 ± 0.13

Table E.1: The measured cross sections for $^{nat}Zn(n,x)$ reactions. Subscript i indicates that the measurement is independent while subscript c indicates that the measurement is cumulative.

^{nat}Zn$(n,x)^{62}$Zn

The measured spectrum-average cross section for ^{62}Zn shows good agreement with the modeling codes shown in Figure E.1a. To be able to produce ^{62}Zn from natural zinc, a ^{64}Zn(n,3n) reaction is required, and thus, more energy. In this experiment, two data points were obtained where the cross section for 6 MeV neuton energy is of a low magnitude and thus, is not visible in Figure E.1a. After approximately 23 MeV, the modeling codes scatters and only a single datapoint by J.Vrzalová et al. [157] with around 30 MeV has been measured.

^{nat}Zn$(n,x)^{63}$Zn

The measured spectrum-averaged cross section for ^{63}Zn (Figure E.1b) shows good agreement especially with TALYS and CoH. For 6 MeV, the modeling codes are in better agreement than for 12 MeV. EMPIRE has overall a lower cross section prediction than the rest of the modeling codes. There are no other data points in the 6-12 MeV region, but J. Vrzalová et al. [157] has reported some data points from approximately 17-37 MeV.

^{nat}Zn$(n,x)^{65}$Ni

The measured spectrum-average cross section for ^{65}Ni is shown in Figure E.1c and Table E.1. Even though the modeling codes are a bit scattered, ALICE, TALYS and CoH show the best agreement. Looking at my data point at 6 MeV, EMPIRE

is the best fit, but at 12 MeV EMPIRE overestimate the peak. Our data points is agrees with the mentioned modeling codes and the datapoints from Y. UWAMINO et al.

$^{\mathbf{nat}}\mathbf{Zn}(n,x)^{\mathbf{65}}\mathbf{Zn}$

The measured spectrum-average cross section for ^{65}Zn is shown in Figure E.1d and Table E.1. There are no measured data points near 6 MeV and 12 MeV, there are however, data points by Y. UWAMINO et al,. [136] above 30 MeV. At 6 MeV, my data point is almost 5 mb higher than the modeling codes. The closest modeling code is TALYS and is within the cross section errorbar for my datapoint. At 12 MeV, both TENDL and ALICE are in good agreement with my datapoint.

$^{\mathbf{nat}}\mathbf{Zn}(n,x)^{\mathbf{69}m}\mathbf{Zn}$

The measured spectrum-average cross section for ^{69m}Zn are shown in Figure E.1e and Table E.1. Since there is no other measured data points for ^{69m}Zn, the modeling codes are our only tool to measure how physically reasonable good of a measurements this is. The modeling codes do scatter a bit, but for 6 MeV, TALYS is the best fit, while EMPIRE and TENDL show good agreement with my data point at 16 MeV. Looking at the spectrum for the modeling codes, the three mention codes are in good agreement with each other. CoH and ALICE gives very different estimates for what the cross section should look like for 10-25 MeV. Without measurements it is hard to know which one of the modelling codes that is correct.

Neutron-induced reactions on zirconium

Figure E.2 shows all the products created through natural zirconium with the abundance 51.45% of ^{90}Zr, 11.22% of ^{91}Zr, 17.15% of ^{92}Zn, 17.38% of ^{94}Zr, and 2.80% of ^{96}Zr.

The products produced along with its half-life, decay mode, gamma energy and the intensity of each gamma is listed in Table C.2.

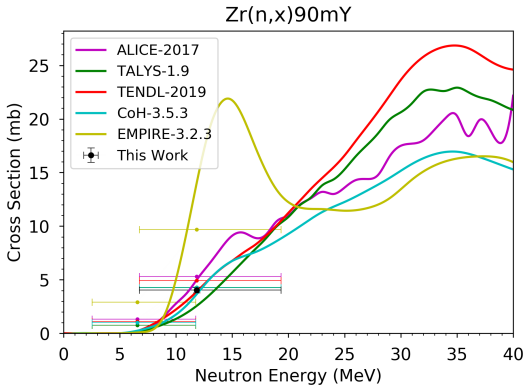

(a) Cross section for $^{\text{nat}}\text{Zr}(n,x)^{90m}\text{Y}$

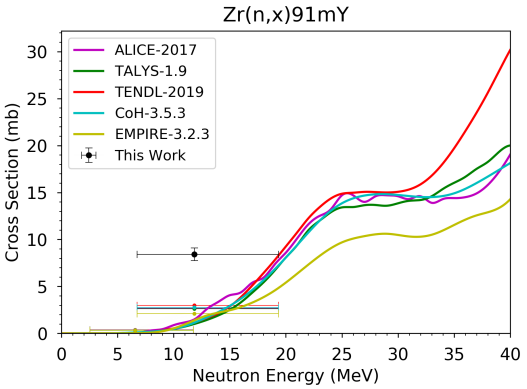

(b) Cross section for $^{\text{nat}}\text{Zr}(n,x)^{91m}\text{Y}$

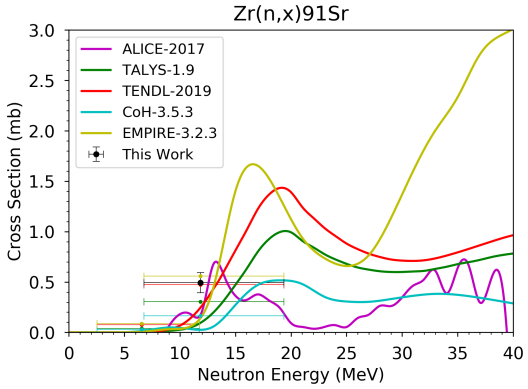

(c) Cross section for $^{\text{nat}}\text{Zr}(n,x)^{91}\text{Sr}$

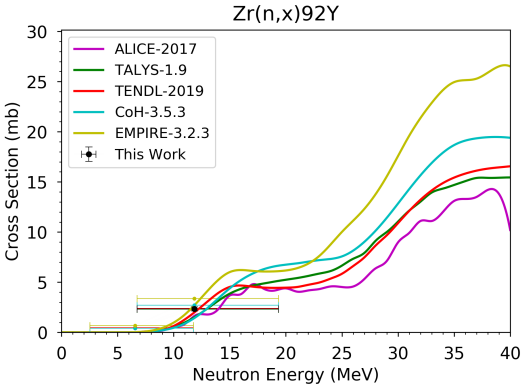

(d) Cross section for $^{\text{nat}}\text{Zr}(n,x)^{92}\text{Y}$

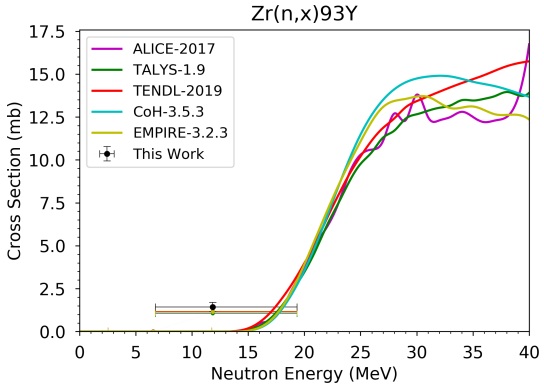

(e) Cross section for $^{\text{nat}}\text{Zr}(n,x)^{93}\text{Y}$

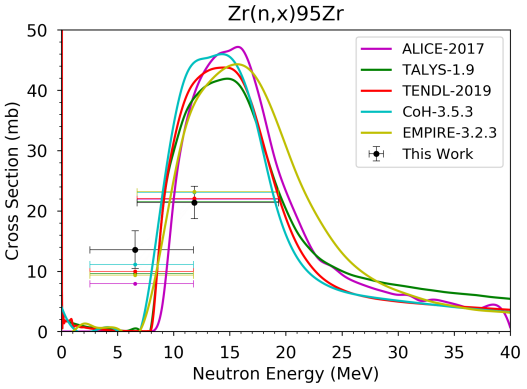

(f) Cross section for $^{\text{nat}}\text{Zr}(n,x)^{95}\text{Zr}$

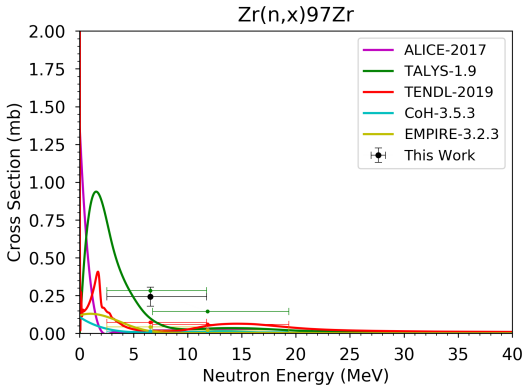

(g) Cross section for $^{\text{nat}}\text{Zr}(n,x)^{97}\text{Zr}$

Figure E.2: Cross section measurements for products following n-induced reactions on natural zirconium target together with modeling codes and other experimental data [135].

Production cross sections (mb)		
E_n (MeV)	$6.55^{+4.02}_{-5.09}$	$11.84^{+5.21}_{-7.51}$
$^{90m}Y_i$		4.04 ± 0.28
$^{91m}Y_i$		8.42 ± 0.66
$^{91}Sr_i$		0.49 ± 0.10
$^{92}Y_i$		2.33 ± 0.20
$^{93}Y_i$		1.43 ± 0.26
$^{95}Zr_i$	13.56 ± 3.12	21.39 ± 2.70
$^{97}Zr_i$	0.24 ± 0.06	
	Monitor reactions	
$^{89}Zr_i$	28.09 ± 8.98	219.76 ± 14.90

Table E.2: The measured cross sections for $^{\text{nat}}\text{Zr}(n,x)$ reactions. Subscript i indicates that the measurement is independent while subscript c indicates that the measurement is cumulative.

$^{\text{nat}}\mathbf{Zr}(n,x)^{\mathbf{90m}}\mathbf{Y}$

The measured spectrum-average cross section for ^{90m}Y is shown in Figure E.2a

and Table E.2, gives only one datapoint at 12 MeV. With no other datapoints to compare this result with, CoH is the modeling code with best agreement to this work. EMPIRE and ALLICE predict a bump near 12 MeV, but this is not seen in our data. This is a first-time measurement, and therefore, more data is needed.

$^{\mathbf{nat}}\mathbf{Zr}(n,x)^{\mathbf{91}m}\mathbf{Y}$

The measured spectrum-average cross section for ^{91m}Y is shown in Figure E.2b and Table E.2. The datapoint in this work is higher than the modeling codes and is therefore not in good agreement. More experimental points are therefore needed to see if the modeling codes are correct for this reaction.

$^{\mathbf{nat}}\mathbf{Zr}(n,x)^{\mathbf{91}}\mathbf{Sr}$

The first-time measured spectrum-average cross section for ^{91}Sris shown in Figure E.2c and Table E.2. The datapoint in this work is in best agreement with EMPIRE and TENDL. It would be interesting to see which modeling codes fit the best if more experimental datapoints for this reaction were collected, as each code provides a very distinct excitation function not seen in any of the others. The modeling codes scatter and do not behave the same way for higher energies.

$^{\mathbf{nat}}\mathbf{Zr}(n,x)^{\mathbf{92}}\mathbf{Y}$

The first-time measured spectrum-average cross section for ^{92}Y is shown in Figure E.2d and listed in Table E.2. This data point agrees well with all of the modeling code, which are all in agreement for the shape of the excitation function with each other, showing small differences in magnitude except EMPIRE, which is a bit higher in magnitude compared to the rest.

$^{\mathbf{nat}}\mathbf{Zr}(n,x)^{\mathbf{93}}\mathbf{Y}$

The first-time measured spectrum-average cross section for ^{93}Y is shown in Figure E.2e and listed in Table E.2. This data point looks to agree well with the modeling codes where all of the codes are in agreement with each other. They follow the same shape of the excitation function. The measured cross section in this work is a bit higher in magnitude, but not much. TENDL is within the errorbar for our data point and is the best fit. The modeling codes do agree with each other when looking at cross sections at higher energies.

$^{\mathbf{nat}}\mathbf{Zr}(n,x)^{\mathbf{95}}\mathbf{Zr}$

The first-time measured spectrum-average cross section for ^{95}Zr is shown in Figure E.2f and listed in Table E.2. The data points in this work show overall a

good agreement with the modeling codes. The 6 MeV point is a bit higher than the modeling codes but CoH is within the data point errorbar. All the modeling codes is also in agreement for the shape of the excitation function with each other, showing small differences in magnitude.

$^{\mathbf{nat}}$Zr$(n, x)^{\mathbf{97}}$Zr

The first-time measured spectrum-average cross section for ^{97}Zr, shown in Figure E.2g and listed in Table E.2. The only data point from this experiment at 6 MeV is in best agreement with TALYS. The data point is small in value and the modeling codes are pretty similar in their predictions. The modelling codes behaviour at low energies is dominated by thermal capture.

Indium

Figure E.3 shows all the products created using a natural indium target with the abundance 4.29% of ^{113}In, 95.71% of ^{115}In.

The products produced along with its half-life, decay mode, gamma energy and the intensity of each gamma is listed in Table C.4.

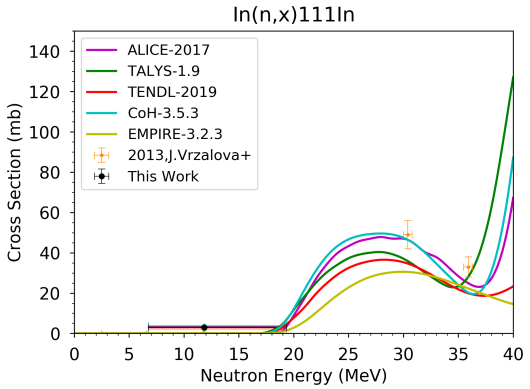

(a) Cross section for $^{\text{nat}}\text{In}(n,x)^{111}\text{In}$

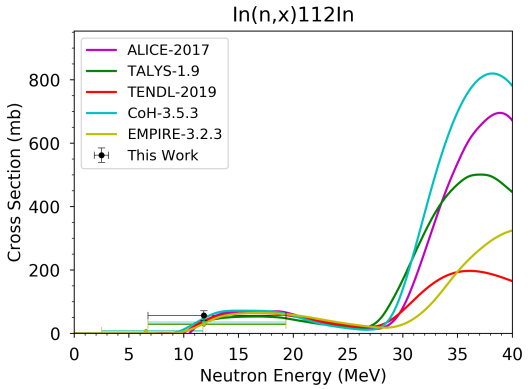

(b) Cross section for $^{\text{nat}}\text{In}(n,x)^{112}\text{In}$

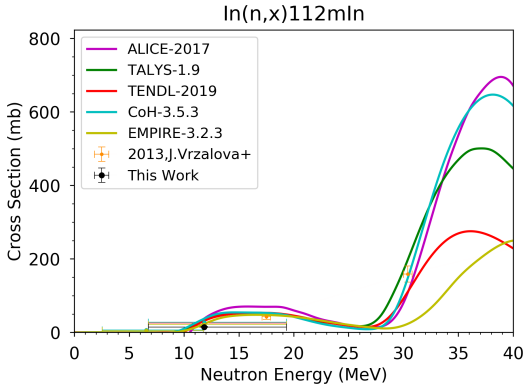

(c) Cross section for $^{\text{nat}}\text{In}(n,x)^{112m}\text{In}$

Figure E.3: Cross section measurements for products following n-induced reactions on natural indium target together with modeling codes and other experimental data [135].

Production cross sections (mb)		
E_n (MeV)	$6.55^{+4.02}_{-5.09}$	$11.84^{+5.21}_{-7.51}$
$^{111}\text{In}_i$		2.87 ± 0.22
$^{112m+g}\text{In}_c$		56.56 ± 14.84
$^{112m}\text{In}_i$		14.61 ± 1.15

Table E.3: The measured cross sections for $^{\text{nat}}\text{In}(n,x)$ reactions. Subscript i indicates that the measurement is independent while subscript c indicates that the measurement is cumulative.

$^{\mathbf{nat}}\mathbf{In}(n,x)^{\mathbf{111}}\mathbf{In}$

^{111}In is a product made in this experiment that also is used in diagnostic application. The spectrum-average cross section in Figure E.3a shows an agreement with the simulations on the production of this medical isotope for the 16 MeV deuteron beam. Some examples on how ^{111}In can be used are as a diagnostic tool for brain studies [158], bone marrow imaging [159] or it can be used to investigate inflammation and infections by imaging white blood cells [160]. More data on the production of this isotope is therefore needed. There are some data points at higher energies by J. Vrzalová et al. [157], but it would be interesting to compare more experimental data points.

$^{\mathbf{nat}}\mathbf{In}(n,x)^{\mathbf{112}}\mathbf{In}$

The first-time measured spectrum-average cross section for ^{112}In is shown in Figure E.3b and listed in Table E.3. The datapoint in this experiment agrees well with the modeling codes and the modeling codes are also in agreement until energies around 30 MeV, where they start to scatter due to the competition between ^{112m}In and ^{112}In.

$^{\mathbf{nat}}\mathbf{In}(n,x)^{\mathbf{112}m}\mathbf{In}$

The measured spectrum-average cross section for ^{112m}In is shown in Figure E.3c and listed in Table E.3. The datapoint from this work is a bit lower in magnitude compared to the modeling codes. It is closest to EMPIRE, but a couple of mb off. An experiment done in 2013 by J. Vrzalová et al. [157] shows a data point at 17 MeV that has best agreement with EMPIRE and another data point at 30 MeV. All of the modelling codes agrees with out data, but EMPIRE is the closest agreement.

Yttrium

Figure E.4 shows all the products created using a natural yttrium target with the abundance 100% of ^{89}Y.

The products produced along with its half-life, decay mode, gamma energy and the intensity of each gamma is listed in Table C.3.

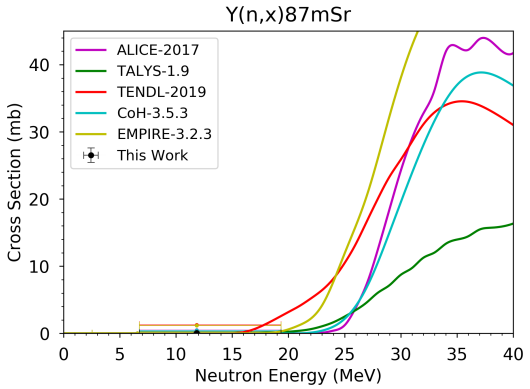

(a) Cross section for $^{\text{nat}}\text{Y}(n,x)^{87m}\text{Sr}$

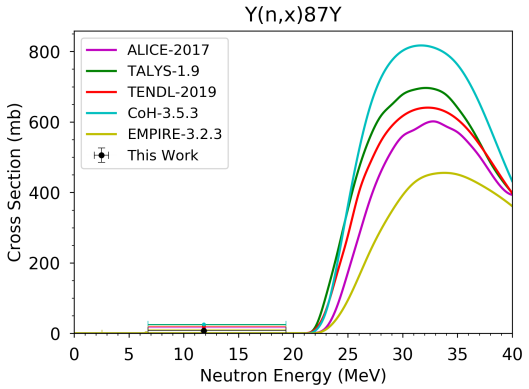

(b) Cross section for $^{\text{nat}}\text{Y}(n,x)^{87}\text{Y}$

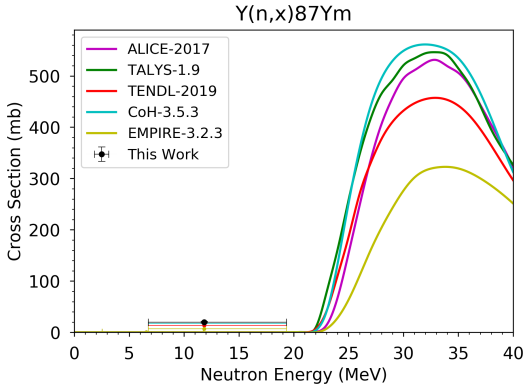

(c) Cross section for $^{\text{nat}}\text{Y}(n,x)^{87m}\text{Y}$

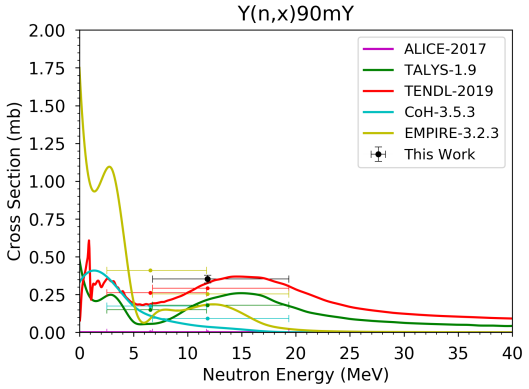

(d) Cross section for $^{\text{nat}}\text{Y}(n,x)^{90m}\text{Y}$

Figure E.4: Cross section measurements for products following n-induced reactions on natural yttrium target together with modeling codes and other experimental data [135].

Production cross sections (mb)		
E_n (MeV)	$6.55^{+4.02}_{-5.09}$	$11.84^{+5.21}_{-7.51}$
$^{87m}Sr_i$		0.07 ± 0.01
$^{87m+g}Y_c$		7.31 ± 0.61
$^{87m}Y_i$		19.99 ± 1.67
$^{90m}Y_i$		0.35 ± 0.03
	Monitor reactions	
$^{88}Y_i$	57.89 ± 12.90	506.32 ± 34.14

Table E.4: The measured cross sections for $^{nat}Y(n,x)$ reactions. Subscript i indicates that the measurement is independent while subscript c indicates that the measurement is cumulative.

$^{nat}Y(n,x)^{87m}Sr$

The first-time measured spectrum-average cross section for ^{87m}Sr is shown in Figure E.4a and listed in Table E.4 , which is in relatively good agreement with the modeling codes. At higher energies there is a scattering in the modeling odes. The cross section itself is quite low, and as the modeling code estimates, the cross section gets bigger with higher energies.

$^{nat}Y(n,x)^{87}Y$

The first-time measured spectrum-average cross section for ^{87}Y is shown in Figure E.4b and listed in Table E.4. EMPIRE is the modeling code closest to the data point in this work and they follow the same shape of the excitation function. The modeling codes are in an agreement until energies over 20 MeV where they start to scatter.

$^{nat}Y(n,x)^{87m}Y$

The first-time measured spectrum-average cross section for ^{87m}Y is shown in **??** and listed in Table E.4. The shape of the modeling codes are similar as for the $^{nat}Y(n,x)^{87}Y$ reaction wcich is to be expected. The shape will generally be similar for the ground state and the isomer state. How the modelling codes partitions these states are the big difference.

$^{nat}Y(n,x)^{90m}Y$

The first-time measured spectrum-average cross section for ^{90m}Y is shown in Figure E.4d and listed in Table E.4. The modeling codes are not in agreement with each other and more experimental points are needed to identify which modeling code that agrees best. For 16 MeV neutrons, TENDL shows the best agreement.

Bibliography

[1] M. Sklodowska Curie, "Rayons émis par les composés de l'uranium et du thorium," *Comptes Rendus Hebdomadaires des Séances de l'Académie des Sciences*, vol. 126, pp. 1101–1103, 1898.

[2] F. Farina Arboccò, P. Vermaercke, K. Smits, L. Sneyers, and K. Strijckmans, "Experimental determination of K_0, Q_0, $\bar{E}_r$ factors and neutron cross-sections for 41 isotopes of interest in Neutron Activation Analysis," *Journal of Radioanalytical and Nuclear Chemistry*, vol. 296, pp. 931–938, may 2013.

[3] WHO, "Cancer," 2018. `https://www.who.int/news-room/fact-sheets/detail/cancer`.

[4] G. Hevesy, "The Absorption and Translocation of Lead by Plants. A Contribution to the Application of the Method of Radioactive Indicators in the Investigation of the Change of Substance in Plants," in *A Source Book in Chemistry, 1900-1950*, pp. 48–50, Cambridge, MA and London, England: Harvard University Press, dec 1968.

[5] H. L. Blumgart and S. Weiss, "STUDIES ON THE VELOCITY OF BLOOD FLOW," *Journal of Clinical Investigation*, vol. 4, pp. 399–425, aug 1927.

[6] A. Koning, D. Rochman, J.-C. Sublet, N. Dzysiuk, M. Fleming, and S. van der Marck, "TENDL: Complete Nuclear Data Library for Innovative Nuclear Science and Technology," *Nuclear Data Sheets*, vol. 155, pp. 1–55, jan 2019.

[7] M. Herman, R. Capote, B. Carlson, P. Obložinský, M. Sin, A. Trkov, H. Wienke, and V. Zerkin, "EMPIRE: Nuclear Reaction Model Code System for Data Evaluation," *Nuclear Data Sheets*, vol. 108, pp. 2655–2715, dec 2007.

[8] A. Koning and D. Rochman, "Modern Nuclear Data Evaluation with the TALYS Code System," *Nuclear Data Sheets*, vol. 113, pp. 2841–2934, dec 2012.

[9] T. KAWANO, P. TALOU, M. B. CHADWICK, and T. WATANABE, "Monte Carlo Simulation for Particle and γ-Ray Emissions in Statistical Hauser-Feshbach Model," *Journal of Nuclear Science and Technology*, vol. 47, pp. 462–469, may 2010.

[10] M. Blann, "New precompound decay model," *Physical Review C*, vol. 54, pp. 1341–1349, sep 1996.

[11] A. Perkins, "In vivo molecular targeted radiotherapy," *Biomedical Imaging and Intervention Journal*, vol. 1, pp. 53–74, oct 2005.

[12] C.-H. Yeong, M.-H. Cheng, and K.-H. Ng, "Therapeutic radionuclides in nuclear medicine: current and future prospects," *Journal of Zhejiang University SCIENCE B*, vol. 15, pp. 845–863, oct 2014.

[13] B. Izar, D. P. Ryan, and B. A. Chabner, *Principles of Chemotherapy*. Elsevier Inc., fourth edi ed., 2015.

[14] C. L. Holloway, D. A. O'Farrell, P. M. Devlin, and A. J. Stewart, *Brachytherapy*. Elsevier Inc., fourth edi ed., 2015.

[15] W. P. Levin and T. F. DeLaney, *Charged Particle Radiotherapy*. Elsevier Inc., fourth edi ed., 2015.

[16] J. G. Jurcic, J. Y. Wong, S. J. Knox, D. R. Wahl, T. L. Rosenblat, and R. F. Meredith, *Targeted Radionuclide Therapy*. Elsevier Inc., fourth edi ed., 2015.

[17] K. S. Krane, *Introductory nuclear physics*. John Wiley & Sons, inc, 1987.

[18] D. R. Tilley, H. R. Weller, C. M. Cheves, and R. M. Chasteler, "Energy levels of light nuclei A = 18-19," *Nuclear Physics, Section A*, vol. 595, no. 1, pp. 1–170, 1995.

[19] L. Bailey., D. L. Humm., J. A. Todd-Pokropek., and A. van Aswegen, *Nuclear medicine physics : a handbook for students and teachers*. IAEA Library Cataloguing in Publication Data, 2014.

[20] A. Vertes, S. Nagy, Z. Klencsar, R. G. Lovas, and F. Rosch, *Handbook of Nuclear Chemistry*. Boston, MA: Springer US, 2011.

[21] E. M. Zeman, "The Biological Basis of Radiation Oncology," in *Clinical Radiation Oncology*, pp. 2–40.e5, Elsevier, fourth edi ed., 2016.

[22] S. R. Cherry, J. A. Sorenson, and M. E. Phelps, "Modes of Radioactive Decay," in *Physics in Nuclear Medicine*, pp. 19–30, Elsevier, 2012.

[23] L. Jødal, "Beta emitters and radiation protection," *Acta Oncologica*, vol. 48, no. 2, pp. 308–313, 2009.

[24] F. Buchegger, F. Perillo-Adamer, Y. M. Dupertuis, and A. Bischof Delaloye, "Auger radiation targeted into DNA: a therapy perspective," *European Journal of Nuclear Medicine and Molecular Imaging*, vol. 33, pp. 1352–1363, oct 2006.

[25] S. R. Cherry, J. A. Sorenson, and M. E. Phelps, "Basic Atomic and Nuclear Physics, chapter 3," in *Physics in Nuclear Medicine*, pp. 7–18, Elsevier, 2012.

[26] B. Q. Lee, T. Kibédi, A. E. Stuchbery, and K. A. Robertson, "Atomic Radiations in the Decay of Medical Radioisotopes: A Physics Perspective," *Computational and Mathematical Methods in Medicine*, vol. 2012, pp. 1–14, 2012.

[27] F. H. Attix, *Introduction to radiological physics and radiation dosimetry*. WILEY-VCH Verlag GmbH & Co. KGaA, Weinheim, 2004.

[28] M. Gruber, "Electronic and magnetic properties of hybrid interfaces. From single molecules to ultra- thin molecular films on metallic substrates.," 2014.

[29] R. C. Gupta, *Handbook of toxicology of chemical warfare agents, second edition*. San Val, 2015.

[30] H. Junde, H. Xiaolong, and J. K. Tuli, "Nuclear data sheets for A= 67," *Nuclear Data Sheets*, vol. 106, no. 2, pp. 159–250, 2005.

[31] I. Preiss and R. Fink, "New isotopes of cobalt; Activation cross-sections of nickel, cobalt, and zinc for 14.8 MeV neutrons," *Nuclear Physics*, vol. 15, pp. 326–336, feb 1960.

[32] G. R. Gilmore and J. Wiley, *Practical Gamma-ray Spectrometry 2nd Edition*. 2011.

[33] "Analysis of gama spectrum," tech. rep., Linkopings Universitet, The department of physics, chemistry and biology, 2018.

[34] E. Lawrence, "The evolution of the cyclotron," 1951.

[35] *Cyclotron Produced Radionuclides: Principles and Practice*. No. 465 in Technical Reports Series, Vienna: INTERNATIONAL ATOMIC ENERGY AGENCY, 2009.

[36] A. Nassiri, B. Chase, P. Craievich, A. Fabris, H. Frischholz, J. Jacob, E. Jensen, M. Jensen, R. Kustom, and R. Pasquinelli, "History and Technology Developments of Radio Frequency (RF) Systems for Particle Accelerators," *IEEE Transactions on Nuclear Science*, vol. 63, pp. 707–750, apr 2016.

[37] S. Braccini, "Compact medical cyclotrons and their use for radioisotope production and multi-disciplinary research," *CYC 2016 - Proceedings of the 21st International Conference on Cyclotrons and their Applications*, pp. 229–234, 2016.

[38] F. R. Wrenn, M. L. Good, and P. Handler, "The Use of Positron-emitting Radioisotopes for the Localization of Brain Tumors," *Science*, vol. 113, pp. 525–527, may 1951.

[39] P. V. Harper, R. A. Fink, D. B. Charleston, R. N. Beck, K. A. Lathrop, and J. P. Evans, "Rapid Brain Scanning with Technetium-99m," *Acta Radiologica. Diagnosis*, vol. 5, pp. 819–831, mar 1966.

[40] S. R. Cherry, J. A. Sorenson, and M. E. Phelps, "What Is Nuclear Medicine?," in *Physics in Nuclear Medicine*, pp. 1–6, Elsevier, 2012.

[41] S. Vallabhajosula, *Molecular Imaging: Radiopharmaceuticals for PET and SPECT*. Springer-Verlag Berlin Heidelberg, 2009.

[42] S. R. Cherry, J. A. Sorenson, and M. E. Phelps, "Positron Emission Tomography," in *Physics in Nuclear Medicine*, pp. 307–343, Elsevier, 2012.

[43] K. Duncan, "Radiopharmaceuticals in PET imaging," *Journal of Nuclear Medicine Technology*, vol. 26, no. 4, pp. 228–234, 1998.

[44] J. H. Kelley, E. Kwan, J. E. Purcell, C. G. Sheu, and H. R. Weller, "Energy levels of light nuclei A=11," *Nuclear Physics A*, vol. 880, pp. 88–195, 2012.

[45] F. Ajzenberg-selove, J. H. Kelley, and C. D. Nesaraja, "Adopted levels, gammas for ^{13}C," *nndc. bnl. gov*, 2019.

[46] F. Ajzenberg-Selove, "Energy levels of light nuclei A = 13-15," *Nuclear Physics, Section A*, vol. 523, no. 1, pp. 1–196, 1991.

[47] B. Singh, "Nuclear Data Sheets for A = 64," *Nuclear Data Sheets*, vol. 108, pp. 197–364, feb 2007.

[48] E. A. McCutchan, "Nuclear Data Sheets for A = 68," *Nuclear Data Sheets*, vol. 113, no. 6-7, pp. 1735–1870, 2012.

[49] J. Katakura and Z. D. Wu, "Nuclear Data Sheets for A = 124," *Nuclear Data Sheets*, vol. 109, no. 7, pp. 1655–1877, 2008.

[50] S. R. Cherry, J. A. Sorenson, and M. E. Phelps, "Radionuclide and Radiopharmaceutical Production," *Physics in Nuclear Medicine*, pp. 43–61, 2012.

[51] K. A. Johnson, N. C. Fox, R. A. Sperling, and W. E. Klunk, "Brain Imaging in Alzheimer Disease," *Cold Spring Harbor Perspectives in Medicine*, vol. 2, pp. a006213–a006213, apr 2012.

[52] M. Hildebrandt, J. Lauridsen, M. Vogsen, J. Holm, M. Vilstrup, P.-E. Braad, O. Gerke, M. Thomassen, M. Ewertz, and P. Høilund-Carlsen, "FDG-PET/CT for Response Monitoring in Metastatic Breast Cancer: Today, Tomorrow, and Beyond," *Cancers*, vol. 11, p. 1190, aug 2019.

[53] J. J. Bailey, L. Kaiser, S. Lindner, M. Wüst, A. Thiel, J.-P. Soucy, P. Rosa-Neto, P. J. H. Scott, M. Unterrainer, D. R. Kaplan, C. Wängler, B. Wängler, P. Bartenstein, V. Bernard-Gauthier, and R. Schirrmacher, "First-in-Human Brain Imaging of [^{18}F]TRACK, a PET tracer for Tropomyosin Receptor Kinases," *ACS Chemical Neuroscience*, vol. 10, pp. 2697–2702, jun 2019.

[54] H. Ito, H. Kubo, K. Takahashi, and S. Ishii, "Measurement of cerebral circulation and oxygen metabolism using integrated PET/MRI scanner with oxygen-15 labeled gases: Effects of attenuation correction and real-time motion correction," *Journal of Nuclear Medicine*, vol. 61, no. supplement 1, p. 75, 2020.

[55] T. Jones, D. A. Chesler, and M. M. Ter-Pogossian, "The continuous inhalation of Oxygen-15 for assessing regional oxygen extraction in the brain of man," *The British Journal of Radiology*, vol. 49, pp. 339–343, apr 1976.

[56] A. Ahmedova, B. Todorov, N. Burdzhiev, and C. Goze, "Copper radiopharmaceuticals for theranostic applications," *European Journal of Medicinal Chemistry*, vol. 157, pp. 1406–1425, sep 2018.

[57] P. Herrero, J. J. Hartman, M. A. Green, C. J. Anderson, M. J. Welch, J. Markham, and S. R. Bergmann, "Regional myocardial perfusion assessed with generator-produced copper- 62-PTSM and PET," *Journal of Nuclear Medicine*, vol. 37, no. 8, pp. 1294–3000, 1996.

[58] M. E. Shelton, M. A. Green, C. J. Mathias, M. J. Welch, and S. R. Bergmann, "Assessment of regional myocardial and renal blood flow with copper-PTSM and positron emission tomography.," *Circulation*, vol. 82, pp. 990–997, sep 1990.

[59] A. Ahmedova, B. Todorov, N. Burdzhiev, and C. Goze, "Copper radiopharmaceuticals for theranostic applications," *European Journal of Medicinal Chemistry*, vol. 157, pp. 1406–1425, sep 2018.

[60] P. J. Blower, J. S. Lewis, and J. Zweit, "Copper radionuclides and radiopharmaceuticals in nuclear medicine," *Nuclear Medicine and Biology*, vol. 23, pp. 957–980, nov 1996.

[61] E. Browne and J. Tuli, "Nuclear Data Sheets for A = 60," *Nuclear Data Sheets*, vol. 114, pp. 1849–2022, dec 2013.

[62] K. Zuber and B. Singh, "Nuclear Data Sheets for A = 61," *Nuclear Data Sheets*, vol. 125, pp. 1–200, mar 2015.

[63] A. L. Nichols, B. Singh, and J. K. Tuli, "Nuclear Data Sheets for A = 62," *Nuclear Data Sheets*, vol. 113, pp. 973–1114, apr 2012.

[64] E. Browne and J. Tuli, "Nuclear Data Sheets for A = 66," *Nuclear Data Sheets*, vol. 111, pp. 1093–1209, apr 2010.

[65] J. R. Turnlund, W. R. Keyes, G. L. Peiffer, and K. C. Scott, "Copper absorption, excretion, and retention by young men consuming low dietary copper determined by using the stable isotope ^{65}Cu," *American Journal of Clinical Nutrition*, vol. 67, no. 6, pp. 1219–1225, 1998.

[66] J. Osredkar, "Copper and Zinc, Biological Role and Significance of Copper/Zinc Imbalance," *Journal of Clinical Toxicology*, vol. s3, no. 01, 2011.

[67] H. A. Williams, S. Robinson, P. Julyan, J. Zweit, and D. Hastings, "A comparison of PET imaging characteristics of various copper radioisotopes," *European Journal of Nuclear Medicine and Molecular Imaging*, vol. 32, pp. 1473–1480, dec 2005.

[68] D. Denoyer, S. Masaldan, S. La Fontaine, and M. A. Cater, "Targeting copper in cancer therapy: 'Copper That Cancer'," *Metallomics*, vol. 7, no. 11, pp. 1459–1476, 2015.

[69] K. A. Koch, M. M. O. Peña, and D. J. Thiele, "Copper-binding motifs in catalysis, transport, detoxification and signaling," *Chemistry & Biology*, vol. 4, pp. 549–560, aug 1997.

[70] W. T. Johnson and C. M. Anderson, "Cardiac Cytochrome c Oxidase Activity and Contents of Subunits 1 and 4 Are Altered in Offspring by Low Prenatal Copper Intake by Rat Dams," *The Journal of Nutrition*, vol. 138, pp. 1269–1273, jul 2008.

[71] A. Gupta and S. Lutsenko, "Human copper transporters: mechanism, role in human diseases and therapeutic potential," *Future Medicinal Chemistry*, vol. 1, pp. 1125–1142, sep 2009.

[72] Z. Zhou, W. T. Johnson, and Y. J. Kang, "Regression of copper-deficient heart hypertrophy: reduction in the size of hypertrophic cardiomyocytes," *The Journal of Nutritional Biochemistry*, vol. 20, pp. 621–628, aug 2009.

[73] Z. Cai and C. J. Anderson, "Chelators for copper radionuclides in positron emission tomography radiopharmaceuticals," *Journal of Labelled Compounds and Radiopharmaceuticals*, vol. 57, pp. 224–230, apr 2014.

[74] M. Tegoni, D. Valensin, L. Toso, and M. Remelli, *Copper Chelators: Chemical Properties and Bio-medical Applications*, vol. 21. 2014.

[75] D. Sarko, M. Eisenhut, U. Haberkorn, and W. Mier, "Bifunctional Chelators in the Design and Application of Radiopharmaceuticals for Oncological Diseases," *Current Medicinal Chemistry*, vol. 19, no. 17, pp. 2667–2688, 2012.

[76] C. J. Anderson, T. S. Pajeau, W. B. Edwards, E. L. C. Sherman, B. E. Rogers, and M. J. Welch, "In Vitro and In Vivo Evaluation of Copper-64-Octreotide Conjugates Thr (OL) -cys-Th," pp. 2315–2326, 1995.

[77] M. Wang, A. L. Caruano, M. R. Lewis, L. A. Meyer, R. P. VanderWaal, and C. J. Anderson, "Subcellular Localization of Radiolabeled Somatostatin Analogues: Implications for Targeted Radiotherapy of Cancer," *Cancer Research*, vol. 63, no. 20, pp. 6864–6869, 2003.

[78] I. H. Scheinberg, M. E. Jaffe, and I. Sternlieb, "The Use of Trientine in Preventing the Effects of Interrupting Penicillamine Therapy in Wilson's Disease," *New England Journal of Medicine*, vol. 317, pp. 209–213, jul 1987.

[79] G. J. Cooper, "Therapeutic Potential of Copper Chelation with Triethylenetetramine in Managing Diabetes Mellitus and Alzheimers Disease," *Drugs*, vol. 71, pp. 1281–1320, jul 2011.

[80] G. J.S. Cooper, "Selective Divalent Copper Chelation for the Treatment of Diabetes Mellitus," *Current Medicinal Chemistry*, vol. 19, pp. 2828–2860, may 2012.

[81] J. Liu, L. Guo, F. Yin, X. Zheng, G. Chen, and Y. Wang, "Characterization and antitumor activity of triethylene tetramine, a novel telomerase inhibitor," *Biomedicine & Pharmacotherapy*, vol. 62, pp. 480–485, sep 2008.

[82] T. Traub, V. Petkov, S. Ofluoglu, T. Pangerl, M. Raderer, B. J. Fueger, W. Schima, A. Kurtaran, R. Dudczak, and I. Virgolini, "^{111}In-DOTA-lanreotide scintigraphy in patients with tumors of the lung," *Journal of Nuclear Medicine*, vol. 42, no. 9, pp. 1309–1315, 2001.

[83] Z. Baranyai, G. Tircsó, and F. Rösch, "The Use of the Macrocyclic Chelator DOTA in Radiochemical Separations," *European Journal of Inorganic Chemistry*, vol. 2020, pp. 36–56, jan 2020.

[84] M. Henze, J. Schuhmacher, P. Hipp, J. Kowalski, D. W. Becker, J. Doll, H. R. Mäcke, M. Hofmann, J. Debus, and U. Haberkorn, "PET imaging of somatostatin receptors using [^{68}GA] DOTA-D-Phe1-Tyr3-octreotide: first results in patients with meningiomas," *Journal of Nuclear Medicine*, vol. 42, no. 7, pp. 1053–1056, 2001.

[85] L. Gaetke, "Copper toxicity, oxidative stress, and antioxidant nutrients," *Toxicology*, vol. 189, pp. 147–163, jul 2003.

[86] J. F. Collins and L. M. Klevay, "Copper," *Advances in Nutrition*, vol. 2, pp. 520–522, nov 2011.

[87] S. Environmental, "Copper : Health Information Summary," *Environmental Fact Sheet*, pp. 0–2, 2013.

[88] A. R. Jalilian and J. Osso, "The current status and future of theranostic Copper-64 radiopharmaceuticals," *Iranian Journal of Nuclear Medicine*, vol. 25, no. 1, pp. 1–10, 2017.

[89] A. Pfeifer, U. Knigge, J. Mortensen, P. Oturai, A. K. Berthelsen, A. Loft, T. Binderup, P. Rasmussen, D. Elema, T. L. Klausen, S. Holm, E. von Benzon, L. Hojgaard, and A. Kjaer, "Clinical PET of Neuroendocrine Tumors Using ^{64}Cu-DOTATATE: First-in-Humans Study," *Journal of Nuclear Medicine*, vol. 53, pp. 1207–1215, aug 2012.

[90] G. L. DeNardo, D. L. Kukis, S. Shen, D. A. DeNardo, C. F. Meares, and S. J. DeNardo, "^{67}Cu- versus ^{131}I-labeled Lym-1 antibody: Comparative pharmacokinetics and dosimetry in patients with non-Hodgkin's lymphoma," *Clinical Cancer Research*, vol. 5, no. 3, pp. 533–541, 1999.

[91] R. T. O'Donnell, G. L. DeNardo, D. L. Kukis, K. R. Lamborn, S. Shen, A. Yuan, D. S. Goldstein, C. E. Carr, G. R. Mirick, and S. J. DeNardo, "A clinical trial of radioimmunotherapy with ^{67}Cu-2IT-BAT-Lym-1 for Non-Hodgkin's lymphoma," *Journal of Nuclear Medicine*, vol. 40, no. 12, pp. 2014–2020, 1999.

[92] G. L. Denardo, S. J. Denardo, D. L. Kukis, R. T. O'Donnell, S. Shen, D. S. Goldstein, L. A. Kroger, Q. Salako, D. A. Denardo, G. R. Mirick, L. F. Mausner, S. C. Srivastava, and C. F. Meares, "Maximum tolerated dose of ^{67}Cu-2IT-BAT-LYM-1 for fractionated radioimmunotherapy of non-Hodgkin's lymphoma: a pilot study.," *Anticancer research*, vol. 18, no. 4B, pp. 2779–2788, 1998.

[93] C. Mucin and P. Schubiger, "Targeting Superficial Bladder Cancer by the Intravesical," vol. 18, no. 2, pp. 363–370, 2000.

[94] C. Biggin, M. Harris, A. Hedt, and C. Jeffery, "Radiological properties of Next Generation Theranostics (Cu-64/Cu-67)," *Journal of Nuclear Medicine*, vol. 58, no. supplement 1, p. 1014, 2017.

[95] J. R. Ballinger, "Theranostic radiopharmaceuticals: established agents in current use.," *Br J Radiol*, vol. 91, no. 1091, p. 1, 2018.

[96] Müller, Cristina and Bunka, Maruta and Haller, Stephanie and Köster, Ulli and Groehn, Viola and Bernhardt, Peter and van der Meulen, Nicholas and Türler, Andreas and Schibli, Roger , "Promising Prospects for ^{44}Sc-/^{47}Sc-Based Theragnostics: Application of ^{47}Sc for Radionuclide Tumor Therapy in Mice," *Journal of Nuclear Medicine*, vol. 55, no. 55, pp. 1658–1664, 2014.

[97] Q. S. Rösch Frank Herzog Hans, "The Beginning and Development of the Theranostic Approach in Nuclear Medicine, as Exemplified by the Radionuclide Pair ^{86}Y and ^{90}Y," *Pharmaceuticals*, vol. 10, no. 4, p. 56, 2017.

[98] Sneha S. Kelkar. Theresa M. Reineke., "Theranostics: Combining Imaging and Therapy," *Bioconjugate Chem*, vol. 22, no. 10, pp. 1879–1903, 2011.

[99] D. D. Ellingsen, N. Horn, and J. Aaseth, "Handbook on the Toxicology of Metals (Third Edition), Chapter 26," no. Ii, 2007.

[100] F. Peng, S. Lutsenko, X. Sun, and O. Muzik, "Positron Emission Tomography of Copper Metabolism in the Atp7b / Knock-out Mouse Model of Wilson's Disease," *Molecular Imaging and Biology*, vol. 14, pp. 70–78, feb 2012.

[101] L. Sonzogni and B. Shu, "NuDat 2.8." `https://www.nndc.bnl.gov/nudat2/reZoom.jsp?newZoom=1`.

[102] D. W. McCarthy, R. E. Shefer, R. E. Klinkowstein, L. A. Bass, W. H. Margeneau, C. S. Cutler, C. J. Anderson, and M. J. Welch, "Efficient production of high specific activity ^{64}Cu using a biomedical cyclotron," *Nuclear Medicine and Biology*, vol. 24, pp. 35–43, jan 1997.

[103] C. Alliot, N. Michel, A.-C. Bonraisin, V. Bossé, J. Laizé, C. Bourdeau, B. M. Mokili, and F. Haddad, "One step purification process for no-carrier-added ^{64}Cu produced using enriched nickel target," *Radiochimica Acta*, vol. 99, pp. 627–630, oct 2011.

[104] D. C. Santry and J. P. Butler, "Excitation Curves for the Reactions of Fast Neutrons with Zinc," *Canadian Journal of Physics*, vol. 50, pp. 2536–2548, oct 1972.

[105] T. Katabuchi, S. Watanabe, N. S. Ishioka, Y. Iida, H. Hanaoka, K. Endo, and S. Matsuhashi, "Production of ^{67}Cu via the ^{68}Zn(p,2p)^{67}Cu reaction and recovery of ^{68}Zn target," *Journal of Radioanalytical and Nuclear Chemistry*, vol. 277, pp. 467–470, aug 2008.

[106] K. Hilgers, T. Stoll, Y. Skakun, H. Coenen, and S. Qaim, "Cross-section measurements of the nuclear reactions $^{nat}Zn(d,x)^{64}Cu$, ^{66}Zn(d,α)^{64}Cu and ^{68}Zn(p,αn)^{64}Cu for production of ^{64}Cu and technical developments for small-scale production of ^{67}Cu via the ^{70}Zn(p,α)^{67}Cu process," *Applied Radiation and Isotopes*, vol. 59, pp. 343–351, nov 2003.

[107] A. Obata, S. Kasamatsu, D. W. McCarthy, M. J. Welch, H. Saji, Y. Yonekura, and Y. Fujibayashi, "Production of therapeutic quantities of ^{64}Cu using a 12 MeV cyclotron," *Nuclear Medicine and Biology*, vol. 30, pp. 535–539, may 2003.

[108] K. Abbas, J. Kozempel, M. Bonardi, F. Groppi, A. Alfarano, U. Holzwarth, F. Simonelli, H. Hofman, W. Horstmann, E. Menapace, L. Lešetický, and N. Gibson, "Cyclotron production of ^{64}Cu by deuteron irradiation of ^{64}Zn," *Applied Radiation and Isotopes*, vol. 64, pp. 1001–1005, sep 2006.

[109] F. Szelecsényi, G. F. Steyn, Z. Kovács, C. Vermeulen, N. P. Van Der Meulen, S. G. Dolley, T. N. Van Der Walt, K. Suzuki, and K. Mukai, "Investigation of the ^{66}Zn(p,2pn)^{64}Cu and ^{68}Zn(p,x)^{64}Cu nuclear processes up to 100 MeV: Production of ^{64}Cu," *Nuclear Instruments and Methods in Physics Research, Section B: Beam Interactions with Materials and Atoms*, vol. 240, no. 3, pp. 625–637, 2005.

[110] T. Stoll, S. Kastleiner, Y. N. Shubin, H. H. Coenen, and S. M. Qaim, "Excitation functions of proton induced reactions on ^{68}Zn from threshold up to 71 MeV, with specific reference to the production of ^{67}Cu," *Radiochimica Acta*, vol. 90, pp. 309–313, jan 2002.

[111] S. Kastleiner, H. H. Coenen, and S. M. Qaim, "Possibility of Production of ^{67}Cu at a Small-Sized Cyclotron via the (p,α)-Reaction on Enriched ^{70}Zn," *Radiochimica Acta*, vol. 84, jan 1999.

[112] J. A. Favorite, "The solid angle (geometry factor) for a spherical surface source and an arbitrary detector aperture," *Nuclear Instruments and Methods in Physics Research Section A: Accelerators, Spectrometers, Detectors and Associated Equipment*, vol. 813, pp. 29–35, mar 2016.

[113] Ashland Inc., "GAFChromic^{TM} EBT3 film specifications," pp. 1 – 5, 2014.

[114] J. Sorriaux, A. Kacperek, S. Rossomme, J. A. Lee, D. Bertrand, S. Vynckier, and E. Sterpin, "Evaluation of Gafchromic® EBT3 films characteristics in therapy photon, electron and proton beams," *Physica Medica*, vol. 29, no. 6, pp. 599–606, 2013.

[115] A. S. Voyles, L. A. Bernstein, E. R. Birnbaum, J. W. Engle, S. A. Graves, T. Kawano, A. M. Lewis, and F. M. Nortier, "Excitation functions for (p,x) reactions of niobium in the energy range of E p = 40–90 MeV," *Nuclear Instruments and Methods in Physics Research Section B: Beam Interactions with Materials and Atoms*, vol. 429, pp. 53–74, aug 2018.

[116] E. Browne and J. Tuli, "Nuclear Data Sheets for A = 137," *Nuclear Data Sheets*, vol. 108, pp. 2173–2318, oct 2007.

[117] Y. Khazov, A. Rodionov, and F. Kondev, "Nuclear Data Sheets for A = 133," *Nuclear Data Sheets*, vol. 112, pp. 855–1113, apr 2011.

[118] M. Martin, "Nuclear Data Sheets for A = 152," *Nuclear Data Sheets*, vol. 114, pp. 1497–1847, nov 2013.

[119] W. J. Gallagher and S. J. Cipolla, "A model-based efficiency calibration of a Si(Li) detector in the energy region from 3 to 140 keV," *Nuclear Instruments and Methods*, vol. 122, pp. 405–414, nov 1974.

[120] J. P. Meulders, P. Leleux, P. C. Macq, and C. Pirart, "Fast neutron yields and spectra from targets of varying atomic number bombarded with deuterons from 16 to 50 MeV (for radiobiology and radiotherapy)," *Physics in Medicine and Biology*, vol. 20, p. 005, mar 1975.

[121] M. Saltmarsh, C. Ludemann, C. Fulmer, and R. Styles, "Characteristics of an intense neutron source based on the d+Be reaction," *Nuclear Instruments and Methods*, vol. 145, pp. 81–90, aug 1977.

[122] J. H. Kelley and J. L. Godwin, "Adopted Levels for A=2 ENSDF 2," vol. 5, p. 1983, 2003.

[123] Jim Fitzgerald, "FitzPeaks Gamma analysis and calibration software." `https://www.jimfitz.co.uk/fitzpeak.htm`.

[124] M. J. Koskelo, P. A. Aarnio, and J. T. Routti, "SAMPO80: An accurate gamma spectrum analysis method for minicomputers," *Nuclear Instruments and Methods in Physics Research*, vol. 190, pp. 89–99, nov 1981.

[125] M. J. Berger, J. H. Hubbell, S. M. Seltzer, J. Chang, J. S. Coursey, R. Sukumar, D. S. Zucker, and K. Olsen, "NIST standard reference database 8 (XGAM)," *XCOM: Photon Cross Sections Database*, 2008.

[126] M. J. Berger, J. H. Hubbell, S. Seltzer, J. Chang, J. Coursey, R. S. Mar, D. Zucker, and K. Olsen, "XCOM: Photon Cross Sections Databasee," *International Journal of Physics*, vol. 4, no. 2, pp. 37–42, 2016.

[127] S. R. Cherry, J. A. Sorenson, and M. E. Phelps, "Decay of Radioactivity," in *Physics in Nuclear Medicine*, pp. 31–42, Elsevier, 2012.

[128] O. M. Pop, V. M. Simulik, and M. V. Stets, "Nuclide Spectra of Activities of Thorium, Uranium Series and Application in Gamma-spectrometry of Point Technogenic Samples," *International Journal of Physics*, vol. 4, no. March, pp. 37–42, 2016.

[129] T. Johnson and W. Kulp, "Nuclear Data Sheets for A = 87," *Nuclear Data Sheets*, vol. 129, pp. 1–190, nov 2015.

[130] A. Trkov, P. Griffin, S. Simakov, L. Greenwood, K. Zolotarev, R. Capote, D. Aldama, V. Chechev, C. Destouches, A. Kahler, C. Konno, M. Koštál, M. Majerle, E. Malambu, M. Ohta, V. Pronyaev, V. Radulović, S. Sato, M. Schulc, E. Šimečková, I. Vavtar, J. Wagemans, M. White, and H. Yashima, "IRDFF-II: A New Neutron Metrology Library," *Nuclear Data Sheets*, vol. 163, pp. 1–108, jan 2020.

[131] K. Harrig, B. Goldblum, J. Brown, D. Bleuel, L. Bernstein, J. Bevins, M. Harasty, T. Laplace, and E. Matthews, "Neutron Spectroscopy for pulsed beams with frame overlap using a double time-of-flight technique," *Nuclear Instruments and Methods in Physics Research Section A: Accelerators, Spectrometers, Detectors and Associated Equipment*, vol. 877, pp. 359–366, jan 2018.

[132] T. J. Morrell, "Privat comunication on 33 MeV deutreron breakup spectrum..".

[133] A. Colombi, F. Barbaro, L. Canton, M. P. Carante, and A. Fontana, "Modeling Nuclear Reactions for PET/MRI MultiModal Imaging: the innovative use of 52," no. 2, pp. 52–53, 2020.

[134] L. Greenwood, "Recent Research in Neutron Dosimetry and Damage Analysis for Materials Irradiations," in *Influence of Radiation on Material Properties: 13th International Symposium (Part II)*, pp. 743–743–7, 100 Barr Harbor Drive, PO Box C700, West Conshohocken, PA 19428-2959: ASTM International.

[135] N. Otuka, E. Dupont, V. Semkova, B. Pritychenko, A. Blokhin, M. Aikawa, S. Babykina, M. Bossant, G. Chen, S. Dunaeva, R. Forrest, T. Fukahori, N. Furutachi, S. Ganesan, Z. Ge, O. Gritzay, M. Herman, S. Hlavač, K. Katō, B. Lalremruata, Y. Lee, A. Makinaga, K. Matsumoto, M. Mikhaylyukova, G. Pikulina, V. Pronyaev, A. Saxena, O. Schwerer, S. Simakov, N. Soppera, R. Suzuki, S. Takács, X. Tao, S. Taova, F. Tárkányi, V. Varlamov, J. Wang, S. Yang, V. Zerkin, and Y. Zhuang, "Towards a More Complete and Accurate Experimental Nuclear Reaction Data Library (EXFOR): International Collaboration Between Nuclear Reaction Data Centres (NRDC)," *Nuclear Data Sheets*, vol. 120, pp. 272–276, jun 2014.

[136] Y. UWAMINO, H. SUGITA, Y. KONDO, and T. NAKAMURA, "Measurement of Neutron Activation Cross Sections for Energies up to 40MeV for Natural Samples of Mg, Si, Ca, V, Cr, Cu and Zn.," *Journal of Nuclear Science and Technology*, vol. 31, no. 1, pp. 1–11, 1994.

[137] G. L. Squires, *Practical Physics*. Cambridge University Press, fourth edition, 2001.

[138] R. J. Carroll, S. Wang, D. G. Simpson, a. J. Stromberg, and D. Ruppert, "The sandwich (robust covariance matrix) estimator," no. January, p. 16, 1998.

[139] B. Erjun and H. Junde, "Nuclear Data Sheets for A = 63," *Nuclear Data Sheets*, vol. 92, pp. 147–252, jan 2001.

[140] E. Browne and J. Tuli, "Nuclear Data Sheets for A = 65," *Nuclear Data Sheets*, vol. 111, pp. 2425–2553, sep 2010.

[141] C. Nesaraja, "Nuclear Data Sheets for A=69," *Nuclear Data Sheets*, vol. 115, pp. 1–134, jan 2014.

[142] B. Singh, "Nuclear Data Sheets for A = 89," *Nuclear Data Sheets*, vol. 114, no. 1, pp. 1–208, 2013.

[143] E. Browne, "Nuclear Data Sheets for A = 90," *Nuclear Data Sheets*, vol. 82, pp. 379–546, nov 1997.

[144] C. M. Baglin, "Nuclear Data Sheets for A = 91," *Nuclear Data Sheets*, vol. 114, pp. 1293–1495, oct 2013.

[145] C. M. Baglin, "Nuclear Data Sheets for A = 92," *Nuclear Data Sheets*, vol. 113, pp. 2187–2389, oct 2012.

[146] C. M. Baglin, "Nuclear Data Sheets for A = 93," *Nuclear Data Sheets*, vol. 112, pp. 1163–1389, may 2011.

[147] S. Basu, G. Mukherjee, and A. Sonzogni, "Nuclear Data Sheets for A = 95," *Nuclear Data Sheets*, vol. 111, pp. 2555–2737, oct 2010.

[148] N. Nica, "Nuclear Data Sheets for A = 97," *Nuclear Data Sheets*, vol. 111, pp. 525–716, mar 2010.

[149] E. McCutchan and A. Sonzogni, "Nuclear Data Sheets for A = 88," *Nuclear Data Sheets*, vol. 115, pp. 135–304, jan 2014.

[150] J. Blachot, "Nuclear data sheets for A = 111," *Nuclear Data Sheets*, vol. 77, pp. 299–432, oct 1996.

[151] S. Lalkovski and F. Kondev, "Nuclear Data Sheets for A = 112," *Nuclear Data Sheets*, vol. 124, pp. 157–412, feb 2015.

[152] J. Blachot, "Nuclear Data Sheets for A = 113," *Nuclear Data Sheets*, vol. 111, pp. 1471–1618, jun 2010.

[153] J. Blachot, "Nuclear Data Sheets for A = 114," *Nuclear Data Sheets*, vol. 113, pp. 515–714, feb 2012.

[154] J. Blachot, "Nuclear Data Sheets for A = 115," *Nuclear Data Sheets*, vol. 113, pp. 2391–2535, oct 2012.

[155] J. Blachot, "Nuclear Data Sheets for A = 116," *Nuclear Data Sheets*, vol. 111, pp. 717–895, mar 2010.

[156] R. Firestone, "Nuclear Data Sheets for A = 24," *Nuclear Data Sheets*, vol. 108, pp. 2319–2392, nov 2007.

[157] J. Vrzalová, O. Svoboda, A. Krása, A. Kugler, M. Majerle, M. Suchopár, and V. Wagner, "Studies of (n,xn) cross-sections in Al, Au, Bi, Cu, Fe, I, In, Mg, Ni, Ta, Y, and Zn by the activation method," *Nuclear Instruments and Methods in Physics Research Section A: Accelerators, Spectrometers, Detectors and Associated Equipment*, vol. 726, pp. 84–90, oct 2013.

[158] S. Rehncrona, J. Brismar, and S. Holtås, "Diagnosis of Brain Abscesses with Indium-111-labeled Leukocytes," *Neurosurgery*, vol. 16, pp. 23–26, jan 1985.

[159] B. A. Sayle, R. E. Helmer, B. A. Birdsong, S. Balachandran, and F. H. Gardner, "Bone-marrow imaging with indium-111 chloride in aplastic anemia and myelofibrosis: Concise communication," *Journal of Nuclear Medicine*, vol. 23, no. 2, pp. 121–125, 1982.

[160] T. Herron and W. Gossman, *111 Indium White Blood Cell Scan (Indium Leukocyte Imaging, Indium-111 Scan)*. StatPearls Publishing, Treasure Island (FL), 2020.